

INSTITUTE OF EXPERIMENTAL PHYSICS
DEPARTMENT OF PHYSICS
WARSAW UNIVERSITY



Time-frequency analyses of EEG

by

Piotr Jerzy Durka

Advisor

Prof. dr hab. Katarzyna J. Blinowska

A DISSERTATION SUBMITTED IN PARTIAL FULFILLMENT
OF THE REQUIREMENTS FOR THE DEGREE OF
DOCTOR OF PHYSICS

AUGUST 1996

Acknowledgments

Through all the work that led to this dissertation I was fortunate to have the perfect boss and advisor in person of prof. Katarzyna J. Blinowska, whom I hereby express my gratefulness.

I am grateful to prof. Waldemar Szelenberger and dr Michał Skalski from Warsaw Medical School for experimental data and physiological consultations.

Thanks also to students at the University for difficult questions, cooperation and help.

Finally, I'm indebted to the idea of scientific information exchange over Internet; to those that edit electronic journals and update archive sites, and to those that make their latest results available to the scientific community in form of downloadable papers or software packages, like "mpp" by Stéphane Mallat and Zhifeng Zhang from New York University and "Aspirin/Migraines" by Russel Leighton from Mitre Corporation.

Abstract

Proper description of the electroencephalogram (EEG) often requires simultaneous localization of signal's structures in time and frequency. We discuss several time-frequency methods: windowed Fourier transform, wavelet transform (WT), wavelet packets, wavelet networks and Matching Pursuit (MP). Properties of orthogonal WT are discussed in detail. Advantages of wavelet parameterization, including fast calculation of band-limited products, are demonstrated on an example of input preprocessing for feedforward neural network learning detection of EEG artifacts.

MP algorithm finds sub-optimal solution to the problem of optimal linear expansion of function over large and redundant dictionary of waveforms. We construct a method for automatic detection and analysis of sleep spindles in overnight EEG recordings, based upon MP with real dictionary of Gabor functions. Each spindle is described in terms of natural parameters. In the same way the slow wave activity (SWA) is parametrized. In this framework several of reported in literature hypotheses, regarding spatial, temporal and frequency distribution of sleep spindles, and their relations to the SWA, are confirmed. We present also an application to automatic detection and spatial analysis of superimposed spindles. Finally, owing to its high sensitivity, proposed approach allows the first insight into the issue of low amplitude spindles, undetectable by the methods applied up to now.

Contents

Acknowledgments	i
Abstract	ii
Chapter 1.	
Introduction	1
1.1. Numerical analysis of EEG	1
1.2. Time-frequency phase space	3
1.3. Outline of Thesis	4
Chapter 2.	
Methods.	5
2.1. Windowed Fourier transform	5
2.2. Wavelet analysis	6
2.3. Artificial neural networks	10
2.4. Matching Pursuit	14
Chapter 3.	
Simulations and practical remarks	18
3.1. Windowed Fourier transform	20
3.2. Discrete orthogonal wavelet transform	23
3.2.1. Frequency resolution	23
3.2.2. Sensitivity of representation to a time shift of analyzed window	26
3.2.3. Border conditions	29
3.2.4. Calculation of band-limited products of two signals	29
3.3. Wavelet packets	31
3.4. Wavelet networks	32
3.5. Matching Pursuit with real discrete Gabor dictionary	35
3.5.1. Amplitude of a discrete Gabor function	36
3.5.2. Number of waveforms in the expansion	37
3.5.3. Heuristics in practical realizations	39

Chapter 4.

Results and discussion	47
4.1. Evoked potentials studies	48
4.1.1. Investigation of the influence of cerebellar lesions	48
4.2. Detection of EEG artifacts by artificial neural network	52
4.2.1. Tested networks	52
4.2.2. Discussion of results	54
4.2.3. Conclusions	55
4.3. Sleep spindles detection and analysis based upon	
Matching Pursuit parametrization	57
4.3.1. Experimental data	58
4.3.2. Choosing spindles from time-frequency atoms	58
4.3.2.1. Relevant parameters	59
4.3.2.2. Comparison of automatic detection to human	
judgment	61
4.3.3. Other methods of automatic detection of sleep spindles . .	64
4.3.4. Investigation of sleep spindles properties and	
distributions	66
4.3.4.1. Hypothesis of two generators	67
4.3.4.2. Superimposed spindles	68
4.3.4.3. Absence of spindles as hallmark of REM	
sleep	70
4.3.4.4. A step towards complete description of sleep	
EEG	70
4.3.4.5. Low amplitude spindles?	71
4.3.5. Remarks on definitions of EEG structures	73
4.3.6. Summary of MP application to spindles detection and	
analysis	85
5. Conclusions	86
5.1. Brief discussion of time-frequency methods	86
5.2. Summary	88
List of figures	90
Bibliography	93

Chapter 1.

Introduction

1.1. Numerical analysis of EEG

Electroencephalogram [EEG] is a recording of electrical activity of the brain. At the present state of knowledge there are two major facts concerning the analysis of EEG:

Fact 1: *Fundamentally we have no conception of how the brain functions as a psychoelectrochemical machine.*

Fact 2: *EEG is being used for decades as an important parameter in clinical practice. This "classical" knowledge of EEG is of phenomenological nature and relies mostly on visual analysis.*

Twenty three centuries ago Aristotle hypothesized that the brain serves to cool the blood. Today, after a century of experimental brain studies including 75 years from the first EEG recording, we know how does a single neuron work and we can register signals reflecting the global brain's activity with high accuracy. Nevertheless, we still lack the understanding of how the separate processes in the brain are organized into coherent functioning.

Our knowledge is mostly phenomenological. Visual analysis of raw recordings is the most widespread and trusted method of clinical EEG analysis, especially if transients or changes of signal's properties in time are of importance. In some cases,

when the information on the average properties of the analyzed epoch is preferred, spectral power estimates are used.

The art of visual analysis of EEG has three major limitations: sensitivity, repeatability and cost. Most of them could be overcome by numerical analyses, bringing meaningful improvement in both health care and basic neurophysiological research.

Constantly decreasing cost of computations together with rapid developments in mathematics are opening new possibilities in this field. A variety of signal processing techniques is being applied to the EEG time series. A proper choice of mathematical tool for a particular application constitutes a major difficulty. We need general criteria, which could be applied in such situations. They can be drawn from the general methodology of physical research (see e.g. Białkowski 1985) adopted to the particular situation in the analysis of EEG.

Criterion of verifiability

Generally this criterion is understood as consistence of results, given by the application of a new theory/method, with the prior knowledge. In EEG research the strongest reference for judgment of new results is usually the visual analysis. An assumption required for verification of this criterion is a possibility to check this consistence, which is not always straightforward.

Criterion of predictivity

A new method should obviously bring some improvement - traditionally related to widening of the research possibilities. A new tool may allow us to predict new phenomena or give new explanations. However, this criterion is not a *sin equa non* condition for a successful application of a new method in the field of EEG analysis. An automatic method fulfilling only the criterion of verifiability in some cases can bring a meaningful improvement by making possible reliable processing of larger amounts of data.

First breakthrough in the automatic analysis of EEG was brought by the introduction of the FFT (Fast Fourier Transform) algorithm in 1965, which made possible wide application of the Fourier transform (FT). The Fourier transform fulfilled the criterion of predictivity, providing a new brand of information - spectral distribution of signal's energy. However, FT is subject to high statistical errors and is severely biased as a consequence of the unfulfilled assumption that the signal is either infinite or periodic outside the measurement window. Nevertheless, until

today FFT is the major signal processing tool used for the analysis of biomedical signals. Parametric methods like autoregressive (AR) model are free from the "windowing" effect and give estimates of better statistical properties since no assumptions about the signal outside the measurement window are needed. However, similarly as in case of FT, the stationarity of signal is required.

The spectral methods like Fourier transform and AR models have their natural limits. They give overall characteristics of the whole analyzed segment and the signal structures of duration shorter than the measurement window cannot be identified. According to the present understanding, information processing by brain is coded by the dynamic changes of electrical activity in time, frequency and space. Full description of such phenomena requires high time-frequency resolution, which lies beyond the possibilities offered by FFT or AR. Nevertheless, these considerations are by no means intended to suggest that those methods are no more useful. Indeed there are cases where the overall characteristics of whole analyzed segment *are* required. Also in some cases the time-frequency analyses are still unable to provide the kind of information given e.g. by the multichannel AR model - the direction of information flow between electrodes (Kamiński and Blinowska 1991)

1.2. Time-frequency phase space

The term *phase space*, well known from physics, has its precise meaning also in signal processing applications (Daubechies 1990). In the area of time series analysis it is a two-dimensional space (plane) with time on horizontal and frequency on vertical axis, on which the density of signal's energy is being represented. Since in practice we deal with finite intervals of non-stationary signals, the representations of energy of such signals in this space is approximate and subject to statistical errors. The energy density is approximated on a discrete set of points of the time-frequency phase space. As time-frequency methods we understand tools providing information on both time and frequency localization of phenomena present in analyzed signal, or signal's energy density in the time-frequency phase space.

1.3. Outline of Thesis

In spite of arguments presented above, none of the time-frequency methods acquired position among the classical tools used in EEG analysis, like e.g. Fourier transform. Therefore in chapter 3 we briefly discuss practical issues related to application of several of the available time-frequency algorithms to the EEG analysis.

According to the presented discussion, orthogonal wavelet transform meets the requirements for analysis of time-locked phenomena and/or in cases where computational complexity is a major drawback. Examples of such applications are presented in chapters 4.1 and 4.2.

Since none of the presented approaches satisfied all the expectations, we introduce to biomedical signal processing a new method - Matching Pursuit. Chapter 4.3 proves that analysis based upon the MP decomposition fulfills the criteria formulated in paragraph 1.1, i.e. confirms results obtained previously by means of other methods and allows addressing questions that lie beyond the sensitivity of tools used up to now.

Moreover, methods proposed in chapters 4.2 and 4.3 constitute new and complete frameworks for EEG analysis. Both are being applied in large projects aimed at routine automatic detection of EEG artifacts and new and complete description of sleep EEG, respectively.

Chapter 2.

Methods.

2.1. Windowed Fourier transform

Windowed Fourier transform (or short-time Fourier transform) consists of multiplying the signal $f(t)$ with window function g , and computing the Fourier coefficients of the product gf . Window function g is centered around 0 and usually non-zero on a finite interval only. This procedure is repeated with translated versions of g : $g(t+t_0)$, $g(t+2t_0)$ etc. In such a way the signal's energy is represented on a discrete lattice of points in the time-frequency space:

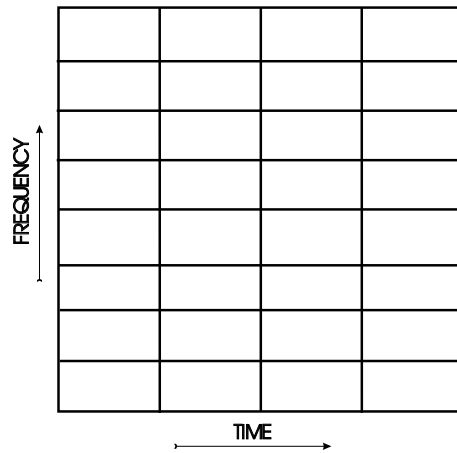


Figure 1 Symbolic division of time-frequency space for windowed Fourier transform

$$c_{mn}(f) = \int_{-\infty}^{\infty} e^{im\omega_0 t} g(t-nt_0) f(t) dt \quad (2.1)$$

$$m, n \in \mathbb{Z}$$

The coefficients $c_{m,n}$ give an indication of the energy content of signal f in the neighborhood of nt_0 in time and $m\omega_0$ in frequency. We can view them as products of the signal f with "coherent states" $g_{m,n}$, generated from a single window function g by translations and modulations, or translations in both time and frequency:

$$g_{m,n}(t) = e^{im\omega_0 t} g(t-nt_0) \quad (2.2)$$

However, it is proven (Daubechies 1990) that no reasonable [i.e. well concentrated in both time and frequency] choice of the window function g can lead to construction of a basis via the above formula. Therefore such representation will always bear an intrinsic redundancy.

2.2. Wavelet analysis

The function ψ is an admissible wavelet if it satisfies:

$$\int_{-\infty}^{\infty} \psi(t) dt = 0 \quad (2.3)$$

or, equivalently, if its Fourier transform $\hat{\psi}(\omega)$ satisfies $\hat{\psi}(0) = 0$. To fulfill this condition it has to oscillate, hence the name "wavelet". Wavelet transform describes signals in terms of coefficients, representing their energy content in specified time-frequency region. This representation is constructed by means of decomposition of the signal over a set of functions generated by translating and scaling one function - wavelet ψ :

$$\psi_{s,u}(t) = \frac{1}{\sqrt{s}} \psi\left(\frac{t-u}{s}\right) \quad (2.4)$$

The name (*ondelettes*) and general framework were introduced by Yves Meyer and Jean Morlet in 1984. Since then we observe explosion of successful applications of wavelet techniques, from differential equations and fractals to geophysics and image analysis and compression. Wavelet theory provided common framework for problems from different fields. Nevertheless, the introduction of wavelets cannot be treated as a completely new invention. Similar approach can be found in many works before 1984 - to quote only the Calderón-Zygmund¹ theory (Calderón and Zygmund 1954). However, the most important step, at least from the point of view of practical

¹Antoni Zygmund - polish mathematician, graduated from Warsaw University, from 1930 professor of Stefan Batory University in Wilno. Since 1940 in USA. (Kuratowski 1973)

applications to the time series analysis, was finding in early eighties that formula (2.4) can generate an orthonormal basis of $L^2(\mathbb{R})$, with ψ being function well localized in both time and frequency domains. We will discuss such bases in the framework of multiresolution decomposition.

Multiresolution decomposition can be viewed as a recursive approximation of a signal at resolutions changing usually as powers of two. The logarithmic scale of resolution is very convenient from mathematical point of view, as will be presented below. It corresponds also to human perception of intensity (Lindsay and Norman 1972). The goal of multiresolution wavelet representation is to quantify the increase of information about the signal, acquired with increasing resolution.

If we denote the approximation of function f at scale 2^j as $A_{2^j}f$, then obviously between scale 2^{j+1} and coarser scale 2^j some information is lost. It can be retrieved in a "detail signal" $D_{2^j}f$. Both operations [approximation and extracting the difference] are orthogonal projections on subspaces of $L^2(\mathbb{R})$, respectively V_{2^j} and O_{2^j} , such that $O_{2^j} \oplus V_{2^j} = V_{2^{j+1}}$. Orthogonal bases of both spaces are generated by dilating and translating scaling function Φ [for approximations] and wavelet ψ [for the detail signals]. If we denote $\psi_{2^j}(x) = 2^j \psi(2^j x)$, then $(\sqrt{2^{-j}} \phi_{2^j}(t - 2^{-j}n))_{n \in \mathbb{Z}}$ and $(\sqrt{2^{-j}} \psi_{2^j}(t - 2^{-j}n))_{n \in \mathbb{Z}}$ form orthonormal bases of V_{2^j} and O_{2^j} , respectively. Finally a set of wavelets

$$(\sqrt{2^{-j}} \psi_{2^j}(t - 2^{-j}n))_{(n,j) \in \mathbb{Z}^2} \quad (2.5)$$

is an orthonormal basis of $L^2(\mathbb{R})$. The function f is fully characterized by [and can be reconstructed from] its wavelet coefficients:

$$D_{2^j}^n(f) = \langle f(t), \psi_{2^j}(t - 2^{-j}n) \rangle \quad (2.6)$$

$$f(t) = \sum_{j,n} D_{2^j}^n(f) \psi_{2^j}(t - 2^{-j}n) \quad (2.7)$$

The scale 2^j corresponds to an octave of signal bandwidth. If we denote Nyquist frequency as f_N , then scale 2^0 [octave 0] covers frequencies from $f_N/2$ to f_N , scale 2^1 - from $f_N/4$ to $f_N/2$ and so on.

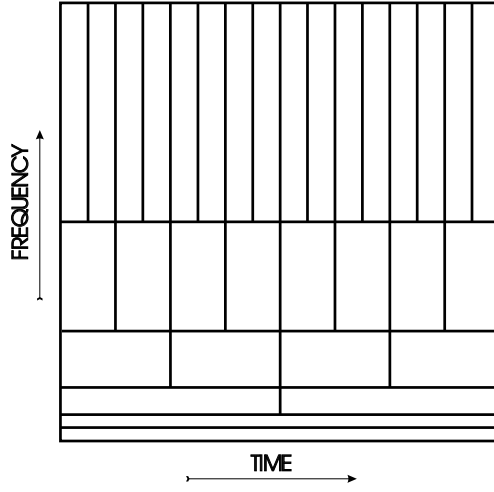


Figure 2 Symbolic division of time-frequency space for multiresolution wavelet decomposition.

Figure 2 represents symbolic division of the time-frequency plane into "Heisenberg boxes", corresponding to ranges of time and frequency parameters, in which the signal's energy is explained by one wavelet coefficient. In reality the borders between these boxes are diluted due to the overlap of time and frequency support of wavelet functions.

Wavelets used in numerical experiments in the next chapter were built from cubic splines, as proposed in (Mallat 1989). The shape of a scaling function and corresponding wavelet are presented in Figure 3

together with a scheme of the multiresolution decomposition.

The multiresolution decomposition [lower part of Figure 3] yields a very efficient pyramidal algorithm for calculating the $D_{2^j}^n$ coefficients, based on quadrature mirror filters. The approximation of a signal at scale 2^j contains all the information necessary to compute coarser approximation at scale 2^{j+1} , as well as the difference of these approximations. Decomposition is performed by an application of low-pass [for $A_{2^j}(f)$] and band-pass [for $D_{2^j}(f)$] filters followed by downsampling [keeping every second sample]. The original signal can be retrieved by the inverse procedure. We can also reconstruct the signal from a subset of it's wavelet coefficients, which corresponds to reproducing signal's energy from particular time-frequency regions. Usually reconstruction from a small subset of largest coefficients reproduces main structures of the signal. By keeping only those coefficients we can achieve a high compression ratio.

In (Mallat 1992) we find an interesting example of denoising algorithm based upon multiresolution wavelet decomposition. To describe it briefly we must first define a Lipschitz exponent. We say that a function $f(t)$ is uniformly Lipschitz α ($0 \leq \alpha \leq 1$) over an interval $[a, b]$ if and only if there exists a constant K such that for any $(t_0, t_1) \in [a, b]^2$

$$|f(t_0) - f(t_1)| \leq K |t_0 - t_1|^\alpha \quad (2.8)$$

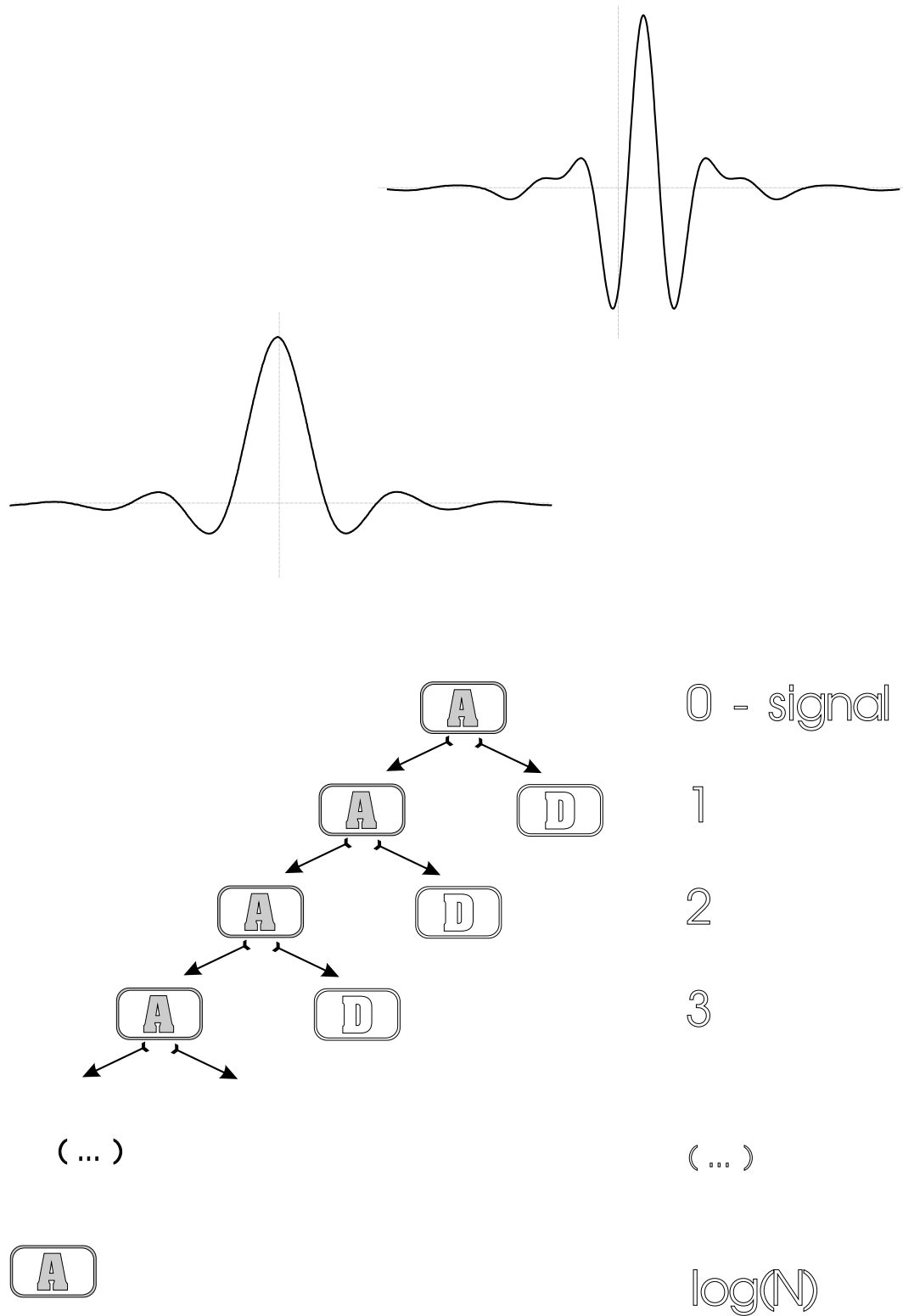


Figure 3 Top: left - scaling function, right - wavelet. Lower part - scheme of multiresolution decomposition. A - approximated, D - detail signals at each level.

If $f(t)$ is differentiable at t_0 , then it is Lipschitz $\alpha=1$. For larger α the function $f(t)$ will be more "regular" at t_0 . If $f(t)$ is discontinuous but bounded in the neighborhood of t_0 , then $\alpha=0$. The Lipschitz exponent α of a function can be measured from the evolution across scales of the absolute value of the wavelet transform, as demonstrated in (Mallat 1992). According to the values of Lipschitz exponent the wavelet transform maxima corresponding to the white noise [or other disturbances definable in terms of Lipschitz exponents] can be removed and the signal can be reconstructed from the remaining maxima of its wavelet transform.

2.3. Artificial neural networks

McCulloch and Pitts (1943) proposed a simple model of neuron as a unit computing weighted input from neighboring neurons. The binary output depends on whether the input exceeded a threshold value. This output can in turn serve as one of the input values for other neurons. Influence of i -th neuron's output on the j -th neuron's input is modified by multiplicative coefficients w_{ij} called the connection weights. For $w_{ij} > 0$ we call the connection excitatory, for $w_{ij} < 0$ - inhibitory. Later instead of binary threshold function a smoother sigmoidal function was proposed. The following equation reflects the above assumptions:

$$n_i(t+1) = f_\sigma(\sum_j w_{ij}n_j(t) - \mu_i) \quad (2.9)$$

$n_i(t)$ - activity of i -th neuron in time t ,

w_{ij} - weight of the connection from the i -th to the j -th neuron,

μ_i - threshold value for the i -th neuron,

$f_\sigma(x) = 1/(1+e^{-x})$, the sigmoid function that usually replaces initially proposed step function $\Theta(x)$.

Such "neurons" were initially intended for modeling of the brain's functioning. However, the resemblance to the live brain's neurons is only superficial - the model is far too simplified. On the other hand such a simplified approach offers many significant advantages in approximation and classification tasks. Therefore artificial neural networks (ANN) evaluated into a purely mathematical tool. The type most widely used in practice are multi-layer feedforward ANN. They can be used in brain research just like in any other task requiring e.g. generalization of knowledge from

a set of input/output data, for which the mechanism of underlying relations is not known.

Based upon equation (2.9) we can construct a network consisting of three layers only to approximate any continuous function with desired accuracy (Cybenko 1989). However, it takes a four-layer feedforward network to realize exactly all possible partitionings of the input space (Kolmogorov 1957).

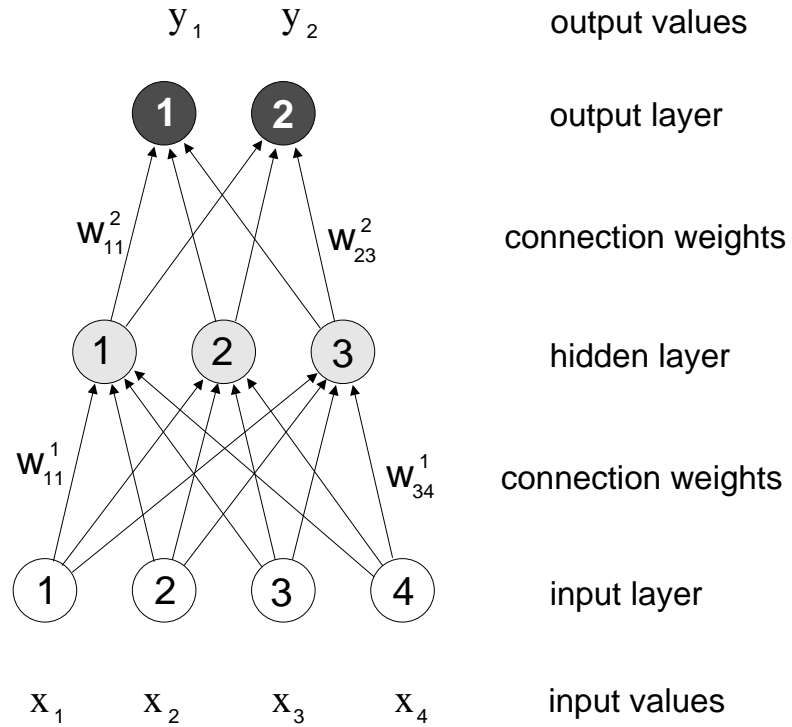


Figure 4 Schematic representation of a three-layer ANN

Figure 4 presents an example of a three-layer feedforward ANN. The first layer [sometimes omitted in numeration] is the input layer, receiving input values x_i . Vector $\{x_i\}$ represents the input data after possibly applied preprocessing. Units in the input layer do not perform any operations on the input data, simply passing values multiplied by the connection weights w_{ij}^1 to the hidden layer. Units in this layer generate output by eg. (2.9) applied to the weighted sum of inputs. Generally more than one hidden layer can be present. Finally the weighted sum of outputs from last hidden layer reaches the output layer. Units in the output layer produce the output values y_i , by applying eg. (2.9) again.

The knowledge used for training the network should consist of set of pairs of vectors: "question" vector $\{x^m\}$ and known "answer" vector $\{d^m\}$. Such vectors paired in

set $\{x^m ; d^m\}$, ($m=1 \dots M$) constitute the "lesson". "Learning" such a "lesson" consists of adjusting the connection weights w_{ij}^k to minimize the least mean square error between the desired outputs d^m and network's responses y^m :

$$E = \frac{1}{2} \sum_{m=1}^M (d^m - y^m)^2 \quad (2.10)$$

Usually the first order gradient descent with a momentum term is used:

$$w_{ij}^m(t+1) = w_{ij}^m(t) - \eta \frac{\delta E}{\delta w_{ij}^m(t)} - \alpha (w_{ij}^m(t) - w_{ij}^m(t-1)) \quad (2.11)$$

where η is called learning rate and $0 < \alpha < 1$.

A classical way of applying such a network for particular problem may consist of the following phases:

1. Choice of network's topology.

Issues encountered at this point include number of layers, scheme of their interconnections and sizes of the input and output layers. Sizes of input and output layers depend strongly on the particular features of the problem being investigated. Size of the output layer should be equal to at least number of bits representing the features recognized by the network. Number of input neurons depends naturally on the size of input data vector after preprocessing.

2. Choice of input preprocessing.

From the theoretical point of view an artificial neural network with only one hidden layer can approximate any continuous function, i.e. any mapping. It means that in principle such a network can also develop any function that we would like to include in preprocessing (Cybenko 1989). In practice relying on such an assumption requires use of larger networks trained on larger datasets. In such case the generalization abilities of the network, measured usually as the performance on data other than the training set, are severely impaired. It was shown in (Hertz et al 1993) that the probability of

proper generalization goes down with the ratio of information relevant to the classification to the information non-relevant to the classification in the network's input. That indicates the importance of careful choice of input data and preprocessing.

3. Learning phase.

A training set is composed of pairs of input-output data. The output data may consist of classification obtained by other means (e.g. human expert), that we want to emulate by means of the network. For each presented data vector the network's response is being computed. Based upon the difference between network's response and the "response" bound with the presented input in the training set, the network's connection weights are modified according to a learning rule (e.g the error backpropagation algorithm). The procedure is repeated until a satisfactory network's performance on the training set is achieved.

4. Testing

The most interesting feature of ANNs is their ability of generalization beyond the learning set. Achieving satisfactory generalization often requires fine tuning of the whole system, including the input preprocessing, as will be presented below. Generalization abilities can be checked via network's performance on a dataset other than the learning set.

2.4. Matching Pursuit

Natural limitations of classical wavelet transform in biomedical signal processing are due to relatively small set of waveforms used to express the signal's variance. We can say that the dictionary used in WT is limited. In case of orthogonal wavelet transform or wavelet packets we deal with the smallest possible dictionary - an orthonormal basis.

On the contrary, the natural languages are highly redundant: there are many words with close meanings. Due to this fact we are able to express very subtle and complicated ideas in relatively few words - like in poetry. On the other hand, let's suppose that the same ideas (feelings, thoughts) are being described by a person using a limited dictionary. Not only shall the expression grow in size, but it will lose much of its meaning and, of course, elegance.

Dictionaries of low [or none, as in case of a basis] redundancy are convenient for both calculations and interpretation. However, if the adaptivity of representation is the main goal, we should extend the repertoire of basic functions. A large and redundant dictionary of basic waveforms can be generated e.g. by scaling, translating and, unlike WT, **modulating** a single window function $g(t)$:

$$g_I(t) = \frac{1}{\sqrt{s}} g\left(\frac{t-u}{s}\right) e^{i\xi t} \quad (2.12)$$

$s > 0$ - scale,

ξ - frequency modulation,

u - translation.

Index $I = (\xi, s, u)$ describes the set of parameters. The window function $g(t)$ is usually even and its energy is mostly concentrated around u in a time domain proportional to s . In frequency domain the energy is mostly concentrated around ξ with a spread proportional to $1/s$. The minimum of time-frequency variance is obtained when $g(t)$ is Gaussian. The dictionaries of windowed Fourier transform and wavelet transform can be derived as subsets of this dictionary, defined by certain restrictions on the choice of parameters. In case of the windowed Fourier transform the scale s is constant - equal to the window length - and the parameters ξ and u are uniformly sampled. In the case of WT the frequency modulation is limited by the restriction on the frequency parameter $\xi = \xi_0/s$, $\xi_0 = \text{const.}$

It remains to choose from such dictionary waveforms fitting at best the signal structures, i.e. optimally explaining signal's variance. We can define an optimal ε -approximation as an expansion minimalizing the error ε of the approximation of signal f by M waveforms:

$$\varepsilon = \| f - \sum_{i=1}^M \langle f, g_{I_i} \rangle g_{I_i} \| = \min. \quad (2.13)$$

Finding such an optimal ε -approximation is a NP-hard² problem (Davis 1994). This can be proved by showing that the "Exact Cover by 3-Sets Problem" (Garey and Johnson 1979) can be transformed in polynomial time into an optimal ε -approximation problem. Thus, an algorithm which solves the ε -approximation problem can solve the "Exact Cover by 3-Sets Problem", which is known to be NP-complete.

We can say that the optimal representation - or all the information necessary to compute it - is encrypted in the sequence of numbers constituting the time series, but we don't have neither a key [Fact 1 section 1.1] nor an efficient way to break the cipher.

Another problem emerges from the fact that such an optimal expansion would be unstable with respect to the number of used waveforms M , because changing M even by one can completely change the set of waveforms chosen for the representation. These problems turn our attention to sub-optimal solutions. A sub-optimal expansion of a function over such a redundant dictionary can be found by means of the **Matching Pursuit algorithm**:

In the first step of the iterative procedure we choose the vector g_{I_0} which gives the largest product with the signal $f(t)$:

$$f = \langle f, g_{I_0} \rangle g_{I_0} + R^1 f \quad (2.14)$$

Then the residual vector R^1 obtained after approximating f in the direction g_{I_0} is decomposed in a similar way. The iterative procedure is repeated on the following obtained residues:

² NP stands for nondeterministic-polynomial, describing a class of problems for which the general solution in polynomial time is not known. Or, in other words, computational complexity grows with the size of problem faster than any polynomial (Harel 1987).

$$R^n f = \langle R^n f, g_{I_n} \rangle g_{I_n} + R^{n+1} f \quad (2.15)$$

In this way the signal f is decomposed into a sum of time-frequency atoms, chosen to match optimally the signal's residues:

$$f = \sum_{n=0}^m \langle R^n f, g_{I_n} \rangle g_{I_n} + R^{m+1} f \quad (2.16)$$

It was proven (Davis et al 1994) that the procedure converges to $f(t)$, i.e.

$$\lim_{m \rightarrow \infty} \|R^m f\| = 0 \quad (2.17)$$

Hence

$$f(t) = \sum_{n=0}^{\infty} \langle R^n f, g_{I_n} \rangle g_{I_n} \quad (2.18)$$

and

$$\|f\|^2 = \sum_{n=0}^{\infty} |\langle R^n f, g_{I_n} \rangle|^2 \quad (2.19)$$

We can visualize the results of MP decomposition in time-frequency plane by adding the Wigner distributions of each of the selected atoms. The Wigner distribution of $f(t)$ is defined as

$$Wf(t, \omega) = \frac{1}{2\pi} \int_{-\infty}^{\infty} f(t + \tau) \bar{f}(t - \tau) e^{-i\omega\tau} d\tau \quad (2.20)$$

Calculating the Wigner distribution from the whole decomposition as defined by eq. (2.18) would yield

$$Wf(t, \omega) = \sum_{n=0}^{+\infty} |\langle R^n f, g_{I_n} \rangle|^2 Wg_{I_n}(t, \omega) + \sum_{n=0}^{+\infty} \sum_{m=0, m \neq n}^{+\infty} \langle R^n f, g_{I_n} \rangle \overline{\langle R^m f, g_{I_m} \rangle} W[g_{I_n}, g_{I_m}](t, \omega) \quad (2.21)$$

where the cross Wigner distribution $W[f, h](t, \omega)$ of functions f and h is defined as

$$W[f, h](t, \omega) = \frac{1}{2\pi} \int_{-\infty}^{\infty} f(t + \tau) \bar{h}(t - \tau) e^{-i\omega\tau} d\tau \quad (2.22)$$

The double sum in eq. (2.21), containing cross Wigner distributions of different atoms from the expansion (2.18), corresponds to the cross terms generally present in Wigner distribution. These terms one usually tries to remove in order to obtain a clear picture of the energy distribution in the time-frequency plane. Removing these terms from eq. (2.21) is straightforward - we keep only the first sum. Therefore, for visualization of the energy density in time-frequency plane of signal's representation obtained by means of MP, we can define a magnitude $Ef(t, \omega)$:

$$Ef(t, \omega) = \sum_{n=0}^{+\infty} | \langle R^n f, g_{I_n} \rangle |^2 W_{g_{I_n}}(t, \omega) \quad (2.23)$$

Wigner distribution of a single atom g_I conserves its energy over the time-frequency plane

$$\int_{-\infty}^{\infty} \int_{-\infty}^{\infty} W_{g_I}(t, \omega) dt d\omega = \|g_I\|^2 = 1 \quad (2.24)$$

Combining this with energy conservation of the MP expansion [eq. (2.19)] and eq. (2.22) yields

$$\int_{-\infty}^{\infty} \int_{-\infty}^{\infty} Ef(t, \omega) dt d\omega = \|f\|^2 \quad (2.25)$$

This justifies the interpretation of $Ef(t, \omega)$ as the energy density of signal $f(t)$ in the time-frequency plane. All the presentations in this work referred to as "Wigner maps" are based upon formula (2.23) - except for the fact that the sum is not infinite. The issue of the point at which we should stop the iterations will be further discussed in chapter 3.5.2.

Chapter 3.

Simulations and practical remarks

Figure 5 presents the components of signals simulated for the purpose of presentations of time-frequency methods in this work. The basic signal, labeled *IV*, is a sum of signals *I*, *II* and *III*, which were drawn to present clearly the contributing structures. Structure *A* is a sine modulated by 4th power of Gauss, *B* is built from straight lines. Structures *C* and *D* are Gabor functions, i.e. sines modulated by Gauss. They have different modulation frequencies and time widths and are centered in the same point in time. Structure *E* is a realization of Dirac's delta [one-point discontinuity], *F* - sine wave running through all the epoch. A noise of similar amplitude and 2.5 times higher variance [signal *V*] was added to signal *IV* to produce the noisy signal *VI*.

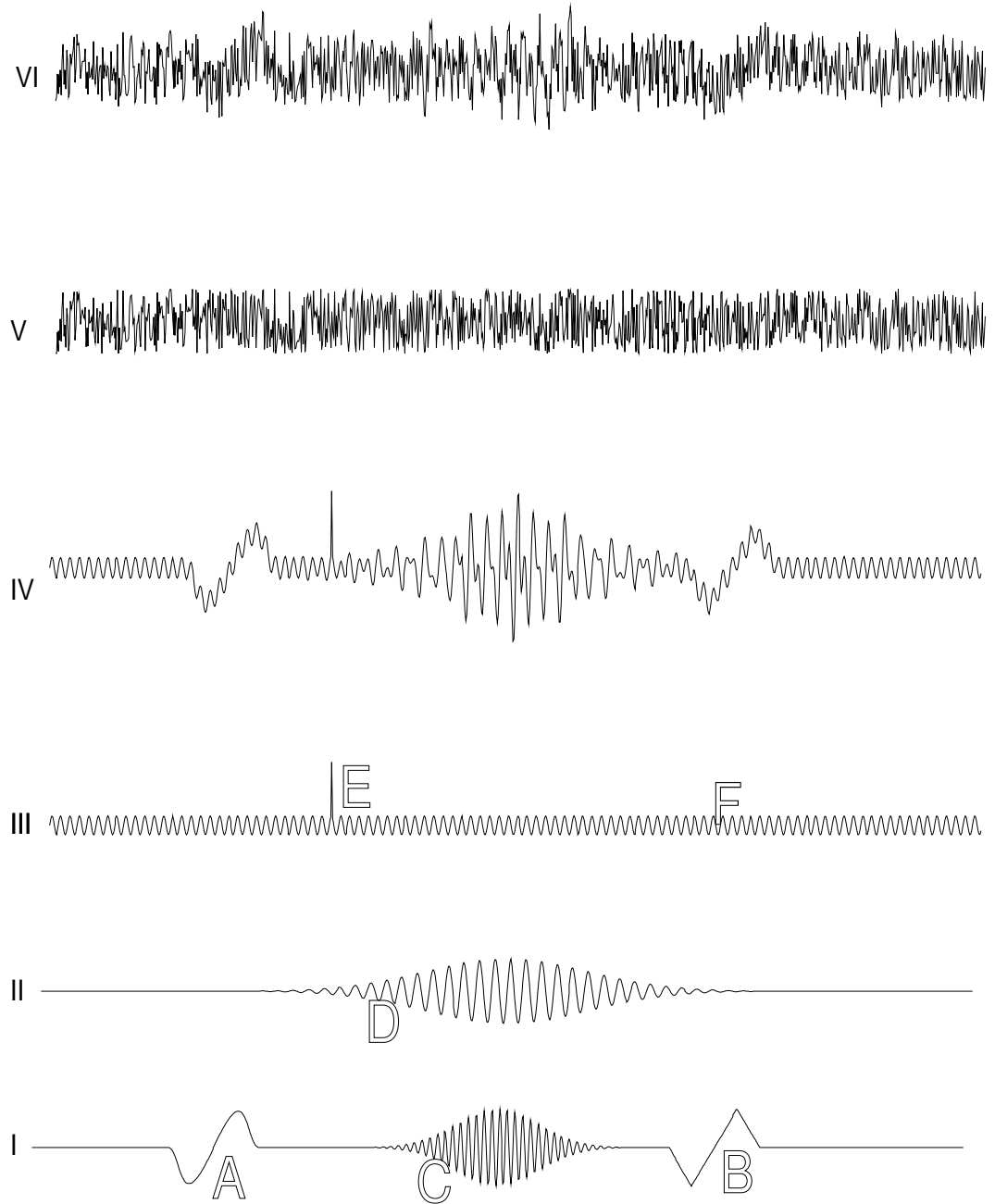


Figure 5 Simulated signals (IV and VI) used for presentation of performance of discussed time-frequency methods. I-III and V present structures contributing to signals IV and VI.

3.1. Windowed Fourier transform

Figure 6 presents Fourier spectral analysis of signal *IV* [plotted in the bottom]. In the upper part the Fourier estimate of spectral density is plotted versus frequency [abscissa]. We notice a sharp peak corresponding to the sine *F* and wider peaks in frequencies of spindles *C* and *D*. Energy of structures *A* and *B* is concentrated in the low frequency region. The one-point discontinuity *E* is reflected in high-frequency regions, however its representation is impossible to interpret visually and without the information about the phase of the Fourier transform.

Middle part of Figure 6 presents a spectrogram, i.e. representation of a realization of windowed Fourier transform. The time resolution is limited to the time width of windowing function. Therefore we can hardly treat the representation of signal's structures in this time-frequency plane as their time-frequency signatures. The best frequency resolution is obtained for the structure *F*, represented as a constant frequency running through all the analyzed epoch. Nevertheless the accuracy of identification of this frequency, comparing to the Fourier transform of the whole segment, is limited by the fact that the spectral estimate is calculated from shorter epochs. Energy of the Dirac's delta *E* is diluted in two subsequent time sections, because the time windows *g* [eq. (2.2)] overlap.

Figure 7 presents the same plots as the previous figure for the noisy signal *VI*. From the spectral density plot in the upper part we can still extract the peaks corresponding to the sine *F* and lower-frequency spindle *D*. Peak corresponding to the higher-frequency spindle *C* is slightly distorted, comparing to the previous figure. Other structures are buried in noise. None of these structures can be reliably identified on the spectrogram plotted in the middle part.

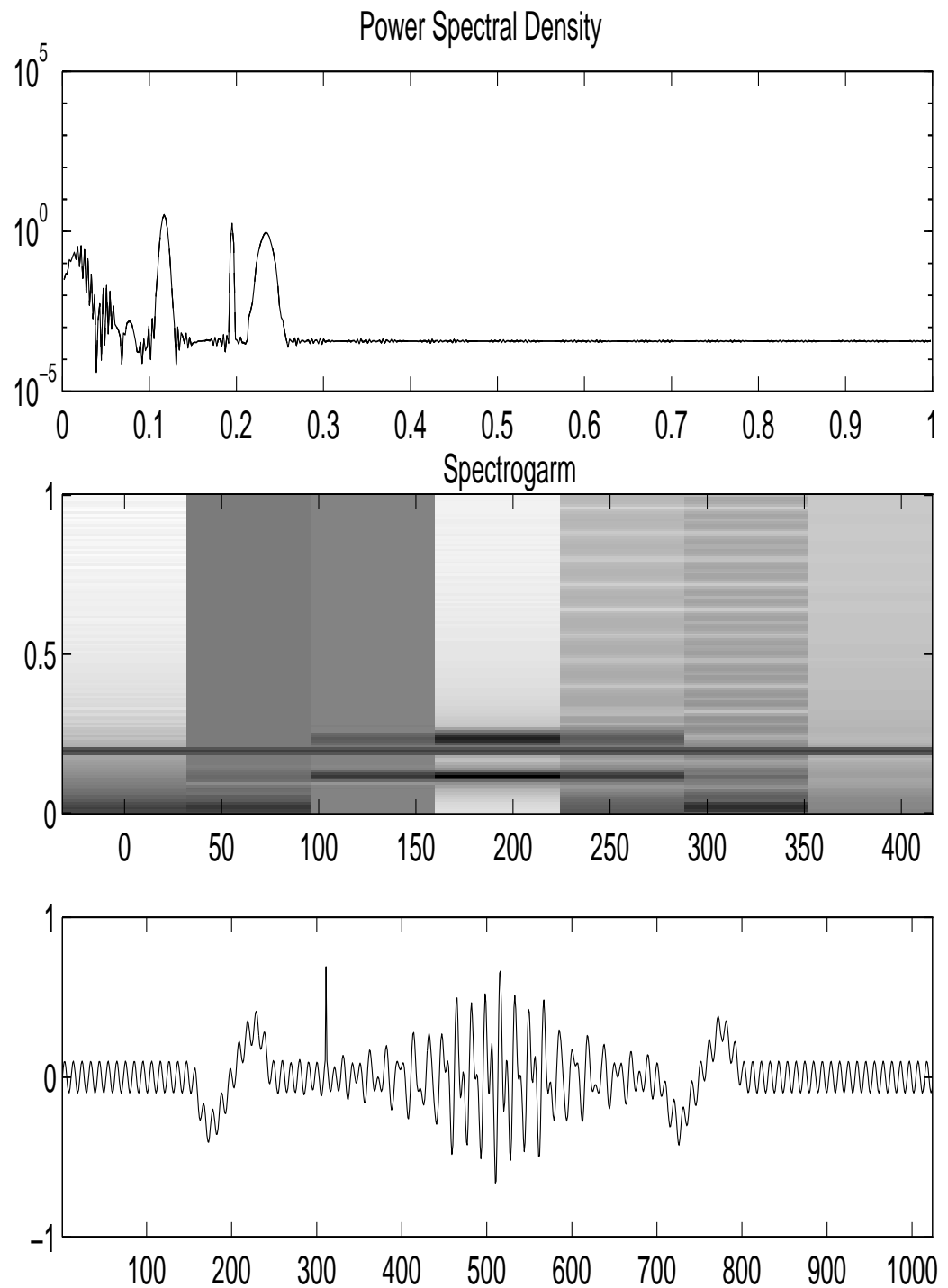


Figure 6 Bottom - signal IV from Figure 5. Top - Fourier estimate of its spectral power density. Middle part - spectrogram, i.e. realization of windowed Fourier Transform.

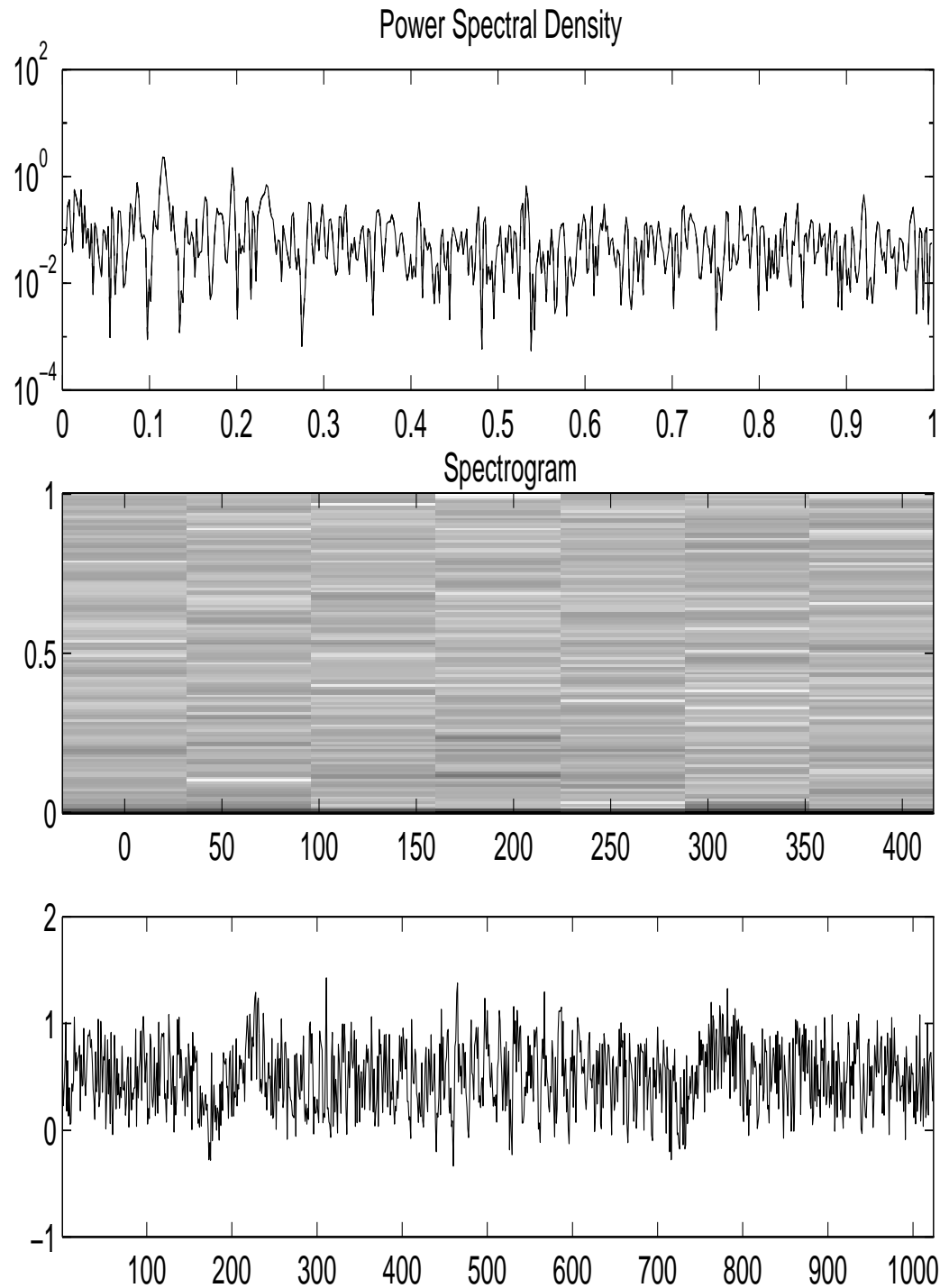


Figure 7 Bottom - noisy signal VI from Figure 5. Top - Fourier estimate of its spectral power density. Middle part - spectrogram, i.e. realization of windowed Fourier transform.

3.2. Discrete orthogonal wavelet transform

3.2.1. Frequency resolution

Figure 8 *a*) presents results of multiresolution decomposition of the simulated signal *IV* from Figure 5, plotted at the bottom. Curves labeled 1-9 are signal's reconstructions from all the wavelet coefficients at given scale. Reconstruction of signal from all the wavelet coefficients at given scale corresponds to band-pass filtering - see also section 3.2.4. We observe that energy of spindles C and D is diluted across scales from 2 to 4.

Figure 8 *b*) presents decomposition of the described above noisy signal *VI*. Again the decomposed signal is drawn at the bottom. Above the reconstructions of signal at scales of wavelet decomposition are shown, with corresponding frequencies decreasing upwards. Comparing these two figures we notice that energy of the noise is concentrated mainly at scales corresponding to higher frequencies [lower on the picture]. In these scales the signal's features, clearly represented on Figure 8 *a*), are buried in noise. Lower frequency structures are relatively less affected by the addition of noise.

Figure 9 shows an alternative way of presenting results of a multiresolution wavelet decomposition [for the same signals as decomposed in Figure 8]. At each scale the values of discrete wavelet coefficients are presented instead of the signal's reconstructions. Heights of rectangles on each level indicate the values of corresponding wavelet coefficients [eq. (2.6)]. Octaves are labeled by numbers [1-9] on the right and corresponding frequencies decrease upwards.

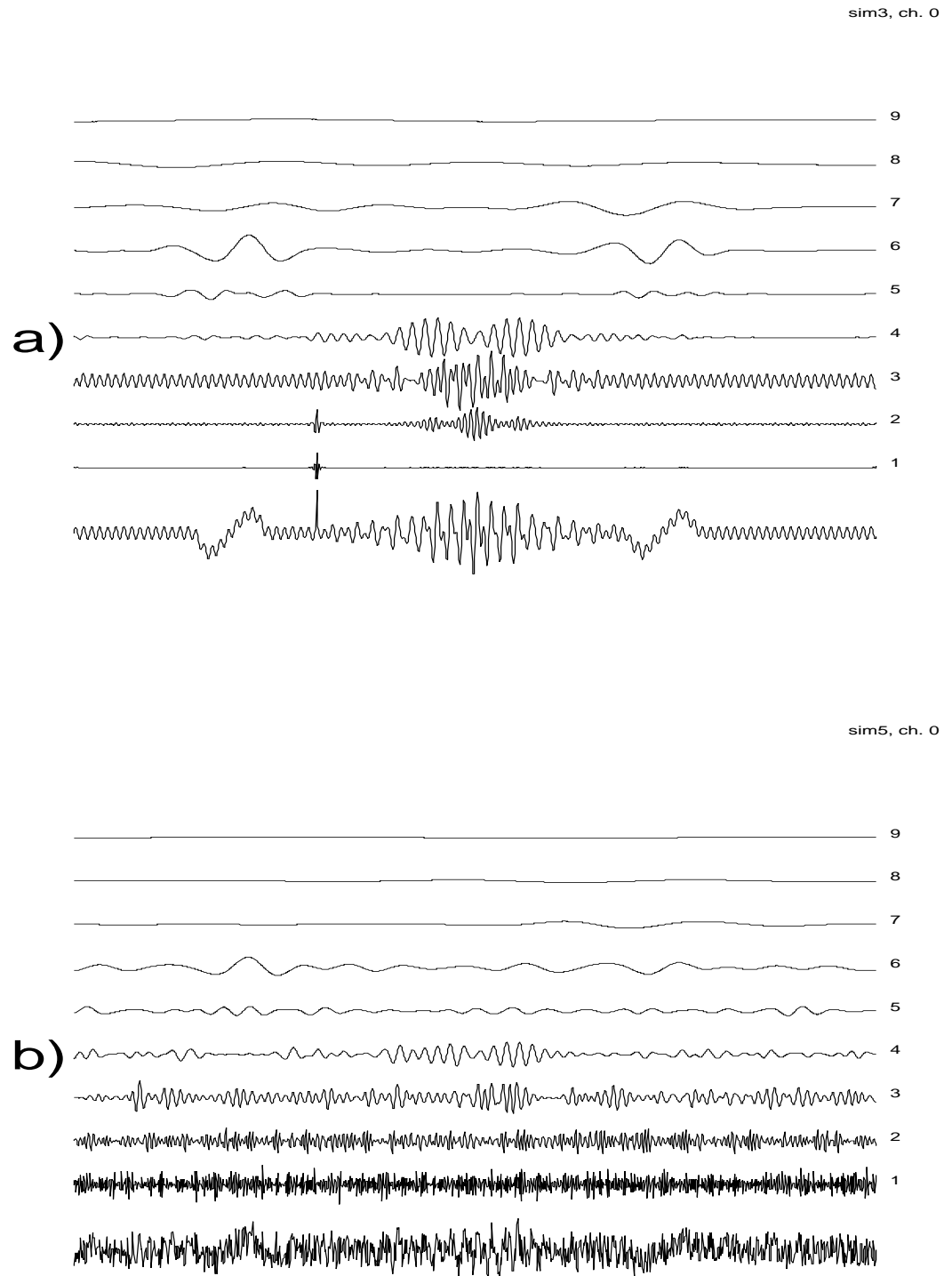


Figure 8 Multiresolution decomposition of simulated signals: a) IV, b) VI from Figure 5. Reconstructions from wavelet coefficients at the corresponding octaves [j , marked 1-9 on the right].

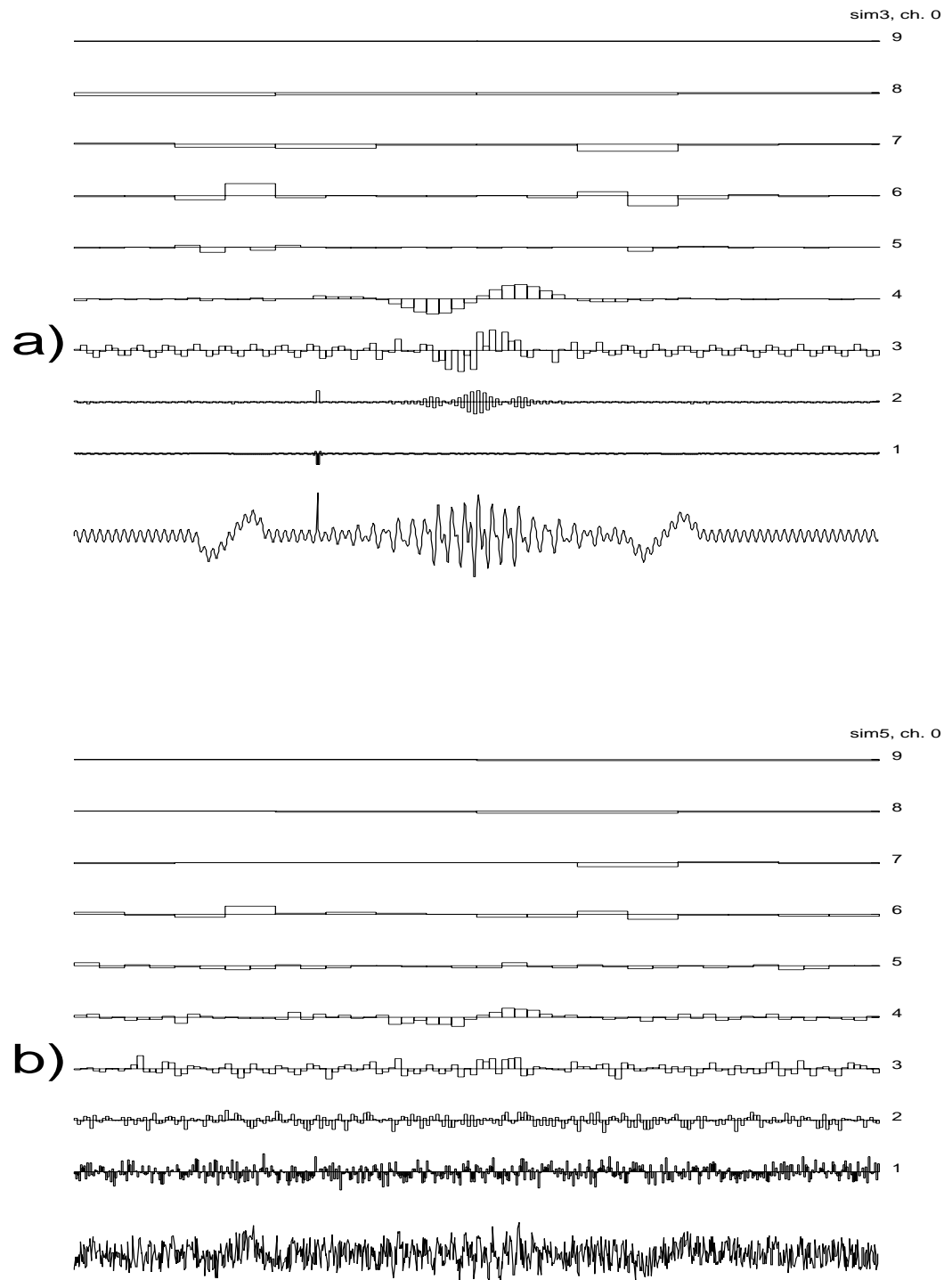


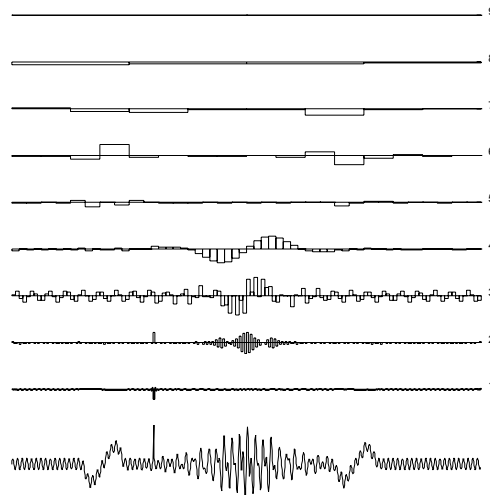
Figure 9 Multiresolution decomposition of simulated signals: a) IV, b) VI from Figure 5. Height of rectangles at each scale corresponds to the values of discrete wavelet coefficients.

3.2.2. Sensitivity of representation to a time shift of analyzed window

When using wavelet parameterization, we must be aware of sensitivity of the representation to the shift in time of the analyzed window. That means, that if we move the beginning of the analyzed segment by few points in time, we get a different set of wavelet coefficients describing the same structures. Or, in other words, the energy of a signal's structure can be distributed between neighboring wavelet coefficients in a different way, depending on the relative position of analyzed section of the signal. This effect is presented in Figure 10 and Figure 11, where the signal *IV* from Figure 5 was subjected to multiresolution decomposition after moving the analyzed window by 0, 5, 10 and 15 points in time. Figure 10 reveals that values of wavelet coefficients describing the same structures differ depending of the shift. We can observe this effect clearly on the two Gabor functions [structures C and D from Figure 5] in the center of the signal, in levels 2 to 5. The pattern of wavelet coefficients representing these structures varies with subsequent shifts, to reach almost its primary form after shift by 15 points. For a 1024 points signal, as is the case for signals from Figure 5, on the fourth level we have 64 coefficients and each of them corresponds to 16 points of analyzed signal. Therefore 16 points is the first shift that conserves the representation on scale 4 and below. Since 15 is only close to that value, the representation is not completely invariant, which is visible mainly at scales 2 and 3. The time shift affects very little the Dirac's delta, because it's energy is represented in the high frequency region, where the time resolution is very good.

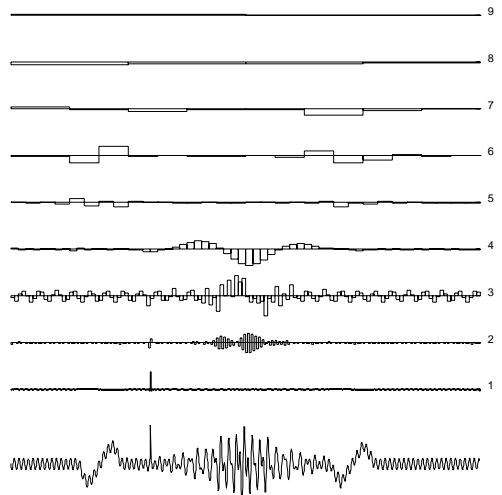
In Figure 11 we observe the same effect on signals reconstructed at different resolutions. These curves are signal's reconstructions from all the coefficients from given scale. Such an operation corresponds to band-pass filtering of the signal [see also section 3.2.4]. Nevertheless, we notice that results of this kind of filtering depend on the shift in time of analyzed window.

P.J. Durka IFD UW: FALKI

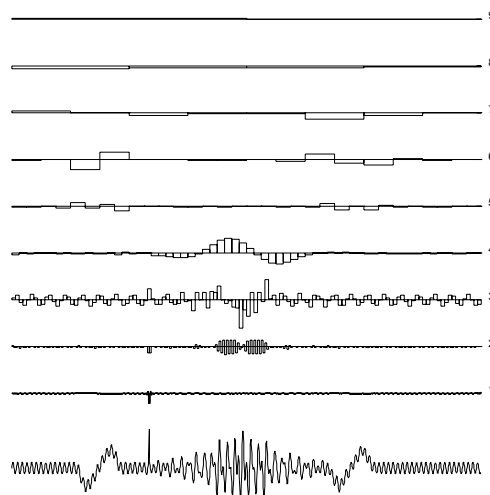


a)

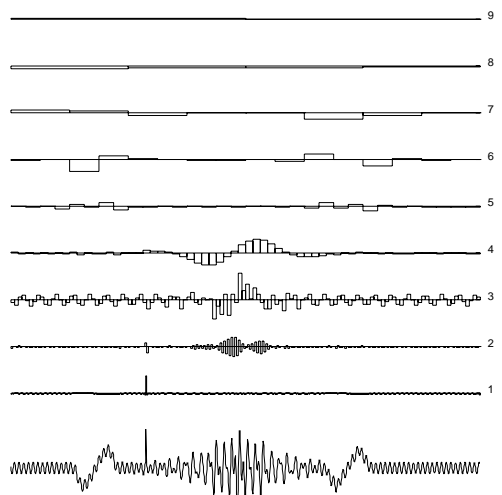
P.J. Durka IFD UW: FALKI



b) shift 5 points



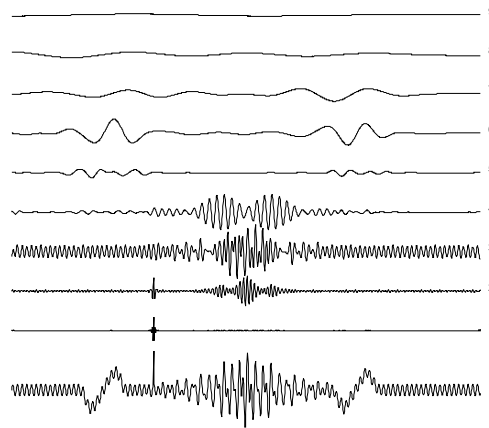
c) shift 10 points



d) shift 15 points

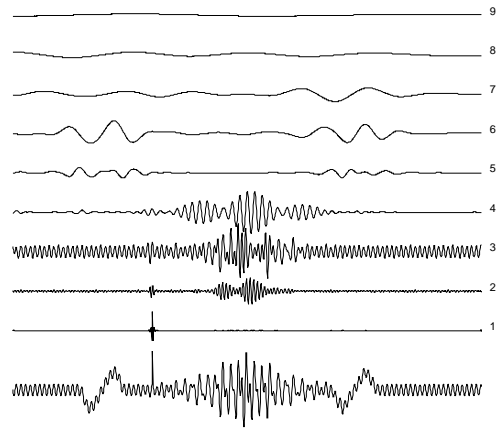
Figure 10 Multiresolution decomposition of the simulated signal shifted by 0, 5, 10 and 15 points in time. Representation of discrete wavelet coefficients.

P.J. Durka IFD UW: FALKI

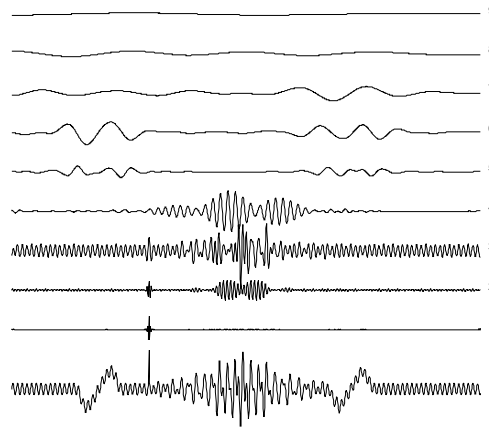


a)

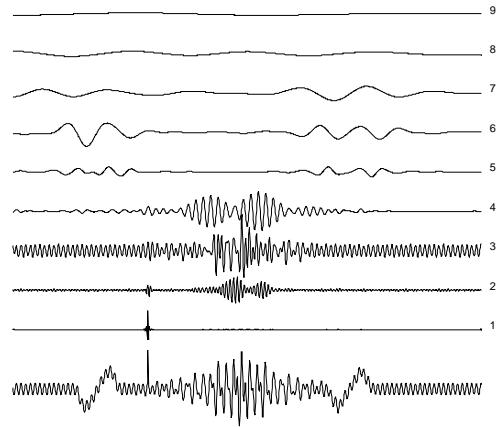
P.J. Durka IFD UW: FALKI



b) shift 5 points



c) shift 10 points



d) shift 15 points

Figure 11 Multiresolution decomposition of the simulated signal, shifted by 0, 5, 10 and 15 points in time. Curves marked 1-9 are reconstructions from wavelet coefficients at the corresponding scale 2^j .

3.2.3. Border conditions

Support in time of wavelet functions, especially for lower frequencies, exceeds the borders of analyzed signal. Therefore for the numerical analysis we must make some assumption about the behavior of signal outside the measurement window. In practice the most common approach is to assume the symmetry (or antisymmetry) with respect to the first and the last point, which gives the best results in most of the cases. However, for some classes of signals, better results are obtained by setting the signal to zero outside the measurement window. An example of such case is provided by the otoacoustic emissions (OAE), gently approaching zero at both their ends [Figure 12].

3.2.4. Calculation of band-limited products of two signals

Wavelet coefficients can serve as a basis for efficient computation of certain spectral and cross-spectral coefficients. Recalling eq. (2.7) from section 2.2, we notice that reconstructing signal from wavelet coefficients from one level only [scale 2^j] is equivalent to band-pass filtering [see e.g. Figure 8]. Normalized product of two signals f and g reconstructed in such a way will give us their cross-correlation in frequency band corresponding to scale 2^j . If we denote by f_j and g_j reconstructions of functions f and g , respectively, from their wavelet coefficients at scale 2^j , then

$$\begin{aligned} \langle f_j(t), g_j(t) \rangle &= \sum_t \{ \sum_n [D_{2^j}^n(f) \psi_{2^j}(t-2^{-j}n)] * \sum_m [D_{2^j}^n(g) \psi_{2^j}(t-2^{-j}m)] \} \\ &= \sum_n \sum_m \{ D_{2^j}^n(f) D_{2^j}^m(g) \sum_t (\psi_{2^j}(t-2^{-j}n) \psi_{2^j}(t-2^{-j}m)) \} \end{aligned} \quad (3.1)$$

In case of orthogonal wavelet transform

$$\sum_t [\psi_{2^j}(t-2^{-j}n) \psi_{2^j}(t-2^{-j}m)] = \delta_{m,n} \quad (3.2)$$

Hence

$$\langle f_j(t), g_j(t) \rangle = \sum_n \sum_m D_{2^j}^n(f) D_{2^j}^m(g) \delta_{m,n} = \sum_n D_{2^j}^n(f) D_{2^j}^n(g) \quad (3.3)$$

This shows that correlation of two signals in a frequency band corresponding to an octave of multiresolution decomposition can be efficiently obtained as scalar product of vectors of wavelet coefficients from given scale.

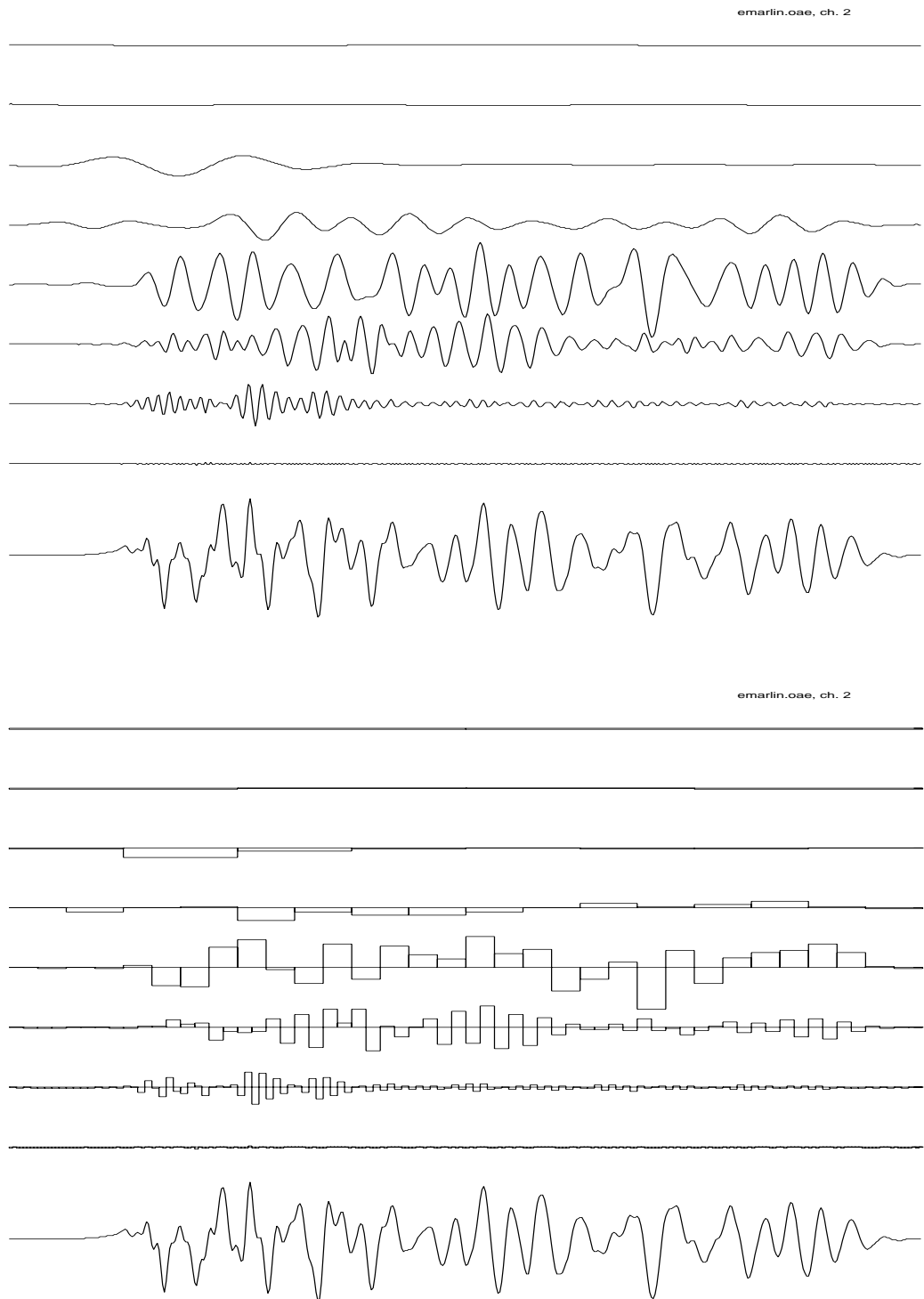


Figure 12 Multiresolution decomposition of an otoacoustic emission; upper part - reconstructed levels, lower part - wavelet coefficients. Border conditions for WT are set as zero outside the measurement window.

3.3. Wavelet packets

Closer investigation of Figure 3 can bring up a question: why are we decomposing only the approximated signals A , leaving the detail signals D apart? Decomposition of the detail signals as well is the main idea of the wavelet packets approach (Coiffman et al 1993). Coefficients obtained in such a way constitute a redundant representation. It contains 2^N orthonormal bases (N - number of points in analyzed signal). The best basis algorithm relies on choosing one of those bases according to certain criterion. The most frequently used is the criterion of minimum of entropy of the representation.

The basis is adapted in a dyadic procedure to the whole analyzed segment. Choice of basis is usually driven by transients of the highest energy, at the cost of representation of weaker structures. Comparing to orthogonal wavelet representation the wavelet packets are surely a step toward the adaptivity of representation. However, with this step we lose one of the advantages given by fixed basis - parameterization ready for statistical comparison. As will be presented in chapter 4, the wavelet coefficients calculated in fixed orthonormal basis can be organized in vectors describing each of analyzed signals in the same space. Such vectors can be used directly as an input for statistical procedures and for comparison of signal's features. In case of wavelet packets the basis is tailored separately for each signal, therefore each signal is described in terms of other coefficients and their comparison is not straightforward. Nevertheless, this problem is present in all the signal-adaptive methods, and as such can be hardly considered a drawback. The computations can be based upon algorithms described in section 2.2, yielding fast implementations which constitute one of the main advantages of wavelet packets among signal-adaptive methods.

Figure 13 presents results of a wavepacket decomposition of the simulated signals. Although in each case an optimal basis is chosen for the signal, even in Figure 13 *a*) [decomposition of the signal without the noise addition] we observe that the positions of strongest coefficients do not correspond exactly to positions - especially in time - of transients present in the signal. An exception is the Dirac's delta, represented with high accuracy. The sine wave running through all the signal is localized with much finer frequency resolution than in case of the multiresolution wavelet decomposition [Figure 8 *a*)]. Addition of noise in Figure 13 *a*) deteriorates the resolution and detectability of signal's structures.

In spite of the advantages offered by an orthonormal time-frequency basis, the wavelet packets were not chosen in this study for the analysis of EEG transients. From this point of view the main drawback lies in the fact that the basis is adapted globally to the whole analyzed epoch. Therefore representation of weaker transients can vary depending on the energy and morphology of other signal's structures. However, the orthogonality of representation can become extremely important e.g. in the investigation of inter-channel dependencies or in cases requiring fast computations.

3.4. Wavelet networks

The name "wavelet networks" proposed by Zhang and Benveniste (1992) relates to single-layer feedforward neural network, where the threshold functions of nets' neurons are replaced by wavelets, generated by scaling and translating one basis function. This approach can produce extremely efficient results in certain function approximation tasks. However, a general choice of initial parameters of the network - the number of "wavelons" and their initial positions and widths - still constitutes an open question. Therefore the representation depends on these initial conditions, not always being the optimal one from the point of view of available functions. Therefore wavelet networks seem to be in the stage of development premature for general signal processing applications.

Figure 14 presents an example of poor approximation of a function by wavelet network, in case where the initial parameters - such as number of "wavelons" - were not chosen especially for the studied case. Results of approximation by 100 wavelons in 50,000 iterations are shown. The function being approximated is the signal *IV* from Figure 5, without the sine component, because a reasonable approximation of a such a sine requires a large number of wavelons. Poor approximation presented in this picture doesn't suggest a generally erratic behavior of wavelet networks. Proper choice of initial settings, e.g. for certain class of signals, could produce much better approximation. Such case is not shown, since the two lines representing signal and it's approximation in Figure 14 would be inseparable.

In spite of their adaptivity, the wavelet networks research in this study remained in the stage of simulations. An application to EEG analysis would require an arbitrary setting of the mentioned above initial conditions.

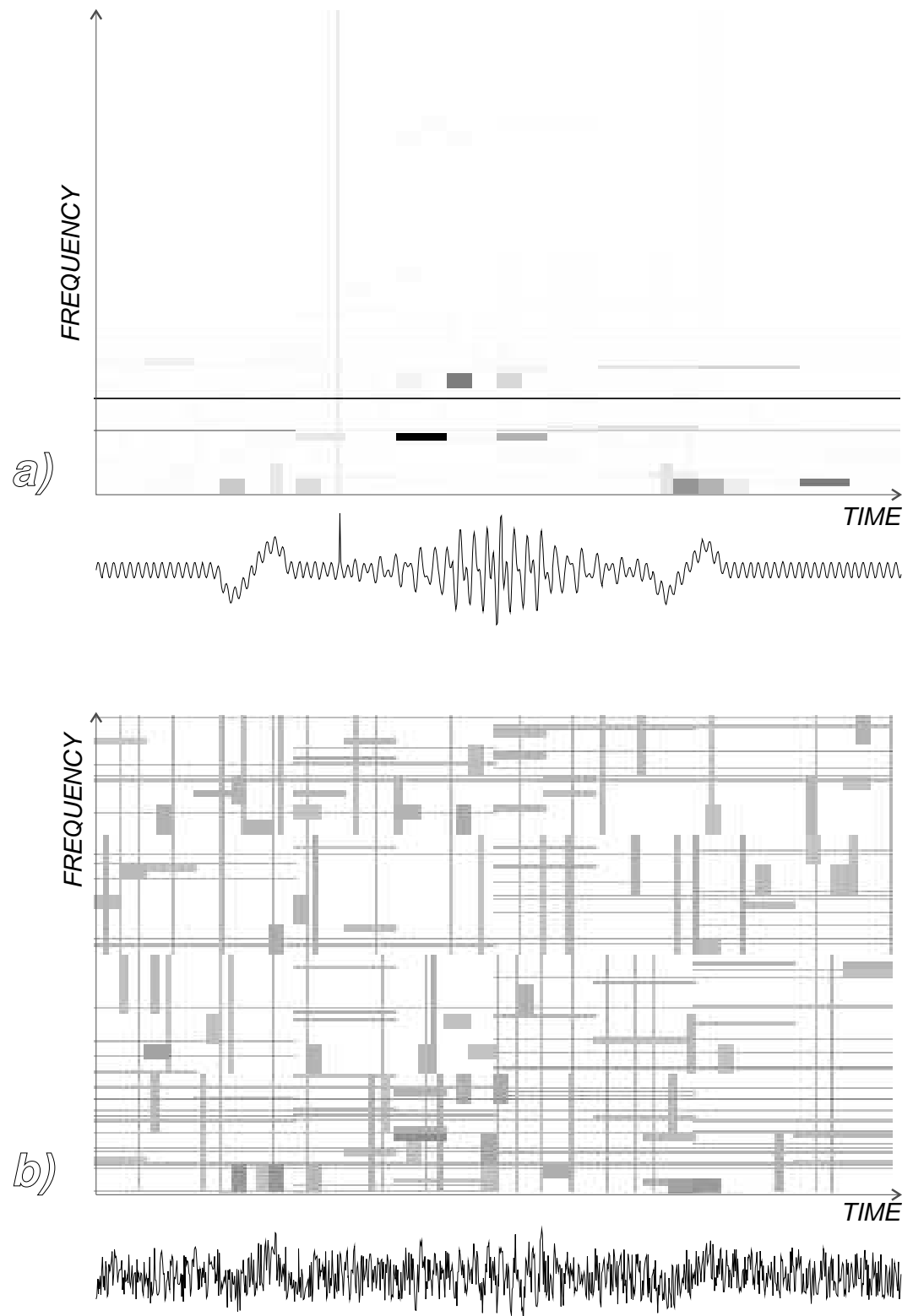


Figure 13 Wavelet packets decomposition of the simulated signals IV [a] and VI [b] from Figure 5.

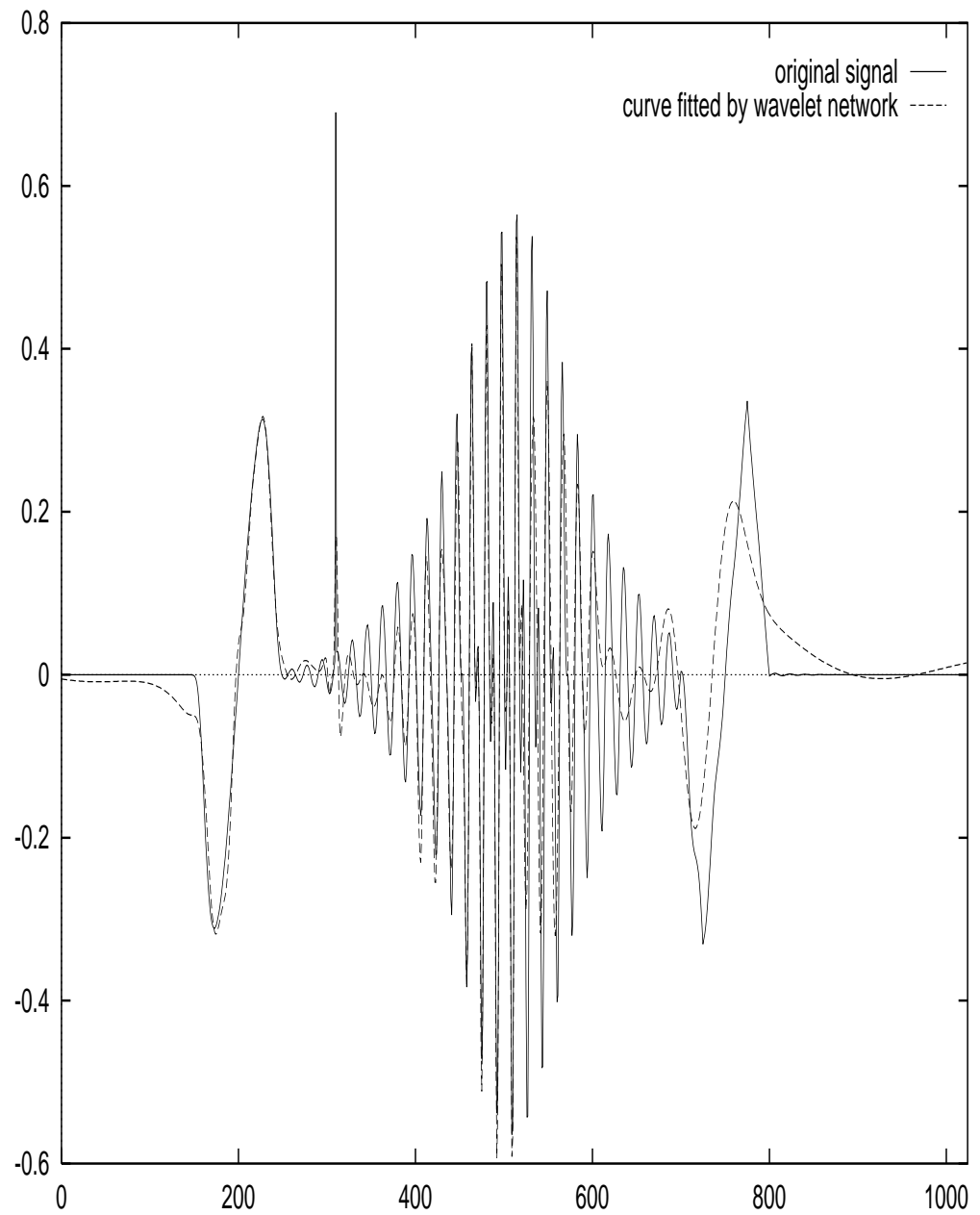


Figure 14 Results of approximation [dashed line] of simulated signal IV from Figure 5 without the sine component [solid line] by a wavelet network of 100 wavelons in 50,000 iterations.

3.5. Matching Pursuit with real discrete Gabor dictionary

EEG recordings that we process numerically are real discrete time series. For analysis of such signals we can construct a dictionary of real time-frequency atoms generated accordingly to eq. (2.12):

$$g_{(\gamma, \phi)}(n) = K_{(\gamma, \phi)} g_j(n-p) \cos(2\pi \frac{k}{N} n + \phi) \quad (3.4)$$

The index $\gamma = (j, k, p)$ is a discrete analog of $I = (\xi, s, u)$ from eq. (2.12). If we assume that analyzed signal has $N = 2^L$ samples, where L is an integer, then $0 \leq j \leq L$, $0 \leq p < N$ and $0 \leq k < N$. Parameters p and k are sampled with an interval 2^j . Such a limited choice of parameters, resembling the dyadic sampling of the time-frequency space in multiresolution wavelet analysis, is a result of tradeoff between accuracy of the representation and computational complexity. Figure 18 presents resulting sampling of the octave-frequency space in such a dictionary. We notice that atoms with longer time span [higher octave] have finer sampling in the frequency domain.

Parameter ϕ , that in eq. (2.12) was hidden as a phase of the complex number, here appears explicitly. The value of $K_{(\gamma, \phi)}$ is such that $\|g_{(\gamma, \phi)}\| = 1$. Integrating this formula [in continuous approximation] yields

$$K_{(\gamma, \phi)} = \frac{2^{\frac{1}{4}}}{\sqrt{2^j \left[1 + e^{-\frac{\pi 2^{2j-1} k^2}{N^2}} \cos\left(\frac{4\pi k p}{N} + 2\phi\right) \right]}} \quad (3.5)$$

The size of this dictionary (and the resolution of decomposition) can be increased by oversampling by 2^l ($l > 0$) the time and frequency parameters p and k . The resulting dictionary has $O(2^{2l} N \log_2 N)$ waveforms, so the computational complexity increases with oversampling by 2^l . Time and frequency resolutions increase by the same factor:

$$\Delta t = 2^{-l} \frac{2^j}{f_s} \quad (3.6)$$

$$\Delta f = 2^{-l} \frac{f_s}{2^j} \quad (3.7)$$

where f_s - sampling frequency of analyzed signal. Resolution here is understood as the distance between centers of dictionary's atoms neighboring in time or frequency. It depends on the octave j , which corresponds to the "width" of atom in time and frequency. The time span of dictionary's atoms defines our ability to measure the time width of signal's structures represented by these atoms. We can define "width" of a time-frequency atom as a half-width of the window function $g_j(n)$:

$$T_{1/2} = 2 \frac{2^j}{f_s} \sqrt{\frac{\ln 2}{\pi}} \quad (3.8)$$

It changes with every octave j by a factor of 2, independently of described above oversampling.

Figure 15 *a)* presents Wigner plot obtained from MP decomposition of the simulated signal *IV* from Figure 5, plotted at the bottom. We observe a perfect representation of the sine wave, Dirac's delta and two Gabor functions [F, E, C, D], representing waveforms present in the dictionary. Structures A and B are represented by groups of atoms. Addition of noise in Figure 15 *b)* does not significantly deteriorate the resolution.

3.5.1. Amplitude of a discrete Gabor function

The magnitude $\langle R^n f, g_{I_n} \rangle$ [eq. (2.15)] calculated by the algorithm for each of selected atoms is called *modulus*. It represents the amount of signal's energy explained by a particular waveform. However, in some cases we may need the value of structure's amplitude. Relation between the modulus and amplitude of window function of an atom from the Gabor dictionary - eq. (3.4) - is given by eq. (3.5). However, this formula gives the amplitude of the **window function**. The actual peak-to-peak amplitude of corresponding Gabor function can be lower, depending on its frequency, phase and octave parameters. Figure 16 presents examples of Gabor functions from dictionary constructed for 2048-point segment. Amplitudes of the window function $[K_{(\gamma, \phi)}, \text{eq. (3.4)}]$ was set to 1 for all the plotted waveforms. Difference between

the amplitude of a Gabor function and amplitude of its window function introduced by discrete sampling can be observed on Figure 16 *g)* and *h)*, where sampling misses the extrema of modulated sine. On plots *c)* and *d)* in Figure 16 the maxima of low-frequency oscillations fall far from the maximum of the window function, resulting also in Gabor's amplitude lower than 1.

Figure 17 presents the relative difference between the doubled amplitude of the window function g from eq. (3.4) and the actual peak-to-peak amplitude of the discrete Gabor function in the frequency-octave space. Calculations were performed for all the octaves and frequencies of atoms that would form a complete discrete Gabor dictionary for a 2048-point segment, and averaged over 1099 random phases. Note that only a subset of points in this plane represents atoms actually present in the dictionary used in calculations - compare Figure 18.

For this dictionary exists a fast numerical implementation of Matching Pursuit, described by Mallat and Zhang (1993). It was used for numerical experiments in chapter 4.3. Oversampling parameter l was set to 3.

3.5.2. Number of waveforms in the expansion

Another practical issue is related to the fact that in practice we do not compute infinite expansions in the form of eq. (2.18). The iterations must be stopped at some point. Number of waveforms in the expansion can be e.g. based upon the percentage of signal's variance explained by the decomposition, or fixed. Nevertheless, it is worthwhile to take a closer look at the behavior of the signal's residues in each iteration.

The MP approximation is non-linear and the residues, not the signal, are being decomposed at each stage of the iterative process. Their norm converges to zero, as stated in eq. (2.17). However, asymptotic properties of residues are the key to understanding convergence properties of the MP. As postulated in (Davis et al 1994a) the Matching Pursuit is a chaotic map. It was proven for a particular type of dictionary (Davis et al 1994b) and was confirmed by the numerical experiments. If we renormalize the residues at each step, to prevent their decay to zero, the renormalized residues converge to realizations of a process that we call a dictionary noise. Realizations of dictionary noise are signals, for which the products with the dictionary's elements are uniformly small. At a certain point of the iterative procedure we reach a stage when a residue is a realization of the dictionary noise. This corresponds to the situation when all the structures coherent with the dictionary, giving relatively

large products with dictionary's elements, were removed in previous iterations. Or, in other words, such a residuum has no structure that would be particularly coherent with respect to the dictionary. In practice this behavior of the iterative procedure can be traced via a magnitude $\lambda(n)$ - the proportion of the energy of residuum $R_n f$ explained by g_{I_n} :

$$\lambda(n) = \frac{\langle R^n(f), g_{I_n} \rangle}{\|R^n(f)\|} \quad (4.15)$$

$\lambda(n)$ converges to a constant value depending on the size of a signal. Reaching this value corresponds to the mentioned above situation, when the distribution of residuum's products with the dictionary waveforms is flat. Figure 19 presents decay of λ , together with the energy of the residuum, versus number of algorithm's iterations. Dotted line gives the percentage of total signal's energy explained by subsequent iterations. This value corresponds to $\lambda(n)$, but at each step is normalized to the total signal energy, not energy of the residuum. Figure 19a presents these curves for a typical EEG segment of length 2048 points. One can observe that at the right side of the plot, in the region where the λ curve becomes flat, there is very little energy left in the residuum. That indicates that the Gabor dictionary is generally coherent with most of the signal's structures. Figure 19b shows the same plot for an EMG [electromyogram, electrical activity of muscles] epoch from the same experiment, sampled also 102.4 Hz. We observe that $\lambda(n)$ becomes flat very soon [around 40 iterations], while both the remaining curves, absolute percentage of energy explained in given iteration and energy of the residuum, decay very slowly. That indicates low coherence of this signal with the Gabor dictionary: after few initial iterations, while there is still a lot of signal's variance left to explain, the distribution of signal's products with the dictionary atoms becomes flat and no structures are particularly coherent with the dictionary. Wigner map for this EMG epoch is presented in Figure 20. One of the most coherent structures is the mains artifact at 50 Hz. Such a low information content of this signal can be result of a sampling frequency too low for EMG, tuned rather for the EEG channels, and the nature of EMG signal itself.

Figure 21 presents Wigner plots of a typical EEG segment in case when a) 50, b) 100 and c) 200 atoms were taken into account. It shows disadvantages of plotting distributions for too many atoms. In Figure 21 c) the clear visibility of main EEG structures from a) and b) is deteriorated mainly by the presence of structures related to noise components. Moreover, 50 atoms from a) explain almost 95% of energy.

3.5.3. Heuristics in practical realizations

In the brief description of MP algorithm in section 2.4 we stated simply that at each step of the iterative procedure a vector g_{I_n} is chosen, which gives the largest product with the residuum $R^n f$:

$$|\langle R^n f, g_{I_n} \rangle| = \max_I |\langle R^n f, g_I \rangle| \quad (4.17)$$

Indeed, since the dictionary constructed for a discrete finite signal has finite number of waveforms, this condition is fulfilled by at least one of them. However, in practice the choice of "best" waveform at each stage is based upon certain heuristic. A straightforward implementation of the above procedure of choice, being already a compromise in favor of lower computational complexity, would still require a huge amount of computing resources. It is enough to consider e.g. phase, continuous by nature, present explicitly in the real time-frequency atoms in the Gabor dictionary. Reasonable sampling of this parameter would produce a huge dictionary even for relatively small dimensions of the signals space [equal to the number of points in analyzed signal]. Therefore, in order to make the algorithm suitable for practical application, certain heuristic optimizations of the procedure of choice are being implemented. Since the method provides by its nature a sub-optimal solution, this problem does not constitute itself a major drawback, if the chosen heuristic gives reasonable results. However, we must be aware of this fact if we want to compare results obtained by means of different implementations of MP. If the implemented optimizations differ even slightly, the differences accumulate with every iteration, since the expansion is non-orthogonal.

The problem of optimal heuristic for MP is being currently investigated. Preliminary results suggest that we might be able to tune the procedure of choice to enhance desired signal features, like e.g. the EEG morphology as perceived by visual analysis. We believe that this research together with development in mathematics and decreasing cost of computations will make MP-based algorithms a generally acceptable parametrization for biomedical signals.

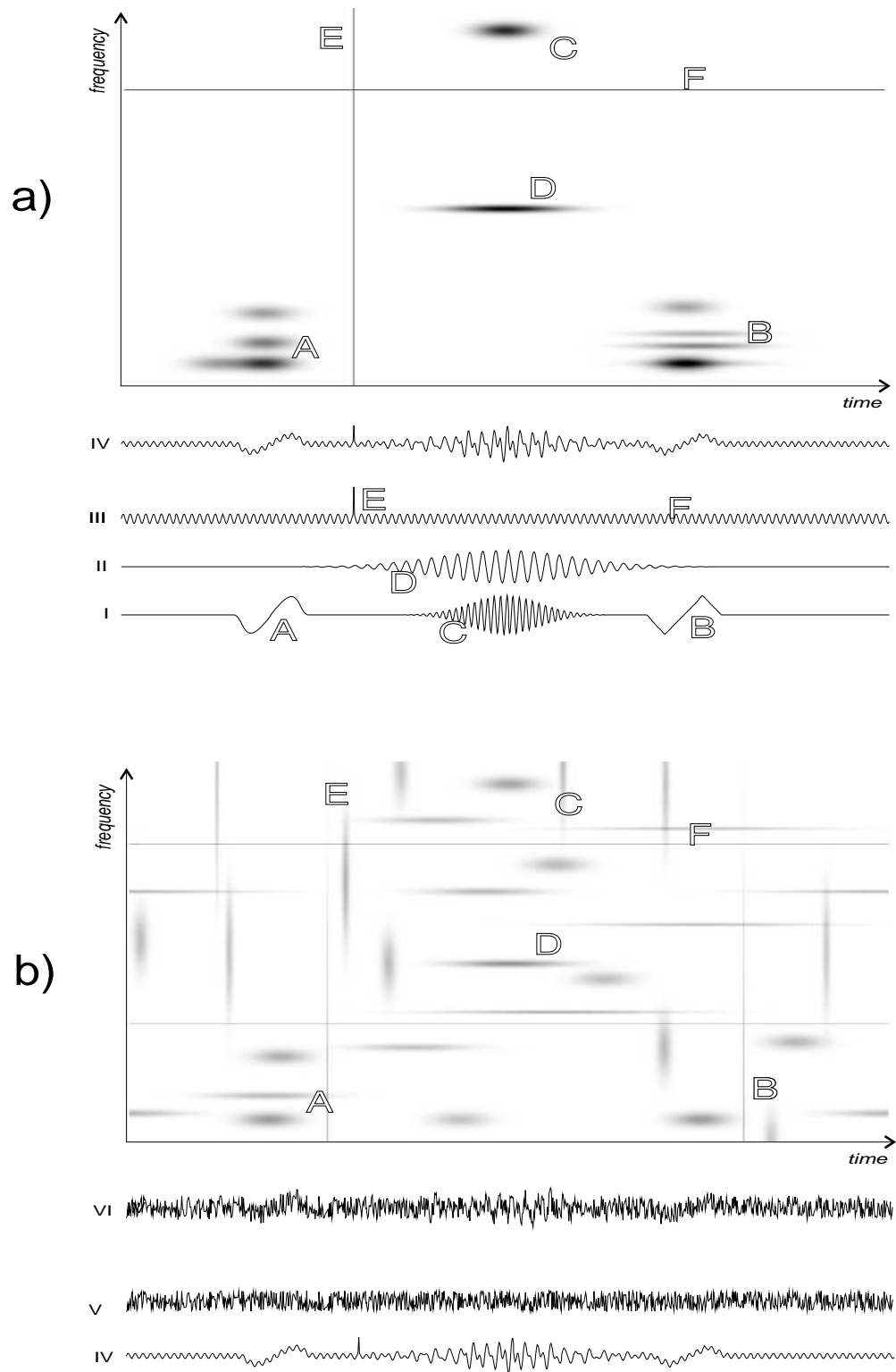


Figure 15 Wigner plots obtained by means of MP for the simulated signals shown below [compare Figure 5]. Letters mark signal structures and corresponding atoms or groups of atoms.

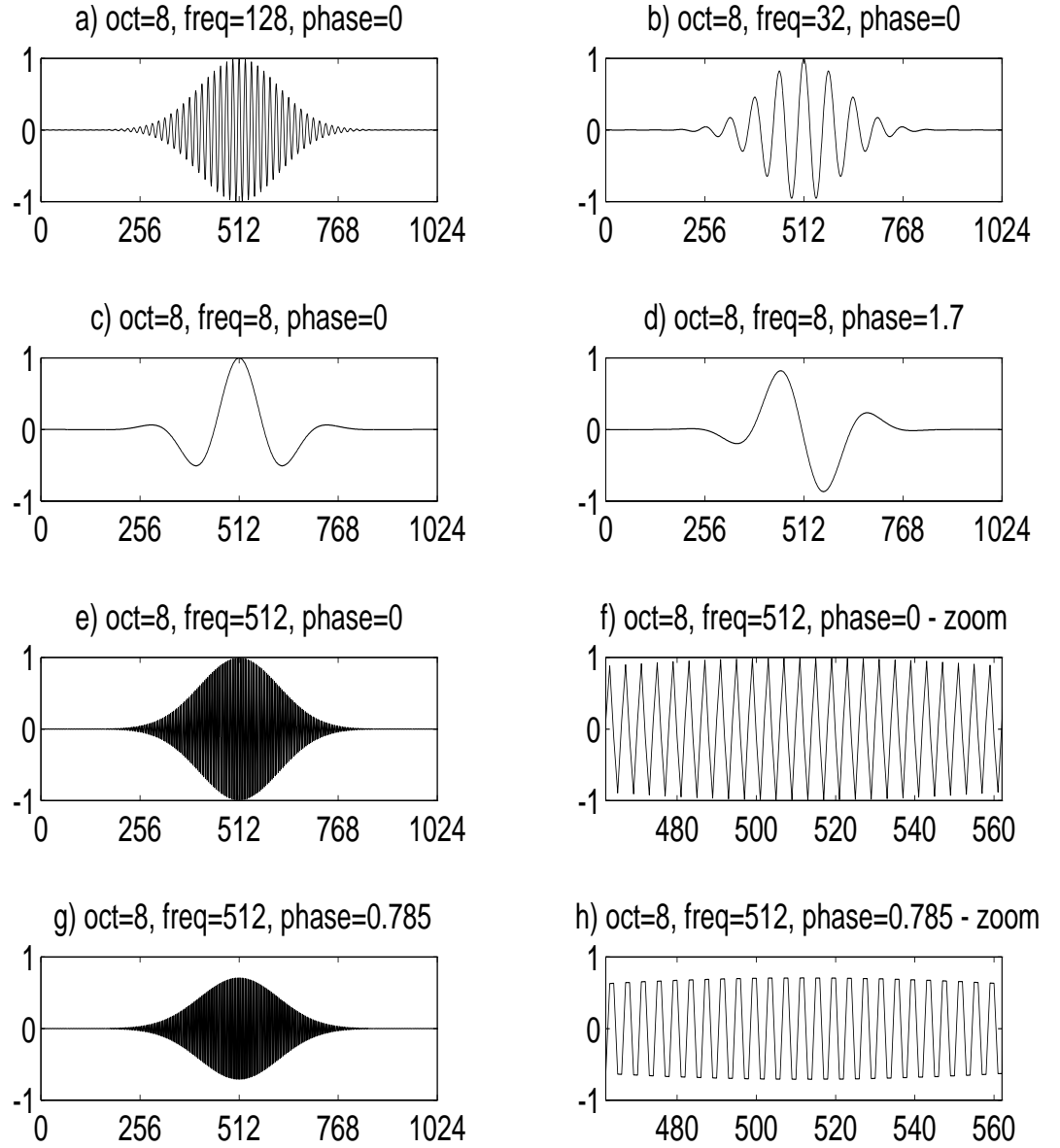


Figure 16 Examples of Gabor functions from a dictionary constructed for 2048-point segment. Amplitude of the window function $[K_{(f,\phi)}, \text{eq. (3.4)}]$ set to 1.

$(2\text{-max+min})/2$, averaged over 1099 random phases in Gabor functions

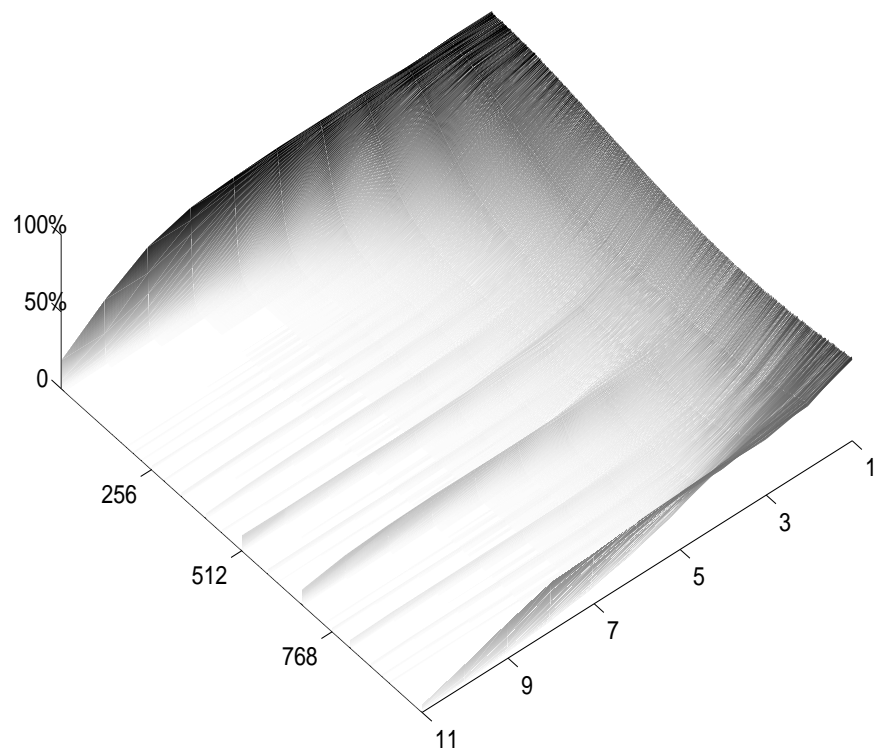


Figure 17 Relative difference between the [doubled] amplitude of the window function and the actual peak-to-peak amplitude of discrete Gabor. Right axis - octaves [1-11], left - frequency in general units.

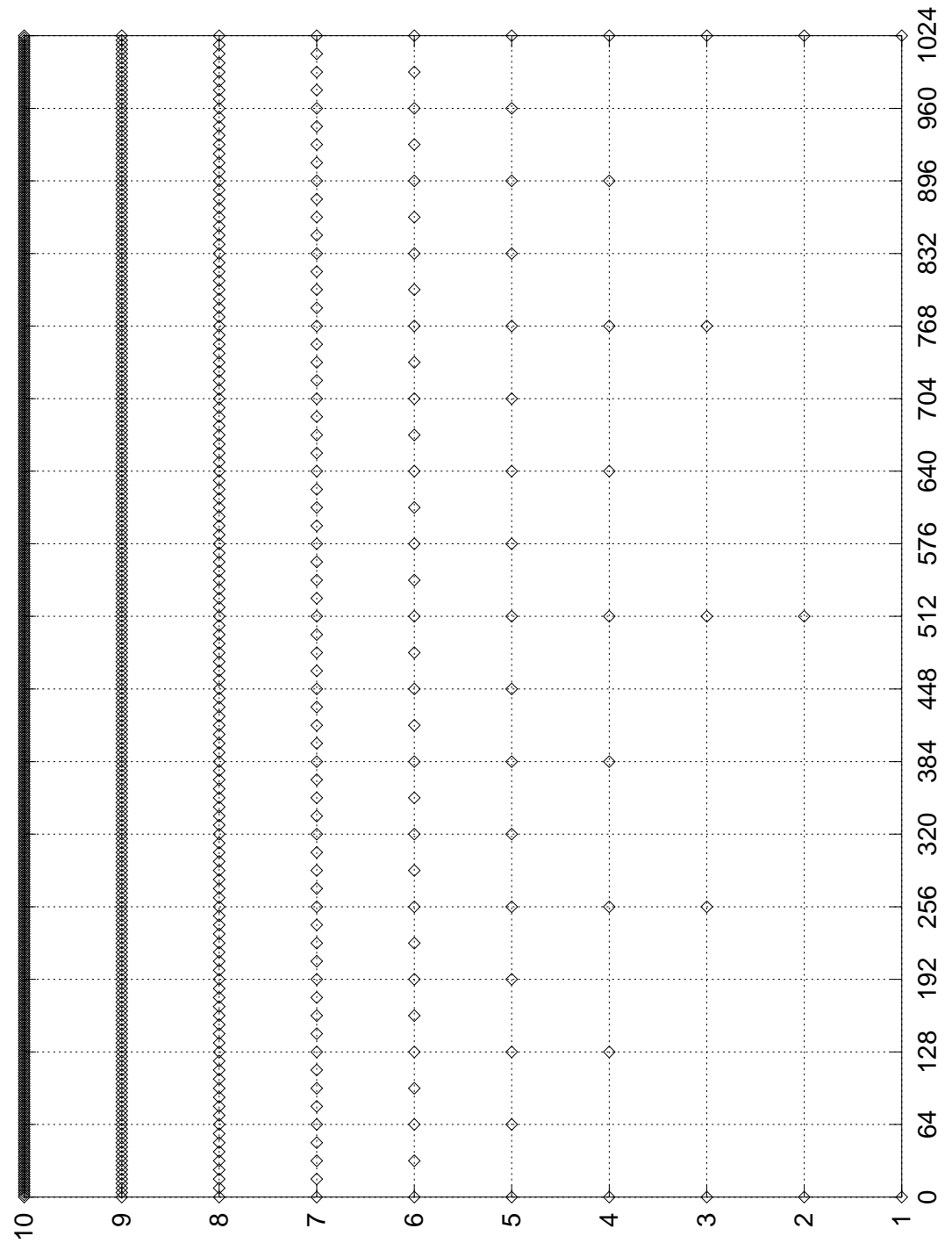


Figure 18 Sampling of the frequency [horizontal axis, 0-1024] - octave [vertical axis, 1-10] space in the limited Gabor dictionary discussed in chapter 3.5.

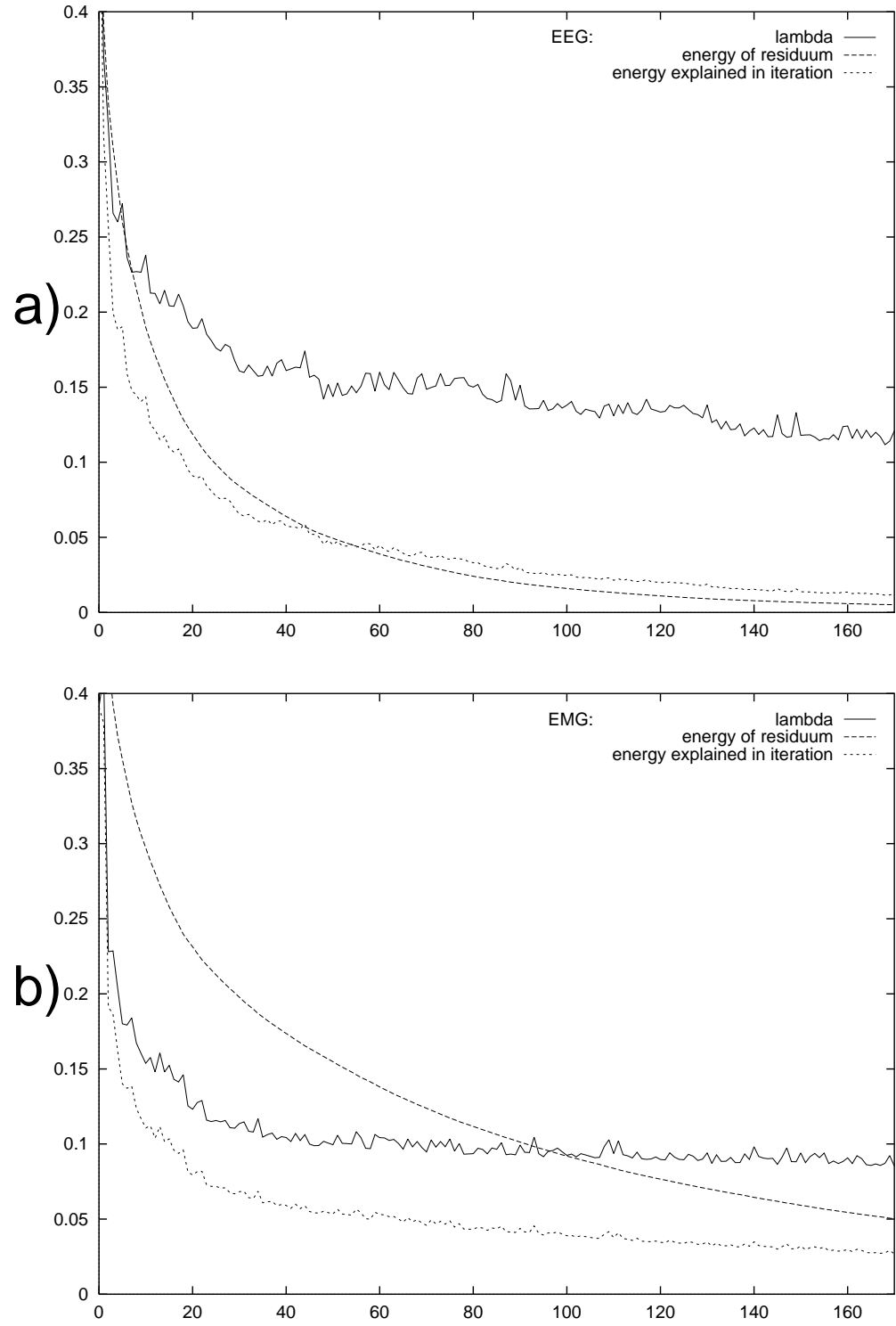


Figure 19 λ [eq. (4.15), solid line] and energies: remaining in residuum [dashed] and explained in iteration [dotted line] relative to signal's energy, versus number of iterations; a) EEG b) EMG

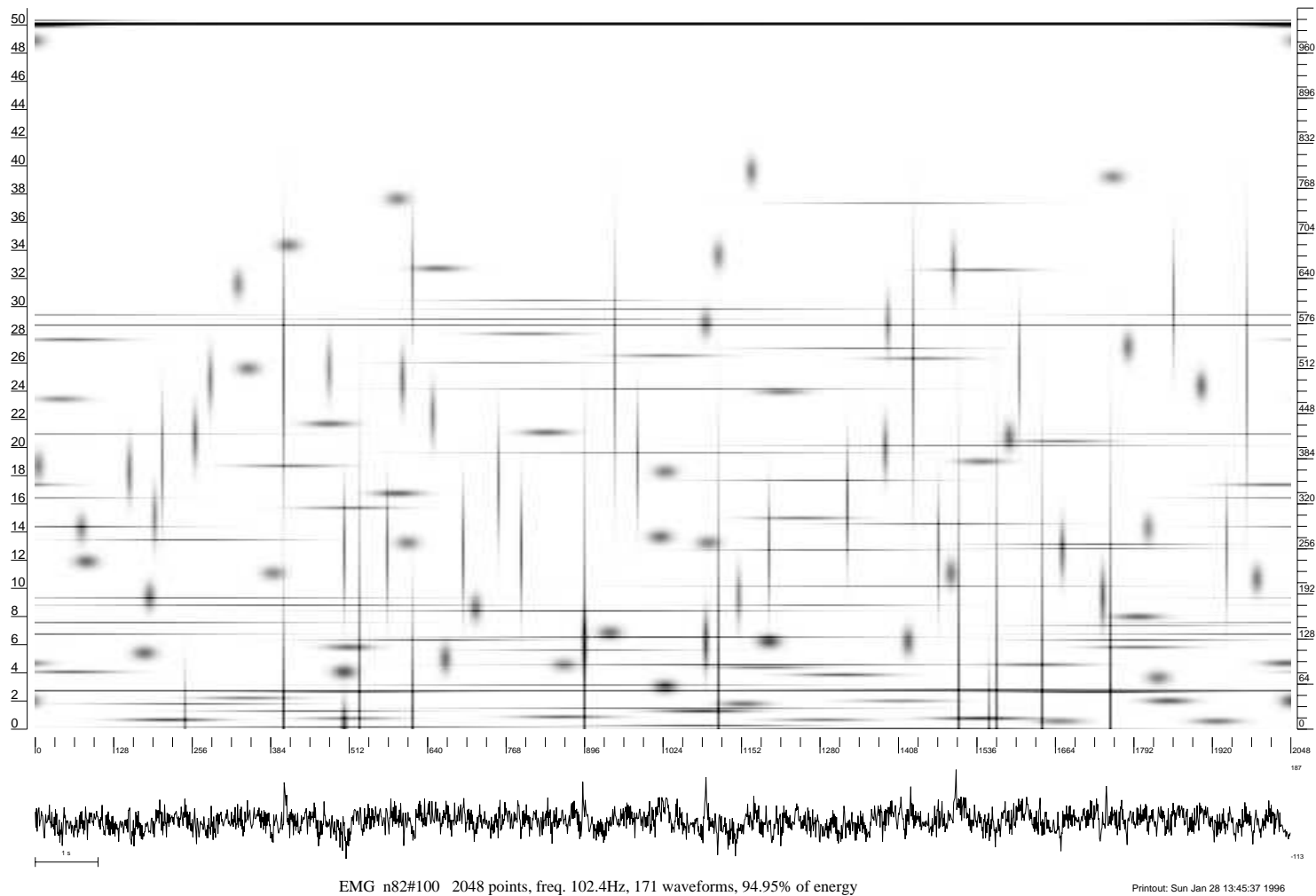


Figure 20 Wigner plot for the EMG signal, for which the decay of λ was plotted in Figure 19b.

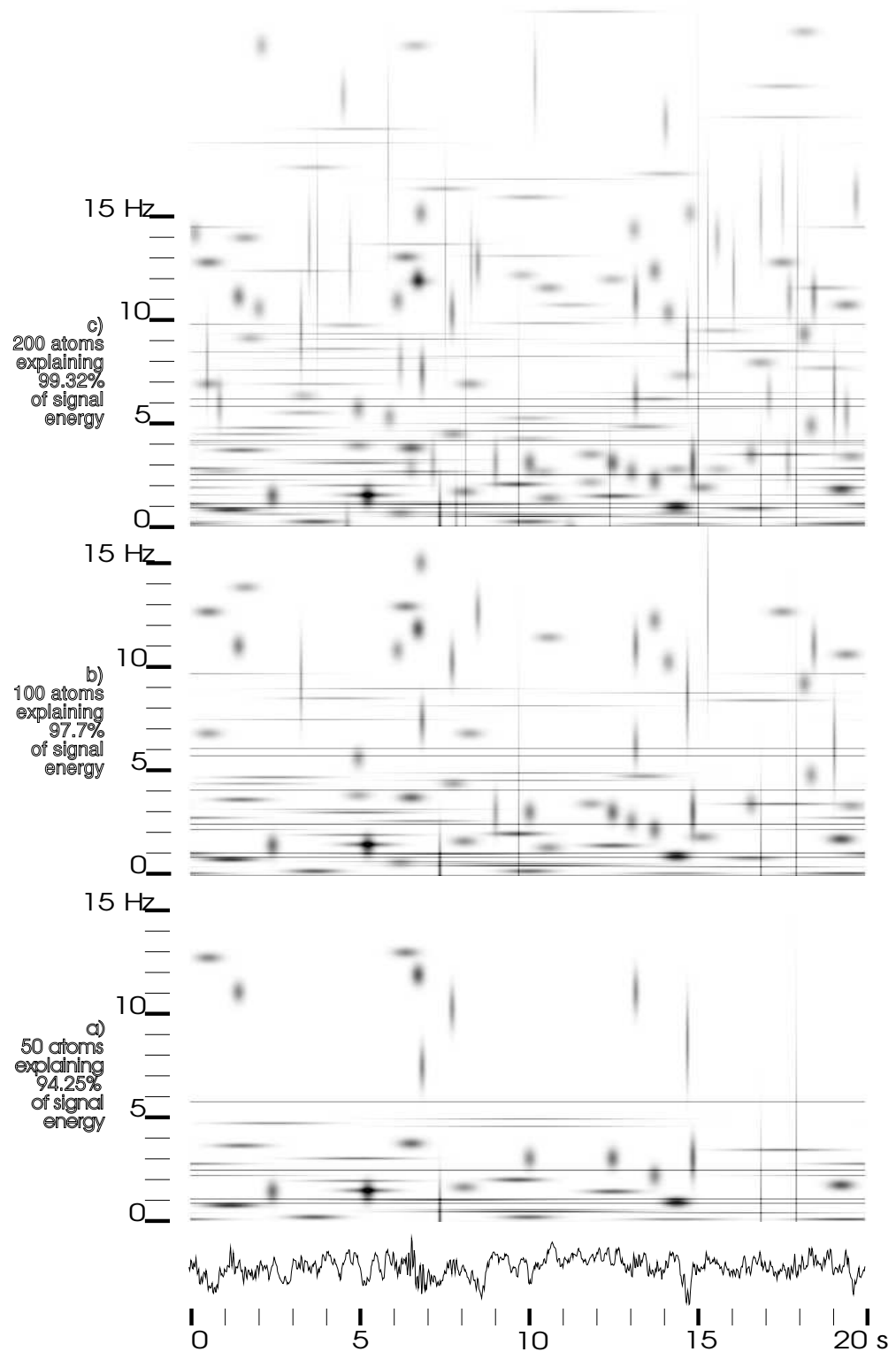


Figure 21 Wigner plot for an EEG epoch 20 sec long [below] presented in cases where a) 50, b) 100 and c) 200 atoms (iterations) were taken into account.

Chapter 4.

Results and discussion

At the beginning of section 4.1 results from (Bartnik et al 1992) and (Bartnik, Blinowska and Durka 1992) are quoted.

Experimental data and physiological background for the analyses described in section 4.1.1 were provided by prof. R. Tarnecki from the Nencki Institute of Experimental Biology in Warsaw.

Numerical experiments with neural networks described in section 4.2 were performed with the Aspirin / Migraines software package by Russel Leighton from Mitre Corporation, available at <ftp://pt.cs.cmu.edu/afs/project/connect/code/am6.tar.Z>

Physiological data and consultations for chapter 4.3 were provided by prof. W. Szelenberger from Warsaw Medical School, dept. of Psychiatry.

Calculations of the MP decomposition were performed by the 'mpp' software package by S. Mallat and Z. Zhang, downloaded via anonymous ftp from <ftp://cs.nyu.edu/pub/wave/software/mpp.tar.Z>

Examples given in this chapter can serve as methodological frameworks for a large class of problems encountered in biomedical signal processing.

4.1. Evoked potentials studies

Evoked potentials are signals an order of magnitude smaller than the background EEG and their shape is found by means of averaging the trials triggered by a repeated stimulus. Validity of the averaging approach is based on unfulfilled assumptions concerning independence of both signals, repeatability of EP and purely stochastic character of on-going EEG. Application of WT made possible to overcome the difficulties related to the averaging procedure. Namely in (Bartnik and Blinowska 1992) the multiresolution decomposition was applied to single auditory evoked potentials and to epochs of background EEG. In the space of wavelet coefficients statistical analysis was performed in order to find differences between EEG and EP recordings. It was found that the confidence level of discrimination 10^{-5} may be obtained for only five wavelet coefficients. In (Bartnik, Blinowska and Durka 1992) reconstructions of single evoked potentials from wavelet coefficients were performed. Figure 22 presents reconstruction of ten first single trials from coefficients differentiating EEG and EP. Above each consecutive trial [solid line, lower part] its reconstruction [solid, thicker line] is drawn on the background of the average [dotted line] of all the 55 single trials of length 512 msec each. One can observe the higher or lower similarity of these reconstructions to the average, depending on the trial. There is also at least one case, where it seems that the response failed to appear.

4.1.1. Investigation of the influence of cerebellar lesions

Somatosensory evoked potentials [SEP, elicited by electrical stimulation of cat's paw] were registered by means of silver ball electrodes positioned on pericrucial cortex of anaesthetized cat. Recordings were performed before and after removal of a part of cerebellum. Spontaneous EEG as well as 92 repetitions of SEP were registered from 8 derivations: F7, F3, C3, P3, O1, F8, F4, C4, P4, O2. The experimental conditions resulted in four groups of recordings: evoked potentials before the lesion, spontaneous EEG before the lesion, evoked potentials after the lesion and spontaneous EEG after the lesion. Wavelet parameterization was computed for each of 92 segments representing each of the four mentioned groups. The Mann-Whitney test was applied in the space of computed wavelet coefficients. The hypotheses of difference between each pair of mentioned groups were tested for each of the wavelet coefficients separately.

Figure 23 presents pattern of wavelet coefficients for which the hypothesis of difference stands at confidence level 0.01. Shaded rectangles [shifted slightly towards upper left] mark wavelet coefficients differentiating EP from EEG. Black rectangles [lower right] indicate differences between EPs before and after the lesion. Empty rectangles mean no significant differences.

Closer investigation of several plots corresponding to Figure 23 allowed to draw the following observations:

1. Differentiation between evoked potentials and spontaneous activity, performed for recordings before as well as after the lesion, brought results corresponding to those described above (Bartnik and Blinowska 1992). Best discrimination occurred for early components from scales (s) 2^2 , 2^3 and 2^4 corresponding to the frequency bands 250-125 Hz, 125-62 Hz and 62-31 Hz respectively. Statistical differences between pure EEG and SEP recordings elucidated the influence of stimuli on SEP. Reconstructions of single trials from these coefficients resulted in shapes related to the average, analogically to the situation from Figure 22.
2. SEP recordings before and after the lesion were generally best discriminated by the same wavelet coefficients as the coefficients differentiating SEP from EEG (before as well as after the lesion). This effect is presented for the first eight electrodes in Figure 23.
3. No statistical differences were found in spontaneous EEG recordings before and after the lesion.

From this analysis follows that the brain activity changed by the lesion was mainly the evoked activity, while the spontaneous EEG before and after the lesion revealed no statistical differences. This relates also to the spontaneous activity present in the background of the evoked potentials segments. The differences introduced by the lesion in these recordings were located in the same time-frequency regions as the differences between evoked potentials and spontaneous EEG, which suggests that the only activity influenced by the lesion was the evoked activity, while the spontaneous EEG remained unchanged.

Wavelet transform offered description of evoked potentials in terms of coefficients reflecting their morphological features. Changes introduced by lesion were detected in the time-frequency space without prior assumptions concerning properties of the signals.

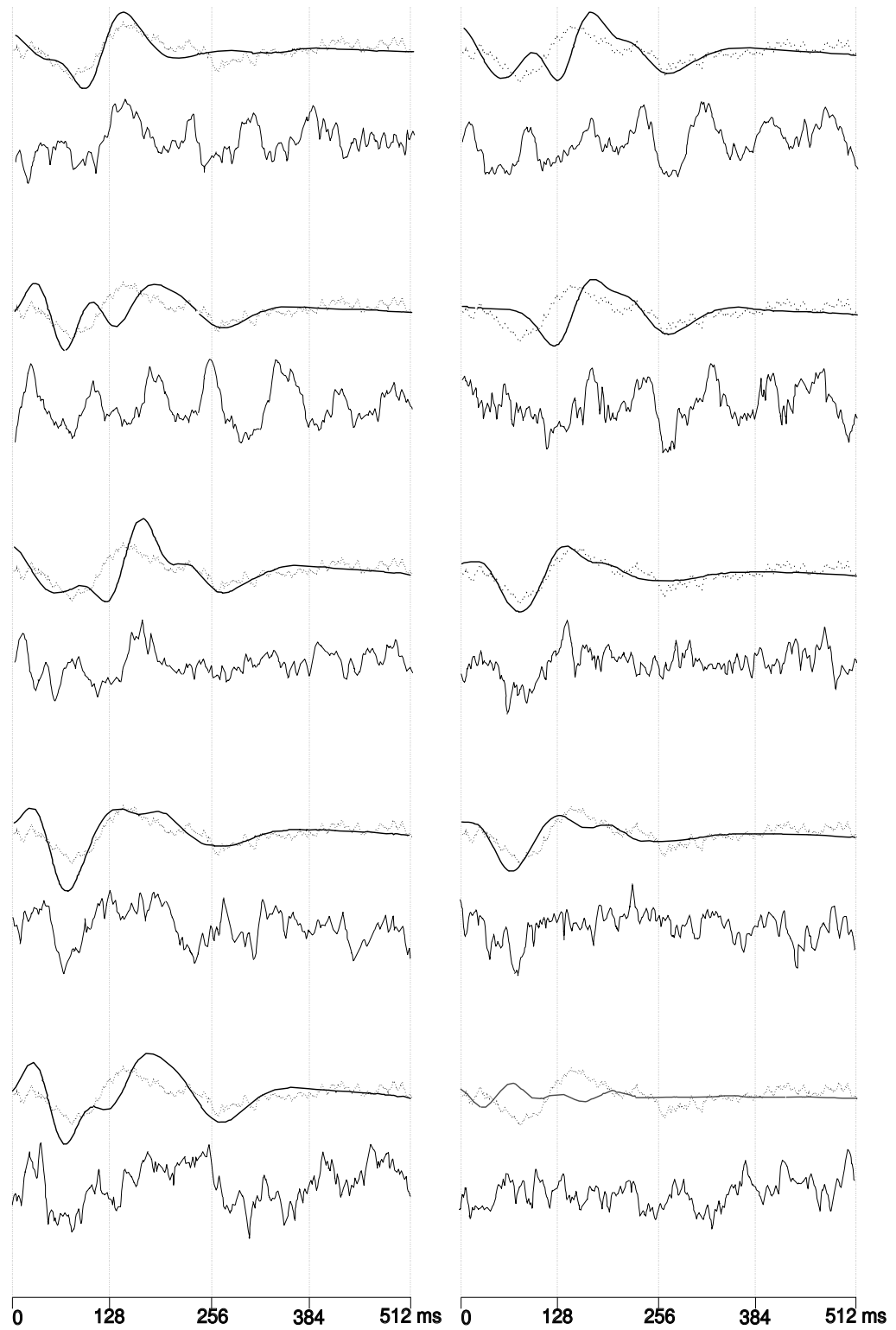


Figure 22 Reconstructions of single evoked potentials from 5 coefficients differentiating statistically SEP from the on-going EEG. Bottom - raw recording, upper solid - reconstructed EP, dotted - average of the 55 trials.

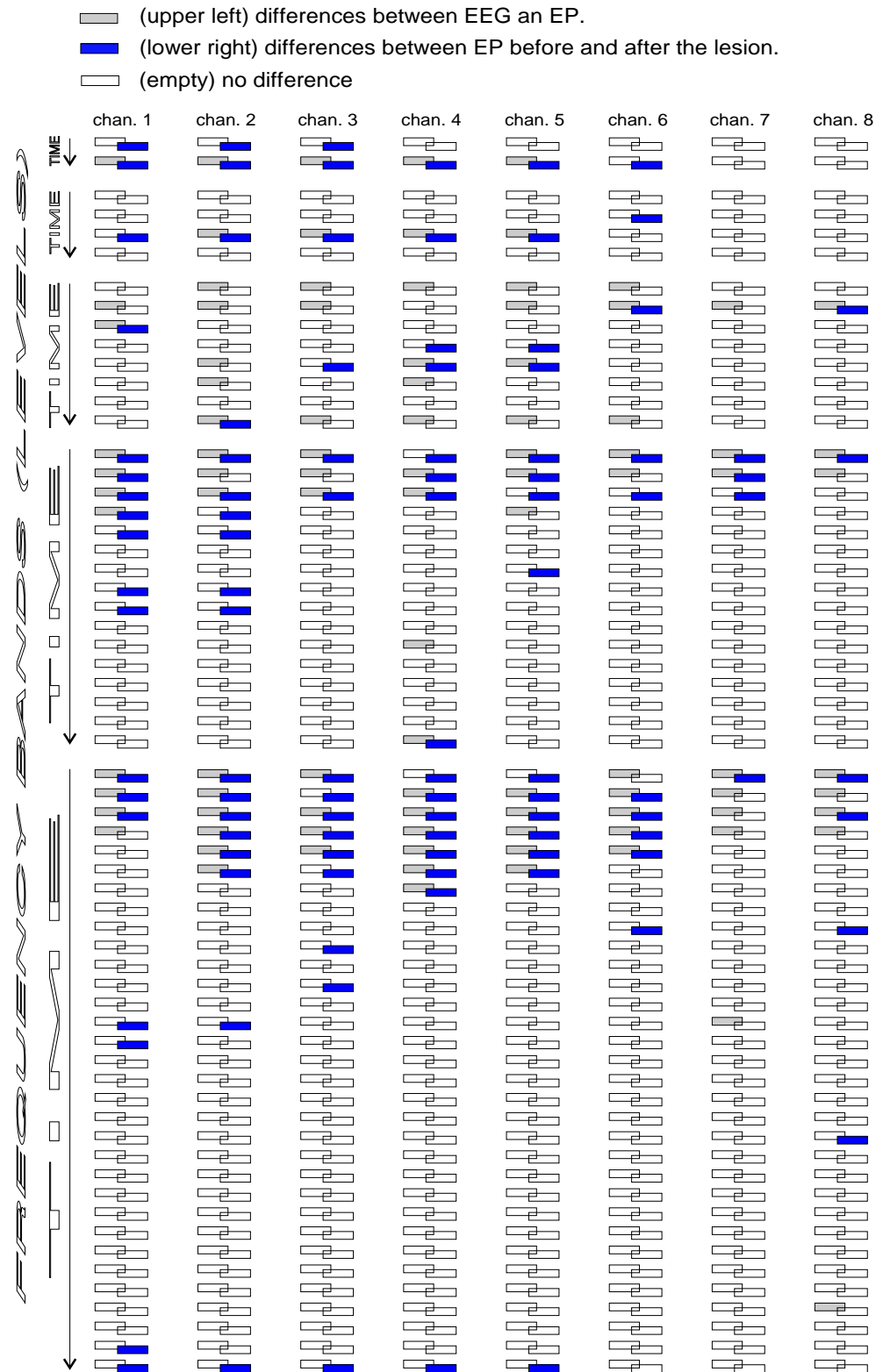


Figure 23 Results of discrimination between SEP and EEG in the space of wavelet coefficients.

4.2. Detection of EEG artifacts by artificial neural network

When applying an artificial neural network (ANN, par. 2.3) to classification of segments of EEG recordings, we encounter the problem of choosing proper preprocessing of the time series before feeding input to the first layer. Orthogonal wavelet transform is a good candidate for the preprocessing tasks due to fast implementations [$O(N)$] and correspondence of wavelet coefficients to the time-frequency energy content.

The classification performance of four artificial neural networks was tested on segments of multichannel EEG recordings of 2.5 sec length. Each of the segments was assigned expert's binary decision: artifact or non-artifact. Artifacts were marked for the purpose of other analyses. Standard polysomnographic channels, 21 channels of EEG according to the 10-20 standard and A1 and A2 derivations were sampled by 12-bit analog-digital converter with frequency 102.4 Hz. 8 hours 38 minutes of recording resulted in 12440 2.5 sec segments. The training set consisted of odd-numbered segments [6220], 2060 of them classified as artifacts. In the testing set [even-numbered segments] 2058 segments contained artifacts.

Backpropagation training of the networks was repeated until tests performed on a subset of the training set showed no significant improvement.

4.2.1. Tested networks

Four different preprocessing schemes were tested. Network's architectures were adapted to the preprocessing:

- A.** In the first approach raw segments of the EEG time series were used as input. Each of the second layer's neurons received input from 7 neighboring signal's samples, with window moved by one point for the next neuron. That resulted in 250 neurons for each 2.5s (256 points) segment, for 27 channels total of 6750 neurons in the first layer. 27 neurons of the third layer received input from all the previous layer's neurons. A single output neuron collected input from all the units of the second layer.

- B.** In the construction of preprocessing for the second network certain amount of *a priori* knowledge about the artifact's nature was engaged. Correlations between electrooculogram and EEG channels [namely EOG1/EOG2, EOG1/Fp1, EOG1/Fp2] were calculated to facilitate detection of ocular artifacts. The rest of total 45 input values consisted of averages and variances calculated for each channel separately.
- C.** Raw wavelet coefficients of each channel's data constituted input for the third of tested networks. The next layer consisted of two sublayers. 27 units of the first sublayer received weighed sum of all the wavelet coefficients from separate channel recordings. Each of 256 units of the second sublayer received one wavelet coefficient (corresponding to specified time-frequency region) from all the 27 channels. The first sublayer was intended to facilitate the network's evolution towards detection of artifacts visible in separate channels, like e.g. the baseline drift. The second sublayer gathered inter-channel dependencies without losing the time-frequency information content provided by wavelet coefficients.
- D.** Based upon the formula (3.3) from paragraph 3.2.4, correlations in low-frequency band (0.4 - 3.2 Hz) were calculated between the electrooculogram EOG1 and the Fp1 derivation of EEG, and between left and right eye's electrooculograms: EOG1 and EOG2. It was expected that their ratio reflects propagation of electrooculogram to the Fp1 channel of EEG. Similar parameters were calculated for the Fp2, F7 and F8 derivations, which are usually most contaminated by this sort of artifacts. Due to calculating the correlation in low frequencies, this parameter was unaffected by the propagation of EEG into the electrooculogram.

For each of the EEG channels the power in the frequency band 25.6-51.2 Hz normalized to the total power reflected the high-frequency (e.g. muscle) artifacts. Similar parameter for the 0-0.8 Hz frequency band reflected low-frequency artifacts, related mainly to breathing. All those parameters were efficiently calculated from orthogonal wavelet decomposition.

Total size of the input layer was 46. Twenty units of the second layer and six units of the third layer were connected to each of the previous layer's neurons. Like in the other described cases, the single output unit was connected to all the units of previous layer.

4.2.2. Discussion of results

Figure 24 presents responses of the four described neural networks [A, B, C, D] to the learning [A1, B1, C1, D1] and testing [A2, B2, C2, D2] sets described above. The training was performed according to the convention artifact = 1, non-artifact = 0. Rectangles at abscissa 0 and 1 represent the expert's decisions - number of non-artifacts and artifacts, respectively. Ideal situation would be represented by a plot with shaded area corresponding to number of non-artifact cases concentrated at abscissa 0, with height equal to height of the left rectangle. Analogically the area dotted to indicate artifact cases would be concentrated at abscissa 1 and as high as the right rectangle. We can observe e.g. large amounts of responses close to 0.4 for network D for both the training and testing datasets. It corresponds to a class of signals, with which the network "didn't know what to do".

To convert the network's output, represented by continuous values ranging from 0 to 1, to binary decisions, we set a decision threshold. Values below this threshold are treated as 0, above - as 1. After such a quantization we have four possible ways to classify the network's response:

net \ expert	0	1
0	<i>TN</i>	<i>FP</i>
1	<i>FN</i>	<i>TP</i>

Choice of the threshold value influences the network's performance in respect to the recognition of artifacts and non-artifact epochs. The performance can be measured by means of probability of proper classification, i.e. probability that an epoch marked by expert as an artifact will be classified accordingly by the network. We can define the detectability of artifacts as $TP/(TP+FN)$ and detectability of non-artifact epochs as $TN/(TN+FN)$. Another parameter, reflecting the probability that the segment classified by the network as an artifact was indeed marked so by the expert, can be called selectivity. Network's selectivity with respect to artifacts will be given by $TP/(TP+FN)$, and with respect to non-artifact epochs - $TN/(TN+FP)$.

The table below presents performance of the four tested networks on the testing dataset for an optimal choice of the threshold parameter:

		A	B	C	D
threshold		0.4-0.9	0.1-0.2	0.1-0.9	0.1-0.3
detect-ability	artifacts $TP/(TP+FP)$	0.9	0.7	0.3-0.4	0.7
	non-artifacts $TN/(TN+FN)$	0.2-0.3	0.8	0.7-0.8	0.7
selectivity	artifacts $TP/(TP+FN)$	0.35	0.7	0.4	0.5
	non-artifacts $TN/(TN+FP)$	0.7	0.85	0.7	0.8

Networks A and C show unsatisfactory performance on the testing set, although on the training set they learned to perform well. For the networks B and D performances on the testing set were very similar to those on the learning set, which proves their good generalization properties. The next table summarizes above results:

	input preprocessing	input size	convergence (iterations)	generalization
A	(none) raw signal	6750	$18 \cdot 10^6$	poor
B	correlations, variances and averages	45	$22 \cdot 10^6$	good
C	raw wavelet coefficients	6912	$2 \cdot 10^6$	poor
D	wavelet-based band-delimited correlations and powers	46	$2.1 \cdot 10^6$	good

4.2.3. Conclusions

1. Networks with smaller and carefully chosen input show better generalization.
2. Use of raw wavelet coefficients on input increased the learning speed by an order of magnitude as compared to the raw signal. This demonstrates relevance of the morphological information carried by wavelet coefficients.
3. Orthogonal wavelet decomposition allows for efficient calculation of more sophisticated preprocessing [like e.g. band-limited correlations in place of overall correlations], keeping the computational cost of preprocessing low.

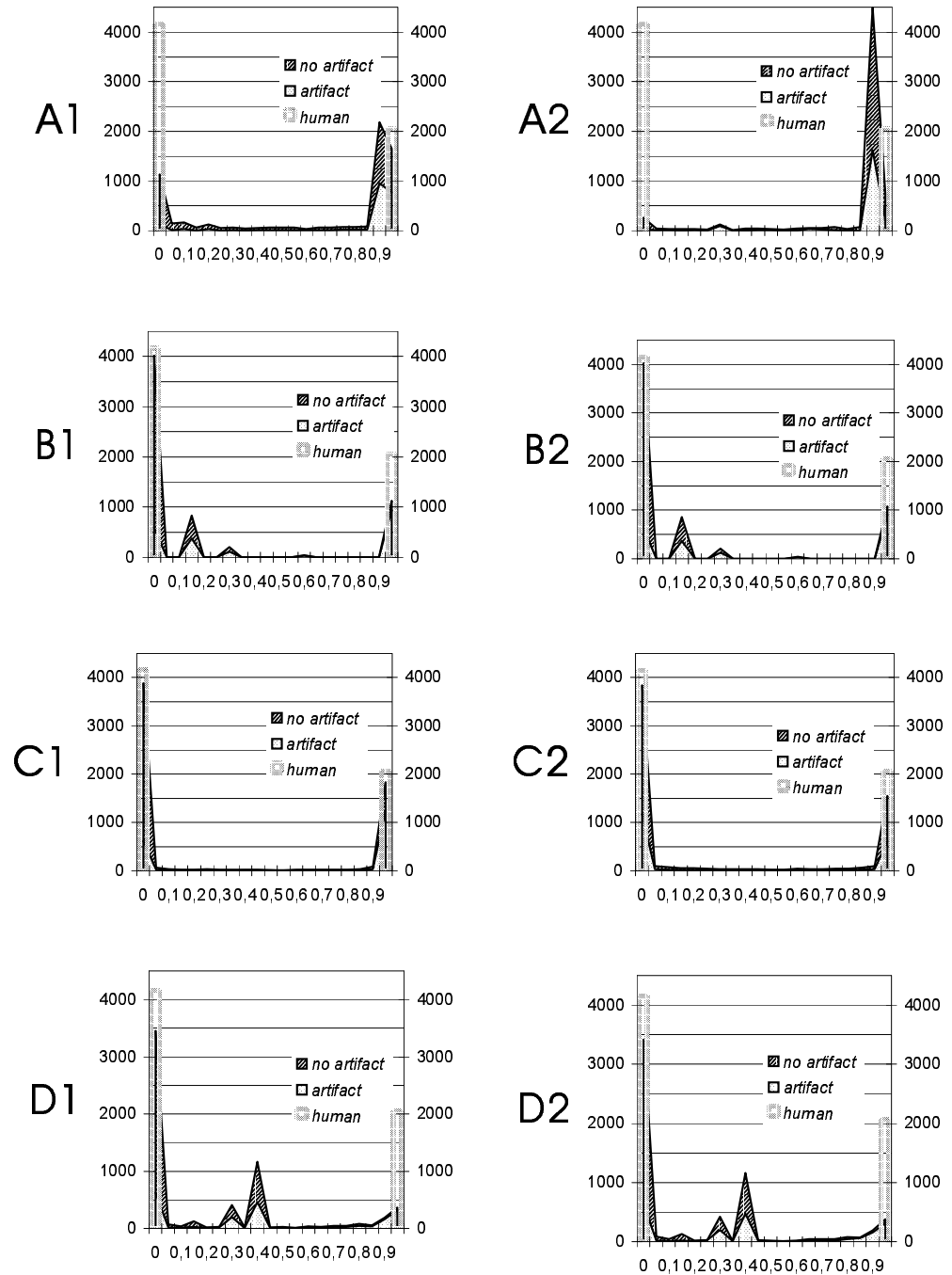


Figure 24 Number of responses of tested networks to the learning (A1, B1, C1, D1) and testing (A2, B2, C2, D2) sets. Abscissa - the value given by output neuron. Rectangles at 0 and 1 represent expert's decisions.

4.3. Sleep spindles detection and analysis based upon Matching Pursuit parametrization

Sleep spindles play a major role in the analysis of cerebral activity in sleep. Spontaneous bursts of rhythmic 12-14 Hz activity in the background EEG of subject in light sleep were first observed by Loomis et al (1935), who from the beginning designated them as "spindles". Later the terms *sigma waves* or *sigma activity* were recommended by the International Federation for Electroencephalography and Clinical Neurophysiology [IFSECN] in 1961, but the use of this terminology was eventually discouraged by IFSECN in 1974. In the "Glossary of terms commonly used by clinical electroencephalographers" [IFSECN 1974] spindles are defined as *"group of rhythmic waves characterized by progressively increasing, then gradually decreasing amplitude"*. Definition given in (Rechtschaffen and Kales 1968) states: *"The presence of sleep spindle should not be defined unless it is at least 0.5 sec. duration, i.e. one should be able to count 6 or 7 distinct waves within the half-second period. (...) The term should be used only to describe activity between 12 and 14 cps."* In (Dutertre 1977) we find also that *"spindle waves are monomorphic, dysphasic and symmetrical with respect to the baseline. Frequency is stable at 12 to 14 Hz. Duration of the whole spindle is variable from 1 to 6 s"*.

Jankel and Niedermayer (1985) discuss also the controversial issue of existence of spindles with frequency around 10 Hz. This question is not addressed in this work.

Sleep spindles show variations with regard to wave morphology, frequency, spatial distribution and stage of sleep. The appearance of spindles is modified by age and certain central nervous system disorders. Their accurate description may be of interest in study of sleep disorders, depression, aging, drug effects, torsion dystonia and assessment of benzodiazepines (Trenker and Rappelsberger 1996).

Finally, one more terminological clarification should be quoted after Jankel and Niedermayer (1985): *"The sleep spindle of the electroencephalographer [recorded in patients or healthy subjects] must be carefully distinguished from the spindles discussed by neurophysiologists. These are usually barbiturate spindles recorded in experimental animals and have served as a model for the understanding of the genesis of physiological EEG rhythms such as alpha rhythm [see (Andersen 1966)]"*. In this work we are investigating the sleep spindles, not the barbiturate spindles.

4.3.1. Experimental data

	Fp1	Fpz	Fp2	
F7	F3	Fz	F4	F8
T3	C3	Cz	C4	T4
T5	P3	Pz	P4	T6
	O1	Oz	O2	

Table I Schematic representation of electrodes positions according to the "10-20" system. Front of head towards top of page.

Overnight recordings of sleep EEG were provided by prof. Waldemar Szelenberger from Warsaw Medical School, Department of Psychiatry. Standard polysomnographic channels, 21 channels of EEG according to the 10-20 standard and A1 and A2 derivations were recorded. Silver electrodes were applied with collodion. Maximal accepted resistance was less than 5 Kohms. 12 bit analog-digital

converter was used and conversion rate was 102.4 Hz. Results described below were obtained from recordings of second nights of healthy volunteers, usually about 7 hours of EEG registered by the Medelec EEG recorder. Both the visual and numerical analyses were performed on signals referenced to the A1/A2 electrodes.

Segments of 20s [2048 points] length were subjected to MP decomposition with 100 iterations for each segment. Although in most cases the algorithm was finding coherent structures [section 2.4 page 38] also beyond this step, they were atoms of a very low amplitude which lie far beyond the verge of visual detectability. Even with this limitation the decomposition of 21 EEG channels of each of the mentioned overnight recordings took about 8 days of computations on IBM RS/6000 320H workstation.

4.3.2. Choosing spindles from time-frequency atoms

The basic shape of waveforms of the Gabor dictionary [section 3.5] corresponds well to the shape described in the definitions of sleep spindles [beginning of chapter 4.3]. Therefore each of the spindles should be represented by one time-frequency atom from this dictionary. However in (Jankel and Niedermayer 1985) we find a warning:

"It seems to be self-explanatory that the term 'spindle' implies a belly in the middle [of the spindle train] tapering off to the left and the right. This shape of spindle trains, however, is the exception rather than the rule. A train of alpha waves is more likely to show the crescendo-decrescendo of 'spindle' - shape. Thus, the term 'spindle'

is a misnomer as far as sleep spindles are concerned. It is, however, a 'catchy' and so widely used term that no terminological change should be made".

Nevertheless, as already stated, the Gabor dictionary was chosen due to the optimum time-frequency localization of Gabor functions, and its application is by no means limited to the spindle-like structures.

The main task is to choose from the waveforms fitted to the analyzed segment structures corresponding to sleep spindles. Such a procedure will operate in the space of parameters of fitted atoms: time, frequency, octave, modulus and phase [eq. (3.4) paragraph 3.5].

4.3.2.1. Relevant parameters

Frequency. Rechtschaffen and Kales (1968) defined the frequency range of spindles as lying between 12 and 14 Hz. In more recent works this range is usually widened up to 1 Hz up and down. Jankel and Niedermayer (1985) explicitly state that *"There is no doubt (...) that the 12-14c/s range is too narrow"*. In this work the frequency range for a structure to be considered a sleep spindle was set between 11 and 15 Hz.

Octave corresponds to the width in time of the waveform [eq. (3.8)]. For the particular experimental conditions [sampling frequency $f_s=102.4$ Hz, length of analyzed epoch $N=2048$ points] we obtain the following values for the half-width in time $T_{1/2}$ of an atom with the octave j [eq. (3.8)]:

octave j	5	6	7	8	9
half width $T_{1/2}$ [s]	0.29	0.59	1.17	2.35	4.7

Octaves from 6 to 8 were chosen. Numerical values of time and frequency resolutions [eq. (3.7), (4.17)] for these octaves are given in the table below:

octave j	6	7	8
time resolution ΔT [s]	0.08	0.16	0.31
frequency resolution Δf [Hz]	0.2	0.1	0.05

Time of occurrence naturally has no influence on classification, although it is an important parameter in evaluation of results.

Finally, the real challenge was presented by the problem of setting bounds on the amplitude parameter for atoms that are to be considered sleep spindles. In the definitions of sleep spindles [chapter 4.3] no assumptions about the amplitude are made, which means naturally that every "visible" structure satisfying the frequency and time span criteria is to be considered a spindle. That translates to some lower bound on the amplitude [or rather local S/N ratio], which makes the structure distinguishable from the background, and no upper bounds. In the previous attempts of automatic spindles detection [Fish et al 1988, Broughton et al 1978, Campbell et al 1980] an arbitrary threshold, usually from 5 to 25 μV , was being set in order to reduce detections due to the background noise.

The notion of "visibility" in terms of the MP method means that the structure was detected - i.e. the proper waveforms were fitted in the iterative procedure before applied criterion stopped the algorithm [section 3.5]. The amplitude was left as a free parameter for investigating the agreement of visual and automatic detection. Problem of lower amplitude of spindles will be further discussed in paragraph 4.3.4.5.

Amplitude corresponds to the **modulus** parameter describing dictionary's atoms. Relation between modulus and amplitude of window function of an atom from the Gabor dictionary - eq. (3.4) - is given by eq. (3.5). However, this formula gives the amplitude of the **window function**. The actual peak-to-peak amplitude of corresponding Gabor function can be lower depending on its frequency and phase parameters, as discussed in par. 3.5.

Formula (3.5) can be simplified for atoms that are to be considered sleep spindles. They have octave from 6 to 8 and frequency from 11 to 15 Hz, which corresponds to $k=220\div300$. In such case

$$e^{-\frac{2\pi 2^{2j} k^2}{N^2}} \ll 1 \quad (5.1)$$

which yields an approximate formula for the amplitude of window function

$$K_{(\gamma, \phi)} = \frac{2^{\frac{1}{4}}}{\sqrt{2^j \left[1 + e^{-\frac{2\pi 2^{2j} k^2}{N^2}} \cos\left(\frac{4\pi k p}{N} + 2\phi\right) \right]}} \approx 2^{\frac{-2j+3}{4}} \quad (5.2)$$

Calibration of recording devices [including A/D converter] gives us the number that represents 1 μV - let's call it U_0 . Approximate amplitude [in μV] of the window function of a structure represented by an atom from the Gabor dictionary is given by

$$U(j, \text{modulus}) = 2 * \text{modulus} * \frac{2^{\frac{-2j+3}{4}}}{U_0} \text{ } [\mu\text{V}] \quad (5.3)$$

However, the notion of sleep spindle amplitude originated from the visual analysis, where the actual difference between the observed maximum and minimum was measured rather than the envelope's amplitude. Moreover, in our case visual analysis was performed on the digitized data, as seen on a computer display. Due to these conditions, a correction factor for calculating the actual peak-to-peak amplitude instead of the amplitude of the window function [compare Figure 17 and Figure 16] was added to formula (5.3) for calculations of structure's amplitudes.

4.3.2.2. Comparison of automatic detection to human judgment

According to the criterion of verifiability from section 1.1 we should check the consistence of the automatic detection of sleep spindles with results of visual analysis. For this purpose sleep spindles in one derivation (C3-A2) of the overnight recording were marked by an experienced electroencephalographer. An option of marking beginnings and ends of structures was added to the program used routinely for visual evaluation of digital EEG recordings.

The possible differences and concordances were counted as follows:

- TP (true positive): position in time of a chosen atom lies within the borders of a spindle marked by electroencephalographer,
- FN (false negative): there's no atom chosen within the borders of a spindle marked by electroencephalographer,
- FP (false positive): the chosen atom lies outside borders of any of the marked spindles.

The only free parameter left to investigate the behavior of the TP/FP curves is the value of minimum amplitude, from which an atom conforming to frequency and time span criteria [section 4.3.2] is to be considered a sleep spindle. This value will be called below a threshold amplitude.

Figure 25 presents results of comparison of automatic spindle's detection to human judgment. Figure 25 a) shows relative percentage of true positive detections to all the detections - $TP/(TP+FP)$, plotted versus the threshold amplitude. Figure 25 b)

corresponds to numerical derivative of the above curve, presenting the same $TP/(TP+FP)$ counted within ranges of threshold amplitude. Namely in Figure 25 *b*) a bin at abscissa x relates to amplitude between x and $x+5$ microvolts, while in Figure 25 *a*) we count all the events corresponding to amplitude from 0 to x . We can observe, on both the plots, that for the threshold value about 50 microvolts [peak-to-peak], true positive detections as related to all the detections exceed 50%.

Figure 25 *c*) and *d*) present histograms of distribution of the TP and FP detections versus the threshold amplitudes. Histogram bins are 5 microvolts wide. The TP cases are distributed rather uniformly across the amplitudes, decreasing only at the high amplitude values, because very high amplitude spindles occur rather seldom. FP cases reach maximum at low threshold amplitudes. It relates to poor visual detectability of low amplitude spindles. Spindles of amplitude which doesn't significantly exceed the amplitude of the background are buried in on-going EEG. Therefore low amplitude spindles are often elusive to visual analysis. Their accurate detection by the algorithm results in FP cases.

Closer inspection of separate FN events revealed that spindles marked by the expert and non detected by the algorithm have either frequency or time span beyond the defined limits. Therefore the FN cases were usually result of inaccurate detection of spindles by human judgment. Mentioned "inaccuracy" relates to the time-frequency characteristics of sleep spindles, defined arbitrary in terms of fixed ranges of parameters, as described in section 4.3.2. This way of defining EEG structures will be further discussed in section 4.3.5.

Figure 32 presents example of another type of inconsistencies between automatic and human detection: superimposed spindles. Structures C and D were classified as one spindle. The time position of the center of structure F falls 7 milliseconds outside the section marked by expert as a spindle. Therefore structure F contributed to the FP cases. The issue of superimposed spindles will be further discussed in par. 4.3.4.2. Figure 33 presents the same time-frequency map in three dimensions, with vertical coordinate corresponding to the energy density.

Above results show reasonable concordance with visual analysis for higher values of amplitude. Higher sensitivity of the automatic choice for weaker structures was observed. Further investigation in this field requires a larger project, including e.g. comparison between scores of several electroencephalographers.

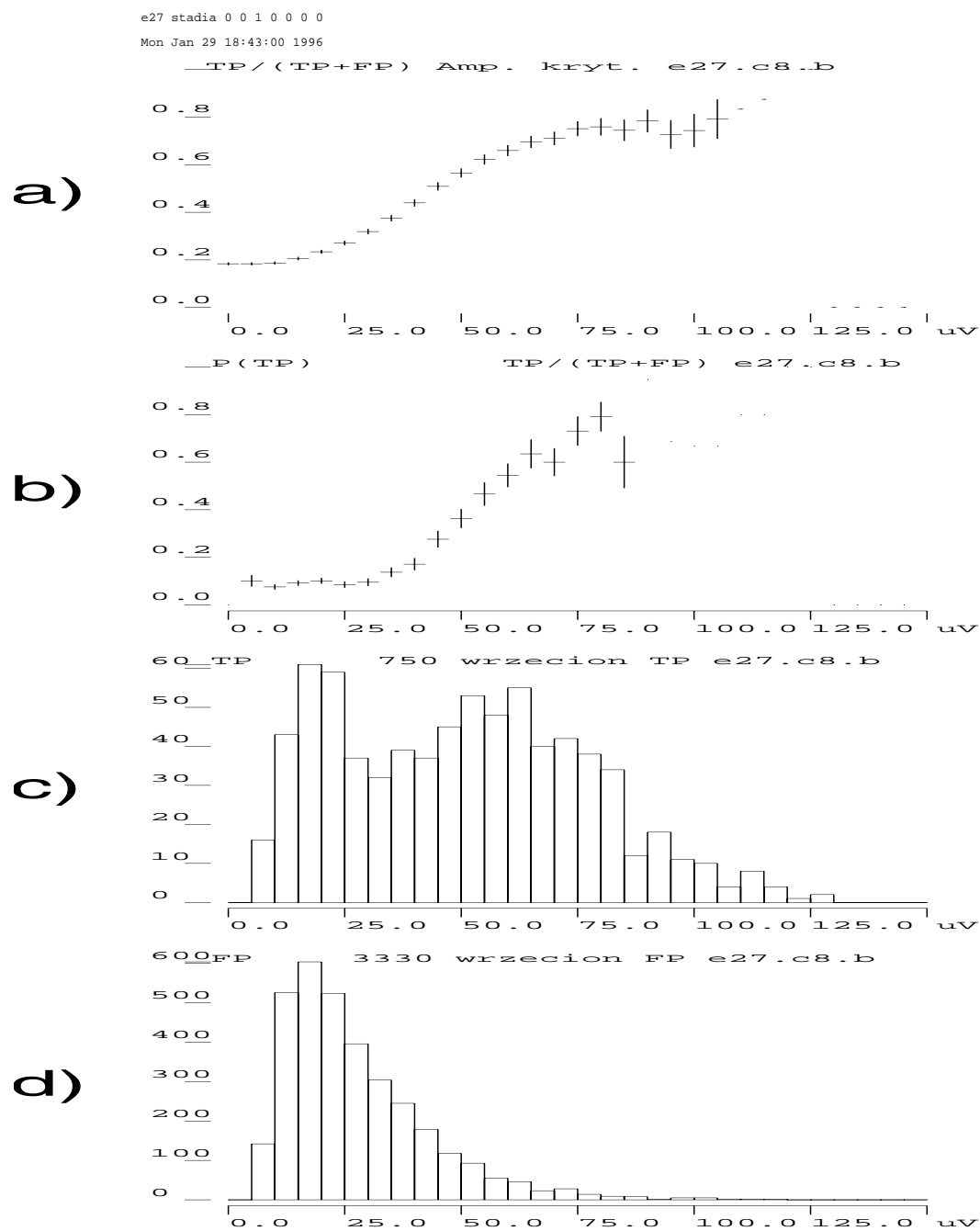


Figure 25 Automatic vs. visual detection of spindles: a) $TP/(TP+FP)$ vs. threshold amplitude, b) within ranges of amplitude, c) and d) - histograms of TP and FP detections vs. amplitude

4.3.3. Other methods of automatic detection of sleep spindles

Visual recognition of spindles in overnight EEG recording is an laborious and often unreliable task. It's enough to imagine a paper recording of one night EEG, about 0.5 km long. Therefore several methods for automatic detection of sleep spindles were developed.

Campbell et al (1980) tested the performance of two phase-locked loop spindle detector systems devised by Broughton et al (1978) and Kumar (1975). They report 65 to 72% of true positive detections by the systems, as compared to visual scoring, and 86% concordance between two independent human experts.

Declerck et al (1986) report better performance of software over hardware methods - agreement of more than 90% with the visual analysis. One important conclusion can be quoted from their paper: *"An exact specification of the criteria used to describe sleep spindles is extremely necessary to be able to compare the results of the different sleep spindle detection methods applied in many laboratories."*

Fish et al (1988) modified the "spindicator" hardware device proposed by Pivik (1982). The threshold for spindle's amplitude was set at 14 μV which gave false detections below 2%. Resulting concordance with visual analysis reached 96%. By means of this device the durations and amplitudes of spindles were measured with high correlations to visual measures on paper recordings.

Jobert et al (1992) used matched filtering for automatic detection of sleep spindles in frequency bands. Applied templates resulted in 1 Hz frequency resolution. Reported comparison with visual detection yielded 80.1% of true positive and 15.9% of false positive. However, thresholds for the detection were adjusted to optimize the concordance with human choice. Therefore the method was partially based upon the visual analysis and explicitly tuned for maximum concordance with it. Results obtained by Jobert et al (1992) confirmed the hypothesis quoted in Jankel and Niedermayer (1985), regarding two types of sleep spindles: slow spindles with frequency about 12 Hz more pronounced in the frontal region and fast spindles around 14 Hz preferably localized in the parietal region.

Finally Schimicek et al (1994) simply filtered EEG in spindles frequency band [11.5-16 Hz] and to the resulting signal applied an amplitude [$>25 \mu\text{V}$] and structure's time width [$>0.5 \text{ s}$] thresholds. By automatic removal of detections presumably connected with alpha or muscle activity, they achieved average of 90% true positive detections on EEG of 10 subjects, as compared to visual analysis.

All these methods were tailored especially for the task of spindle's analysis, with the main goal to imitate the human detection. And that is exactly where the limitations of these methods originate. Let's consider for example a procedure of setting the minimum signal-to-noise ratio for a structure to be detected as spindle. This parameter, set e.g. as 2.5 in (Dijk et al 1993), was intended to minimize the detections due to the background noise. However, the background activity, which changes the S/N ratio, has no documented relation to the spindles occurrence. Therefore such parameter should not be taken into account in the procedure of detection.

Quoted methods fulfill only the criterion of verifiability from section 1.1. On the contrary, procedure proposed in this work implements "raw" criteria on spindle's frequency and duration. Method proposed in this work was aimed at detection of all the phenomena bearing time-frequency signatures within defined ranges, regardless of their "visibility" dependent on background activity. This must be taken into account when comparing the performance of this detection, measured in terms of agreement with visual analysis, with methods aimed directly at the maximization of this index.

4.3.4. Investigation of sleep spindles properties and distributions

Note: Figures 25-36 and Table II presented in this chapter relate to one of 10 analyzed subjects [e27]. It was the first fully analyzed overnight recording and the only one for which the comparison with human detection of sleep spindles was performed. Similar plots for other analyzed subjects are not included in order to preserve reasonable volume and consistency of presented figures. This subject's recording contained also the highest amplitude spindles, so the plots show the trends present in all the recordings in a 'clearer' way. However, discussed results and conclusions apply to all the 10 analyzed overnight recordings.

After completing the procedure of choice described in par. 4.3.2 we are confronted with a huge amount of numeric data. There are usually at least several hundreds of spindles detected in each electrode's recording, each of them described by five parameters [time, frequency, amplitude, octave, phase]. Proper presentation of this data is crucial for the final step of analysis.

Traditionally the process of sleep is perceived in a form of 'sleep staircase' or hypnogram, presented in Figure 26 c) [courtesy of prof. W. Szelenberger from Warsaw Medical School]. Therefore temporal distributions are closely related to the traditional approach. Figure 26 b) presents temporal distribution of amplitudes of detected spindles, i.e. in the time coordinate of each of detected spindles a vertical line with height proportional to the spindles's amplitude is positioned. In Figure 26 a) frequencies of detected spindles are marked in corresponding time coordinates. Finally in Figure 26 d) presents the number of spindles detected per minute.

For evaluation of certain trends, like e.g. frequency distributions, other reports will be convenient. Figure 26 f) presents histogram of frequencies of detected spindles, while e) marks each of detected spindles in the frequency-amplitude coordinates, providing information corresponding to f) and at the same time keeping track of the amplitude values. Similar plots are presented on Figure 27: a - hypnogram, b - frequencies and c - amplitudes of detected spindles marked in time and d - spindle's density. They correspond exactly to plots c-a-b-d from Figure 26. Plots f-g, i.e. frequencies and amplitudes marked in time, correspond to b-c from this figure, presenting instead of spindles structures detected as slow wave activity (SWA). Criteria for the SWA structures were set as: frequency from 0.5 to 4 Hz, amplitude above 75 μ V, time span above 2.35 s. The plot in e) marks for each minute a magnitude

corresponding to the spectral power in the chosen above SWA frequency band. However, this magnitude is calculated only from the moduli of selected atoms. Advantage of such a way of calculating spectral power lies in possibility of explicit including or excluding structures, according to other than only frequency-based criteria. It is also convenient that calculation of this parameter were accomplished in the framework of the same formalism as description of transients presented above.

The above reports present characteristics of structures detected for one particular electrode. For evaluation of the spatial relationship we can combine the same kind of reports for several electrodes. In such case it is convenient to conserve the position of plots on page corresponding to the position of electrodes on the scalp, like e.g. in Figure 28.

In some cases a more "microscopic" insight into a single spindle's realization across electrodes may be required. Figure 29 shows the presence of two sleep spindles in all the recorded EEG channels. Spindles are marked in boxes corresponding to electrodes. Each box contains [from the top] frequency [Hz], amplitude [μ V], relative position in time [bottom left, ms] and time span [bottom right, ms] for a spindle possibly detected in related position. Boxes are positioned topographically, relating to the position of electrodes on the scalp. Front of head towards top of page. Shading of each box is proportional to amplitude. The time resolution of the method for the particular experimental settings [sections 3.5, 4.3.2.1] gives a possibility to investigate the casual relationships between spindles in different electrodes. This microscopic tool can provide a deep insight into the mechanism of spindle's generation. However, for one overnight EEG recording we could draw several hundreds of such maps. Therefore for the beginning we turn our attention to reports summing up more information per page.

Based upon presented above reports, in the following paragraphs we discuss several properties and distributions of sleep spindles and SWA.

4.3.4.1. Hypothesis of two generators

In (Jankel and Niedermayer 1985) the existence of two distinct types of spindles was suggested. They were the slow spindles of frequency about 12 Hz, more pronounced in the frontal region, and fast spindles of frequency about 14 Hz localized mainly in the parietal region. These assumptions suggest a hypothesis of two distinct generators located in the frontal and parietal brain regions (Jobert et al 1992).

Two types of reports can provide a one-sight verification of presence of such a trend. Figure 30 presents histograms of detected spindle's frequencies for all the

21 electrodes. Positions of plots corresponds to the positions of electrodes on the scalp. Frontal electrodes are represented in the upper part of the picture. Figure 31 is organized in the same way. However in this case, for each electrode, position of each detected spindle is marked in the frequency-amplitude plane, providing additional information about the frequency distribution of amplitudes. Both reports clearly present the trend locating higher frequency spindles in anterior electrodes and lower frequency - in posterior. Such a trend was generally present on plots drawn for each of 10 analyzed subjects.

Table 1 gives total amount of detected spindles, their average frequency and standard deviation of average together with numbers of superimposed spindles [see next paragraph] for one overnight recording. It presents results from the same EEG recording of the second night of healthy volunteer as Figures 25-36. Parameters of structures treated as sleep spindles were set as in chapter 4.3.2, i.e frequency between 11 and 15 Hz, amplitude higher than 25 microvolts and time span from 0.59 to 2.35 s.

4.3.4.2. Superimposed spindles

In some cases a structure marked by expert as one sleep spindle can have frequency signature varying with time. Hao et al (1992) proposed interpretation of such cases as superposition of two different spindles. They applied complex demodulation to the structures marked especially for this purpose by an electroencephalographer.

Figure 32 [and Figure 33] presents an example of a case where within the section marked by expert as spindle we have two MP atoms conforming the spindle's criteria. Structures C and D were classified as one spindle. Similarly structures E and F, fulfilling spindle's criteria, are very close in time. However, the time position of the center of structure F falls 7 ms outside the section marked by expert as a spindle. Therefore structure F contributed to the *FP* cases. Results of MP decomposition of these structures can be interpreted in two possible ways: either we deal with different phenomena appearing closely in time, or the frequency changes within the structure's duration. The structure of changing frequency would be represented as few separate atoms, because in the applied dictionary there are only structures of constant frequency. Additional information can be provided by tracing the spatial distribution of these structures. Figure 29 presents distribution of energy of spindles *E* and *F* across the electrodes. Each box corresponds to one recorded channel and contains [from the top] frequency [Hz], amplitude [μ V], relative position in time [bottom left, ms] and time span [bottom right, ms] for a spindle possibly

Derivation	Number of detected spindles	Average weighted frequency [Hz]	Standard deviation of average frequency [Hz]	Number of superimposed spindles	% super-imposed
Fp1	1853	11.85	.73	77	4.16 %
Fpz	1908	11.87	.73	97	5.08 %
Fp2	1863	11.92	.75	95	5.10 %
F7	959	11.83	.67	18	1.88 %
F3	3087	12.16	.89	257	8.33 %
Fz	3359	12.24	.91	339	10.09 %
F4	3264	12.3	.90	337	10.32 %
F8	1361	11.94	.71	31	2.28 %
T3	489	12.04	.77	4	0.82 %
C3	2676	12.54	.95	163	6.09 %
Cz	3464	12.57	.96	269	7.77 %
C4	2864	12.6	.92	169	5.90 %
T4	466	12.07	.75	4	0.86 %
T5	581	12.83	.65	4	0.69 %
P3	2850	13.04	.77	130	4.56 %
Pz	3311	13.09	.73	188	5.68 %
P4	2755	13.05	.75	117	4.25 %
T6	421	12.86	.58	3	0.71 %
O1	767	13.09	.45	1	0.13 %
Oz	1166	13.1	.47	6	0.51 %
O2	935	13.09	.46	2	0.21 %

Table II Summary of spindles detection in one overnight recording for 21 EEG channels. Average frequency weighted by amplitudes.

detected in related position. Boxes are positioned topographically, relating to the position of electrodes on the scalp. Front of head towards top of page. Shading of each box is proportional to amplitude. We notice that higher-frequency spindle *E* is stronger in occipital electrodes, while amplitudes of lower-frequency spindle *F* are higher in frontal electrodes, although in some of them this spindle is missing. These distributions suggest that we deal with two different phenomena rather than one structure of changing frequency.

In the presented framework the separation of superimposed structures with varying time-frequency signatures is straightforward. They can be automatically

detected for the purpose of further investigations, based e.g. upon the proximity in time below 0.5 s., as presented in Table I. In the work of Hao et al (1992) each case of the superimposed spindles was identified visually, which limits the accuracy of the procedure and possibilities to process larger amount of data.

4.3.4.3. Absence of spindles as hallmark of REM sleep

There are no sleep spindles in periods of REM sleep. This fact is generally recognized and serves as one of criteria in sleep staging. If we set the threshold for spindles amplitude at 25 μ V, as in Figure 30, we observe general consistence of the results of automatic detection with the above statement. However, we can concentrate upon sleep spindles appearing *only* in REM. Spindles appearing in stages marked as REM are plotted in Figure 34. Their number doesn't exceed 1% of all the spindles detected in given channel and they are present in the neighborhood of borders of REM stages. It is very likely that this inconsistency is a result of imperfect sleep staging based upon the visual analysis. Another reason is that sleep stages were marked for 20-s epochs. Recently it is generally acknowledged that sleep is a continuous process and the transitions between stages do not have to be sharp. This kind of reports can serve as a basis to reconsider the staging. The above discussion regards spindles defined as structures of amplitude above 25 μ V. Paragraph 4.3.4.5 goes back to the issue of cutoff amplitude and low amplitude spindles.

4.3.4.4. A step towards complete description of sleep EEG

After all the reports summarizing overall properties of sleep spindles detected in all the 21 electrodes, now we concentrate on their time occurrence in one channel. This approach is much closer to the classical way of looking at sleep, perceived in form of the 'sleep staircase' or hypnogram [Figure 27 a].

In order to provide a more complete picture, we draw also the time course of the slow wave activity (SWA). Description of the SWA was traditionally assessed by a spectral analysis. In the framework of MP we pick up from the decomposition [already performed for the purpose of spindle's parametrization] atoms conforming the criteria: frequency 0.5-4 Hz, amplitude > 75 μ V and time span >2.35 s.

The typical time course of spindle activity during normal sleep is discussed e.g. in (Dijk et al 1993) (Aeschbach 1994) and summarized in (Dijk 1995). Aeschbach et al (1994) write:

"The pattern of their [spindles] occurrence during sleep corresponds to a large extent to the pattern of spectral SFA [spindles frequency activity, spectral power density

in the spindle's frequency range] (*Dijk et al. 1993*). Both SWA and SFA rise in the beginning of a NREMS episode and decline prior to the transitions to REMS (*Aeschbach and Borbély 1993*). This positive correlation between the two activities reverses to a negative correlation in the middle part of the NREMS episode where SWA exhibits a peak and SFA a trough. This gives rise to a U-shaped time course of SFA that is most prominent in the early NREMS episodes. An inverse relationship between SWA and SFA had been recognized previously [...]"

Figure 27 presents the time course of spindles [b-d] and SWA [e-g] together with hypnogram a) in the same time scale. Data from the whole overnight recording is presented for the Pz electrode. Plots b)-c) show time distribution of frequencies and amplitudes of spindles, d) gives a number of spindles detected per minute. Plots f) and g) give frequencies and amplitudes of SWA structures, while e) presents a magnitude corresponding to the spectral power of structures classified as SWA, calculated in each minute. The time course of the spindle's density is quite similar to the time course of amplitudes of detected spindles. That means that in epochs where more spindles are detected, usually also higher-amplitude spindles are present. Time course of spindle activity and SWA in slow-wave sleep episodes [marked by presence of SWA and as stages 3-4 on hypnogram] confirms observations quoted above from Aeschbach et al (1994).

4.3.4.5. Low amplitude spindles?

Our current knowledge of sleep spindles is based upon the visual analysis of raw EEG recordings - we must admit this in the middle of the computer era. Although there are several automatic methods for detection and description of sleep spindles [see chapter 4.3.3], all of them were tuned to reproduce results of visual analysis. Thresholds of spindle's amplitude set for these automatic detectors give us an idea of the 'visibility threshold' of spindle's amplitude. It was set from 25 μV (*Shimicek et al 1994*) through 20 μV (*Campbell et al 1980*) to 14 μV (*Fish et al. 1988*). This indicates that spindles of amplitude below about 20 μV are phenomena generally unknown to science, as a natural consequence of limitations of visual detection and automatic methods tuned for its reproduction.

Approach presented in this work is free of the above limitations. Local adaptivity of the MP algorithm allows detection of weak structures with an unfavorable S/N ratio. If we define sleep spindles based upon their frequency-temporal characteristics only, we get a large amount of "low amplitude spindles" detected. At this point new questions are arising, because their pattern of occurrence doesn't

follow schemes known for the "normal" spindles. And of course we cannot rely on the comparison of these results with human detection. Nevertheless, certain observations can be drawn from presented reports.

One of the generally recognized features of sleep spindles is their absence in REM stages of sleep. The "low amplitude spindles" are present all through the overnight EEG. However, distribution of their amplitudes reveals systematic differences between REM and non-REM stages. Figure 35 presents density (1/min) of structures, conforming spindle's criteria for frequency and time span, plotted versus amplitude. Solid line relates to structures detected in non-REM sleep stages, dotted - in REM. Disappearance of structures below about 5 μV is caused by the fact that only 100 waveforms were taken into account [see par. 4.3.1]. We notice certain regularities represented also in the lower amplitude ranges. The peak of spindles density in non-REM stages [solid line] is shifted towards lower amplitudes for temporal and occipital derivations [F7, F8, T3, T4, T5, T6 and O1, Oz, O2] comparing to the remaining central and frontal channels. Spindles detected in REM [dotted line] stages are generally concentrated in lowest amplitudes. Moreover, in this lowest amplitude range [5-10 μV] the density of 'spindles' detected in REM is significantly higher than those from non-REM stages. This could be caused by false detections related to the alpha activity, but the frequency distribution of "low amplitude spindles" does not reveal any shift towards lower frequencies. This subject requires further research.

Nevertheless, it seems that at least some of the low amplitude spindles are indeed related to the 'classical' spindles. Figure 29 presents two maps of spindle's parameters across the recorded channels. Both spindles in some channels reach quite high amplitudes [97 and 61 μV]. However, in some other channels we notice structures related in terms of time and frequency parameters, of amplitudes even as low as 6 μV . This suggests that some of the low amplitude spindles can be traces of structures more pronounced in other locations. This possibly explains some of the low-amplitude spindles from non-REM periods. The low-amplitude "spindles" from the REM periods, present thorough the whole spindle's frequency band, still wait for the interpretation. The question whether all the discussed structures of amplitudes between 5 and 25 μV are indeed related to sleep spindles is of course open. To my best knowledge no research on the low amplitude spindles was published up to now.

The above discussion was intended to present new path of research opened by the application of proposed method. The current stage is too early for conclusions or even hypotheses.

4.3.5. Remarks on definitions of EEG structures

The main goal of EEG analysis is usually a comparison of results for different subjects. This situation favors the way of defining relevant phenomena in terms of fixed ranges of parameters. For example, definitions of sleep spindles quoted at the beginning of this chapter can be expressed as frequency from 11 to 15 Hz, time width from 0.5 to 2 s. However, such a standardizing approach naturally cannot take into account the basic difficulty - so basic that we can call it a feature - of all the medical sciences, namely the inter-subject variability. An example of such an approach is presented by the fixed frequency borders of EEG rhythms (*alpha*, *beta*, etc.). If we want to compare e.g. the relative spectral powers in these bands, we need of course common ranges for integration. However, the natural frequencies of EEG rhythms are different for each subject. An example of a way to overcome this difficulty was presented in my M. Sc. thesis (Durka 1990):

In the framework of the autoregressive approach the EEG was modeled as superposition of damped oscillators (Blinowska and Franaszczuk 1989). The oscillators were described in terms of their natural parameters: frequency, amplitude and damping (FAD). After choosing the proper order of the AR model for the underlying procedure, it was possible to gather the oscillators into groups corresponding to EEG rhythms by means of cluster analysis. This division, however, was absolutely free from assumption of fixed frequency borders between the EEG rhythms, yet showed similar and reasonable results for different subjects. Evaluation of pharmaco-EEG based upon this approach showed performance similar to the spectral analysis in fixed frequency bands. We encounter similar problems when analyzing the definitions of sleep spindles quoted in chapter 4.3.2. Are the fixed frequency borders justified? What is the inter-subject variability of spindles frequencies? Can we detect sleep spindles by a method based upon their more general features?

These questions may be answered in a close future based upon the framework presented here. As an example, Figure 36 presents frequency histograms of structures that would have been detected as spindles, if we extend the frequency window to 6÷17 Hz. The histograms are typical for all the 10 evaluated subjects and we can observe a natural disappearance of structures for higher frequencies. However, in the lower frequencies we observe a continuous transition from spindles to lower-frequency structures - the alpha rhythm. Therefore clustering of spindles in space of MP parameters will require taking into account other parameters besides frequency, that will allow to distinguish spindles from alpha activity.

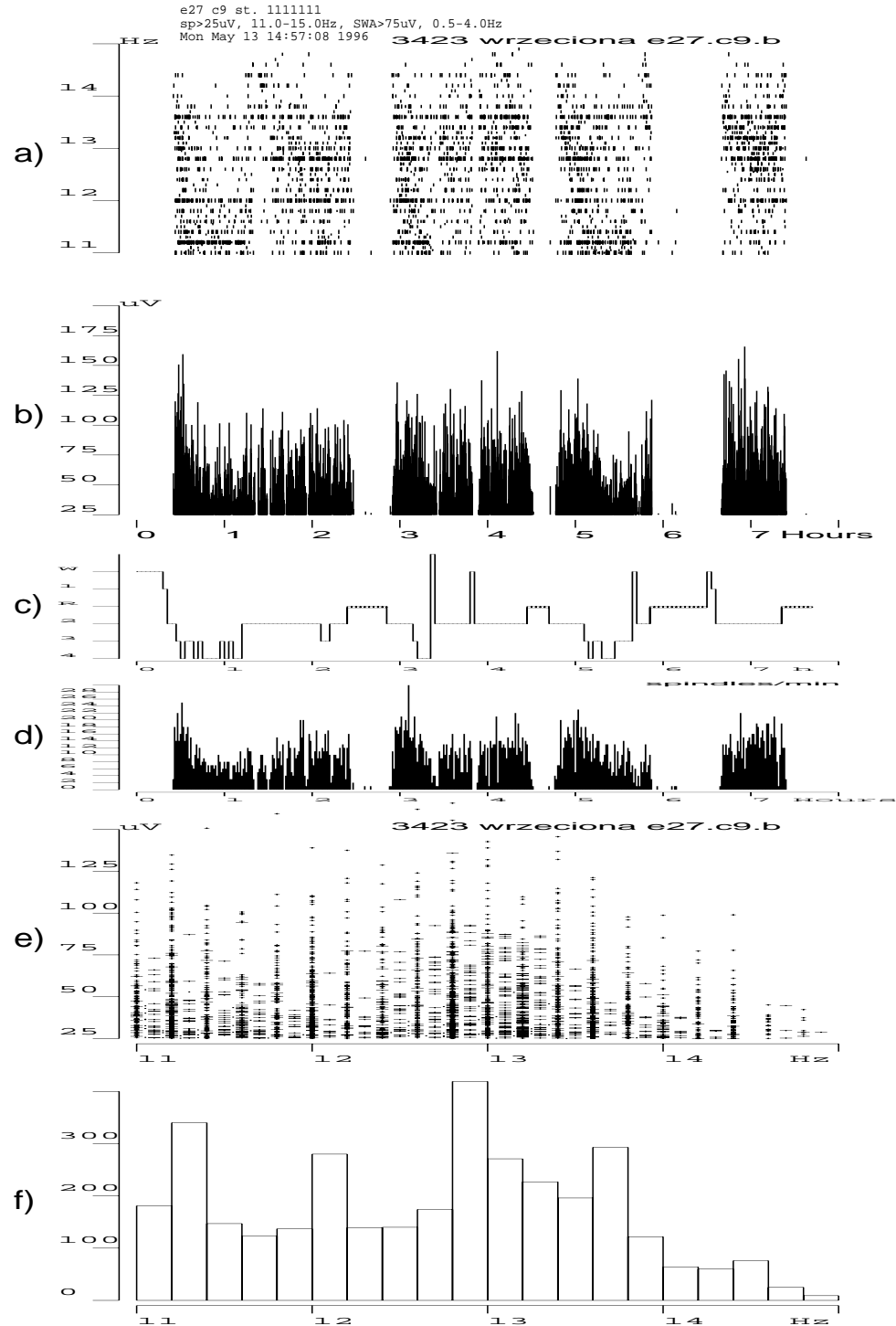


Figure 26 Spindles in Cz: a frequencies, b amplitudes, c hypnogram [court. prof. W.Szelenberger], d occurrences per minute, e amplitudes vs. frequency, f histogram of frequencies.

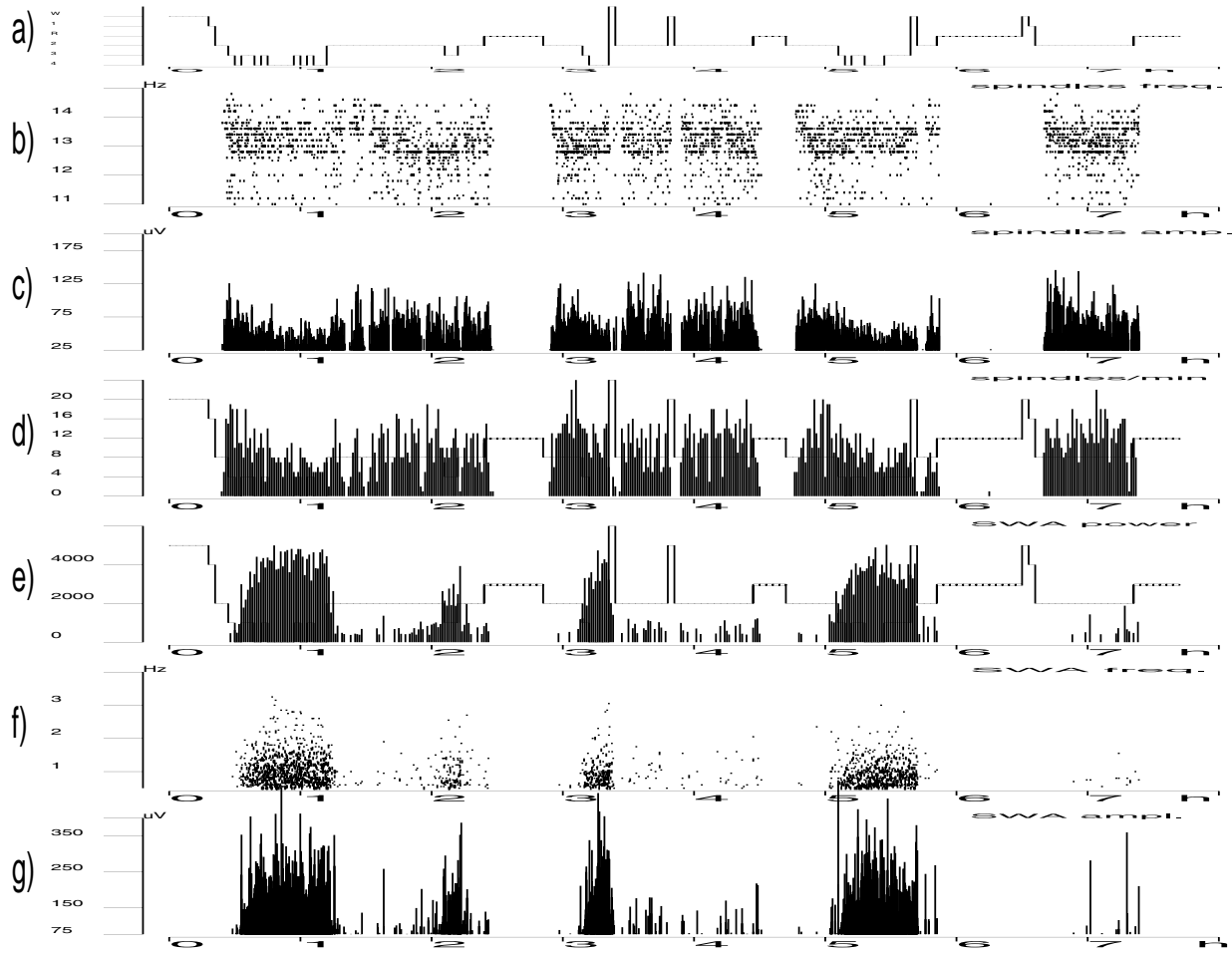


Figure 27 a) hypnogram, b) frequencies of detected spindles, c) amplitudes of detected spindles, d) spindles density [1/min.], e) SWA power, f) frequencies of SWA structures, g) amplitudes of SWA structures. Time scale conserved.

e27 stadia 1 1 1 1 1 1
 min. ampl. 25.0 microV
 Mon Jan 29 15:27:43 1996
 artefakty pomi jane

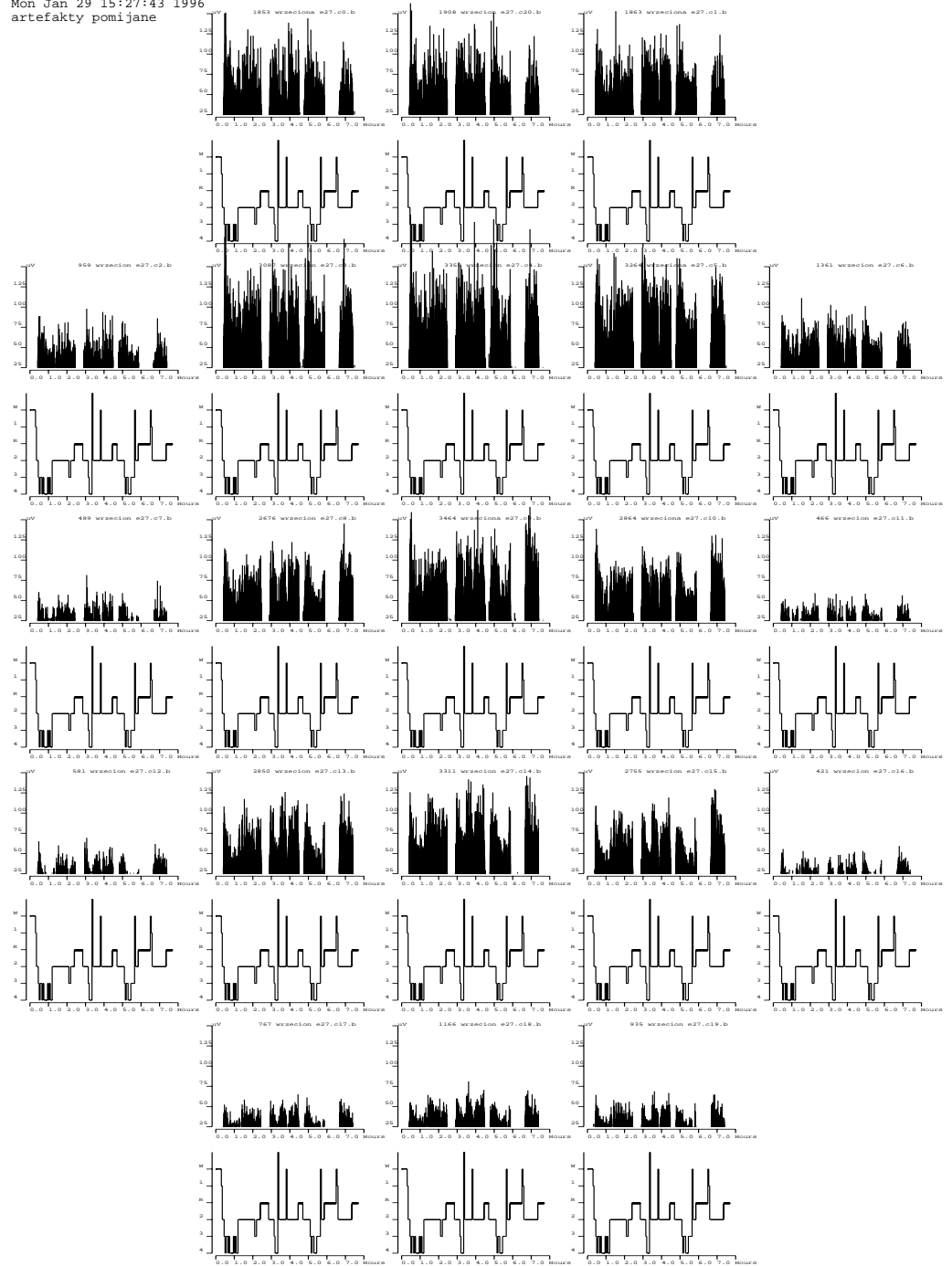


Figure 28 Plots b) [spindle's amplitude vs. time] and c) [hypnogram] from Figure 26 presented for all the 21 EEG channels. Frontal electrodes in the upper part of picture.

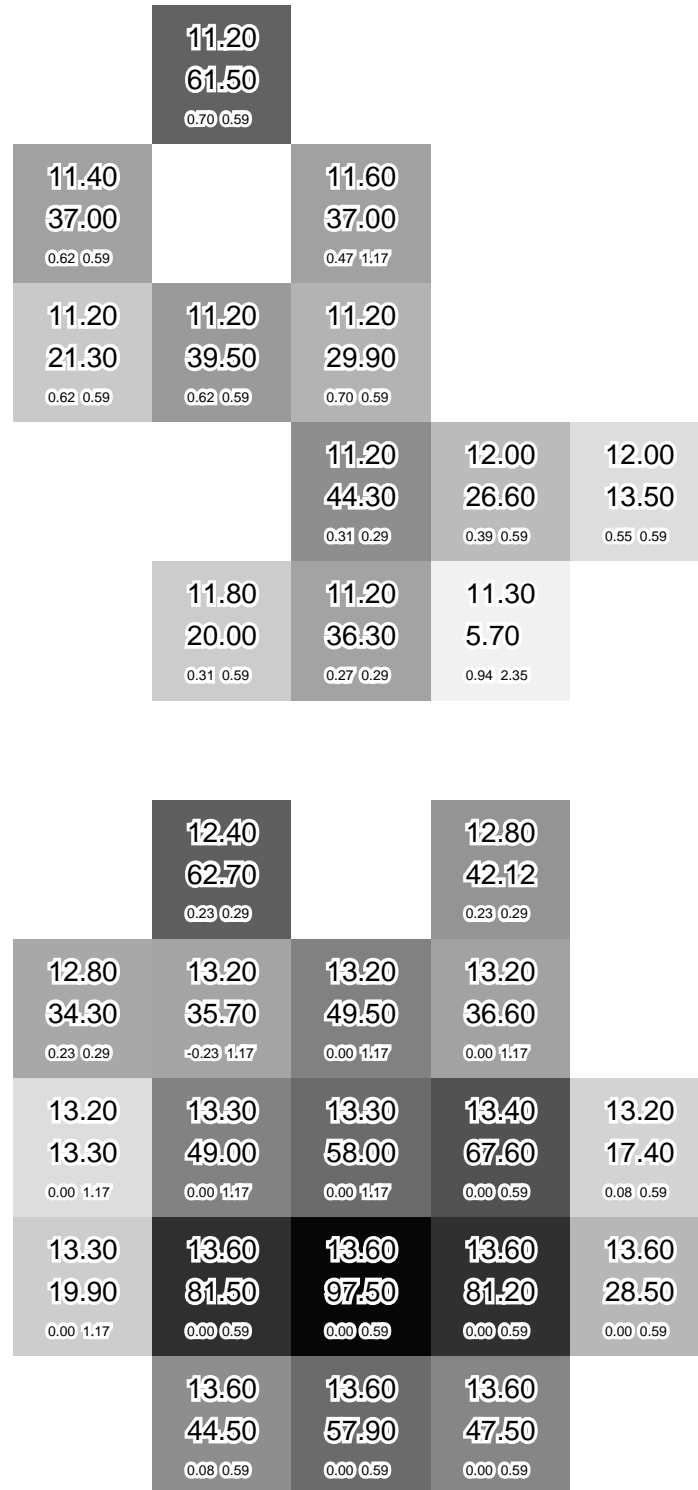


Figure 29 Spindles E and F from Figure 32 across channels. In each box: frequency [Hz], amplitude [μ V], relative position in time [s], phase. Shades of gray proportional to amplitude. Front of head towards top of page.

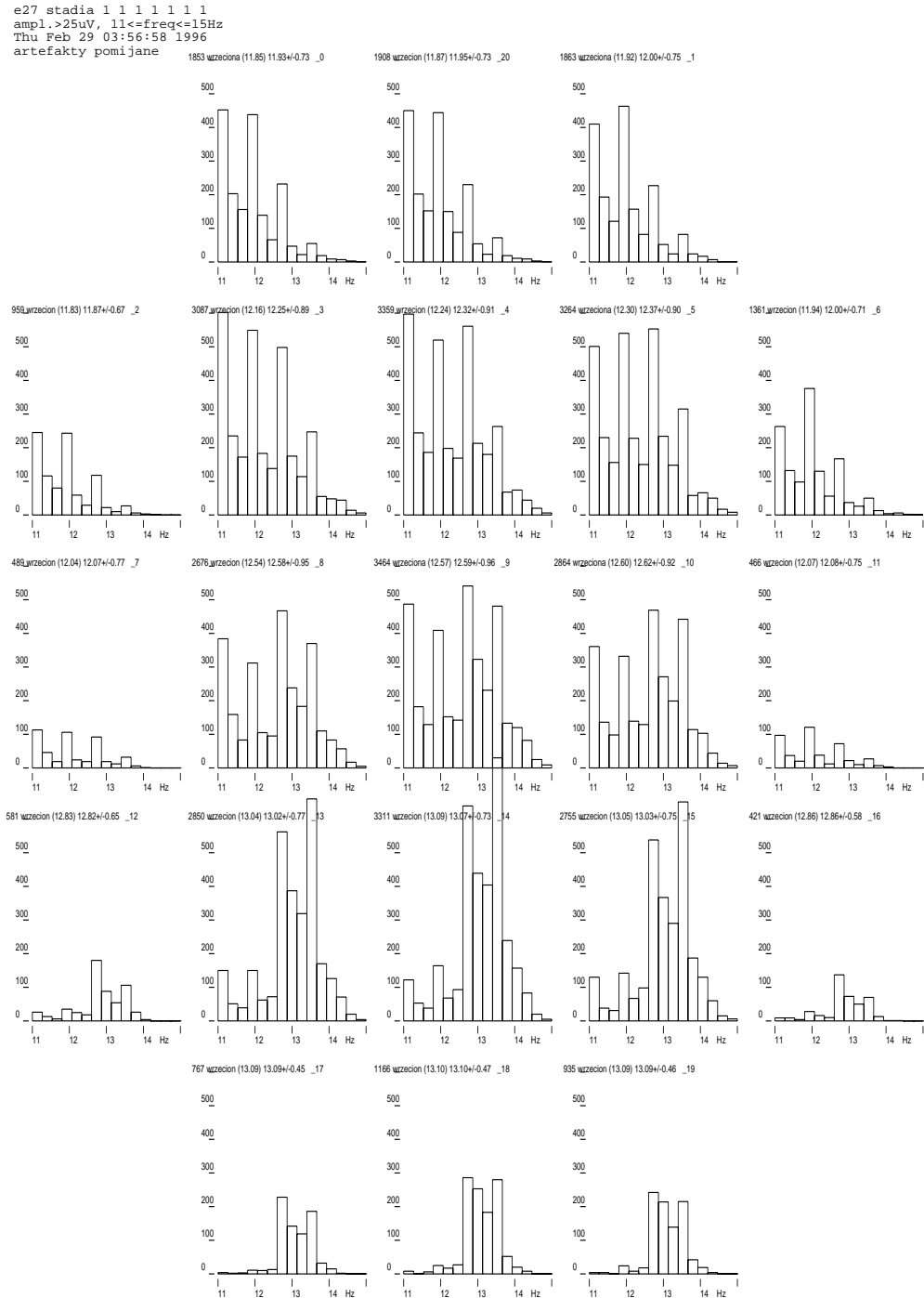


Figure 30 Histogram of spindle's frequencies [Plot d) from Figure 26] presented for all the 21 EEG channels. Frontal electrodes in the upper part of picture.

```
e27 stadia 1 1 1 1 1 1 1
ampl.>25uV, ll<=freq<=15Hz
Tue Mar 5 18:42:27 1996
artefakty pomijane
```

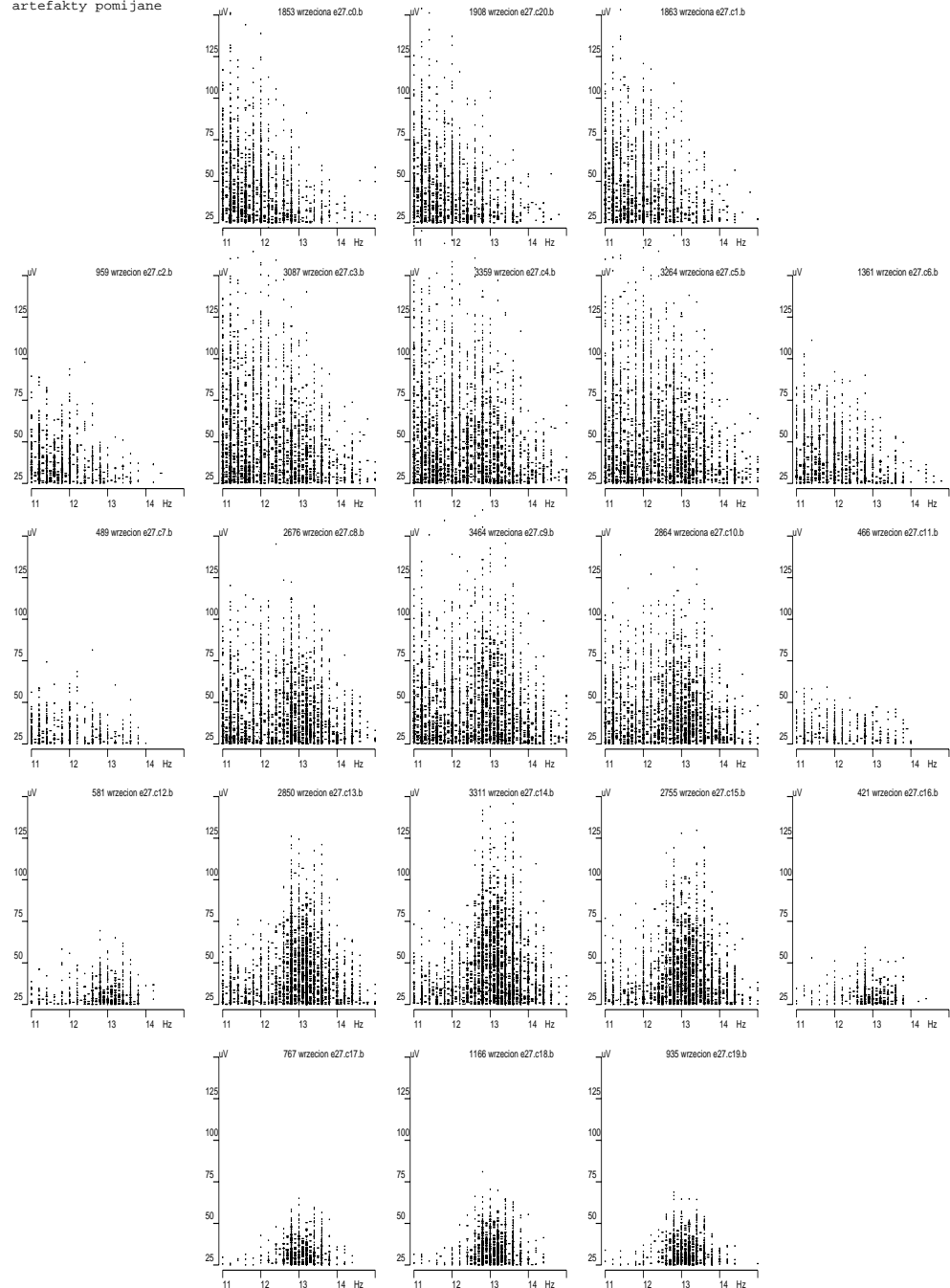


Figure 31 Plots d) from Figure 26 [detected spindles marked in the frequency-amplitude coordinates] organized as in Figure 28 [bottom - occipital electrodes]

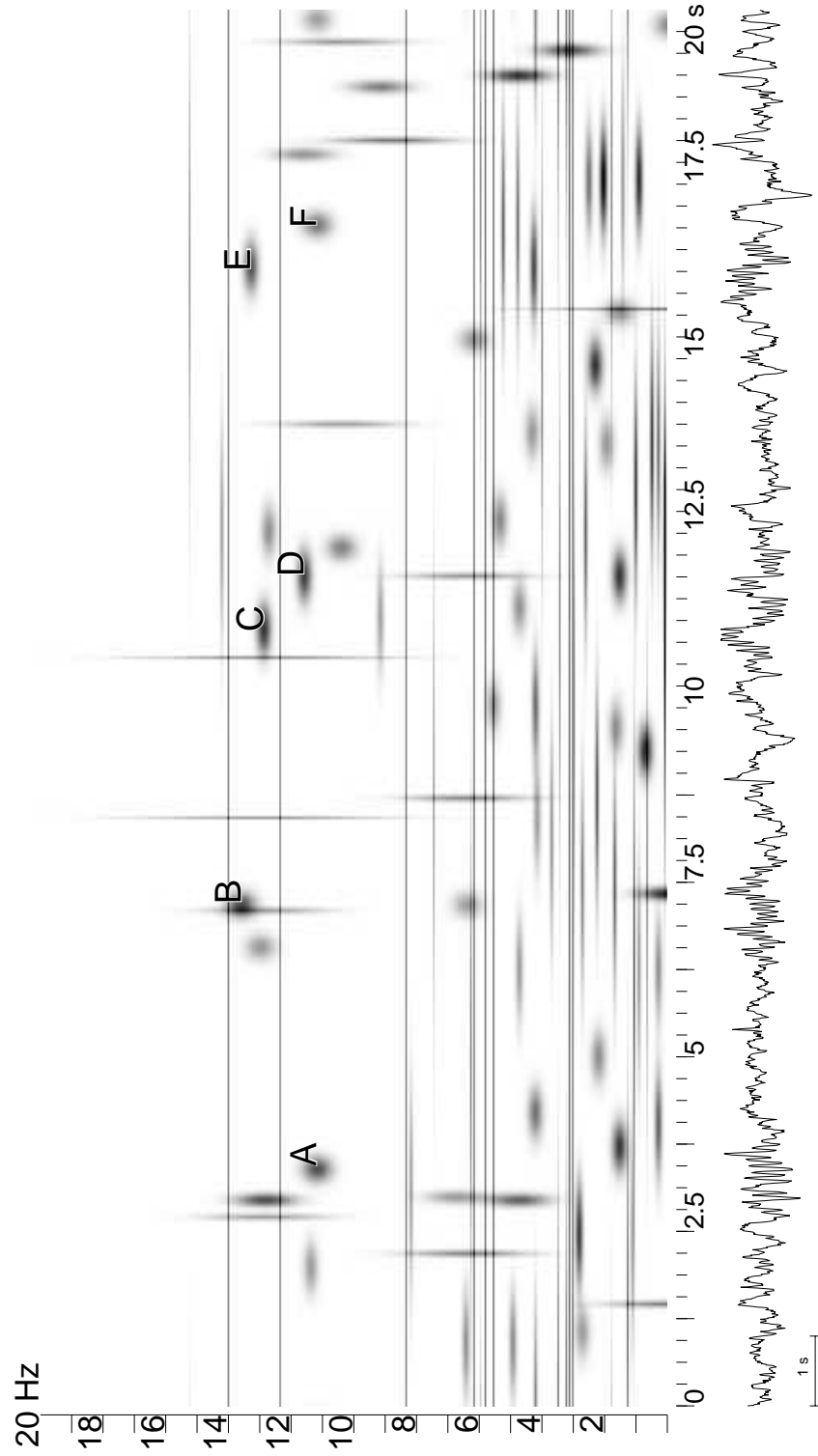


Figure 32 Structures *A* and *B* are true positive spindles. Superimposed spindles *C-D* and *E-F* were classified as one each set. Structure *F* fallen outside the epoch marked by expert.

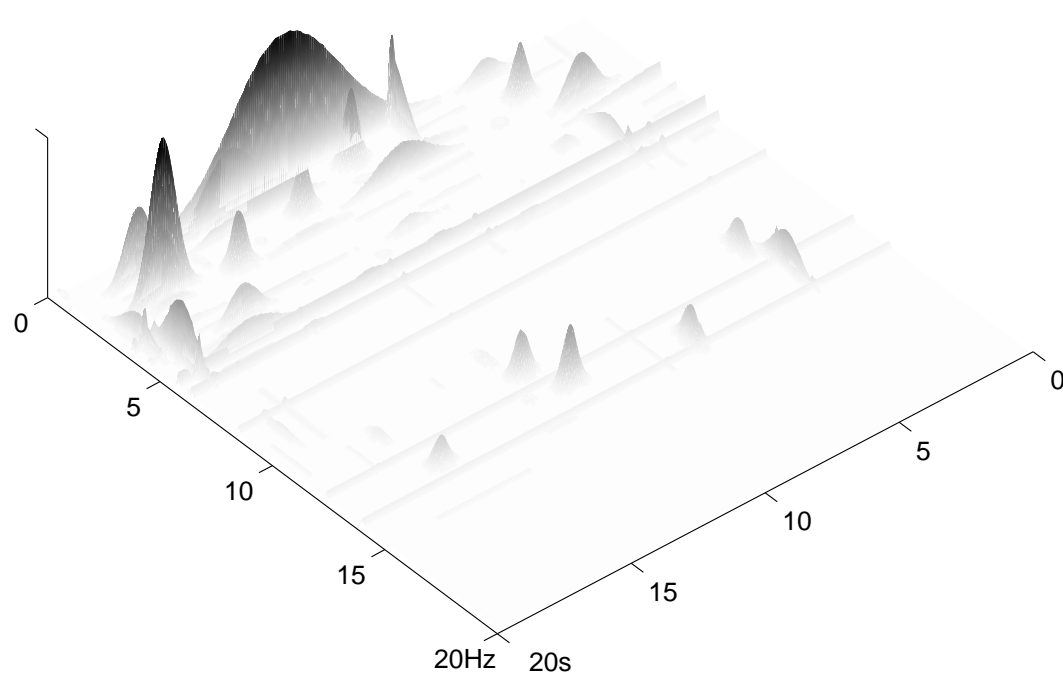


Figure 33 The same time-frequency energy distribution as in the previous figure in 3 dimensions, rotated (frequency increasing from upper left to lower right) to present clearly spindles in 12-15 Hz range.

e27 stadia 0 0 0 1 0 0 0
 ampl.>25uV, ll<=freq<=15Hz
 Tue Mar 5 19:20:14 1996
 artefakty pomijane

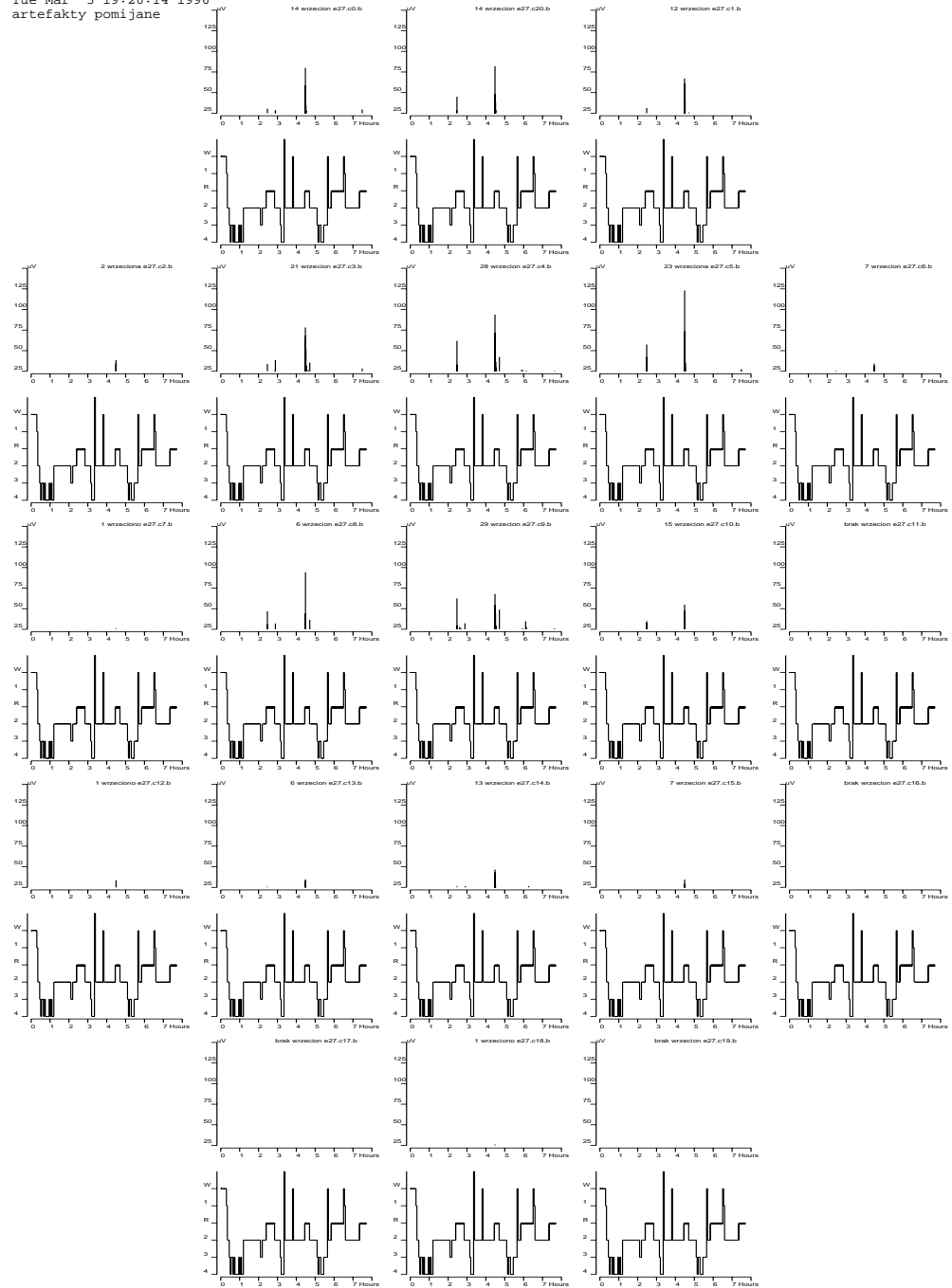


Figure 34 Spindle's amplitudes vs. time above hypnogram for 21 EEG channels. Frontal electrodes in the upper part of picture. Sleep spindles detected in stages marked as REM.

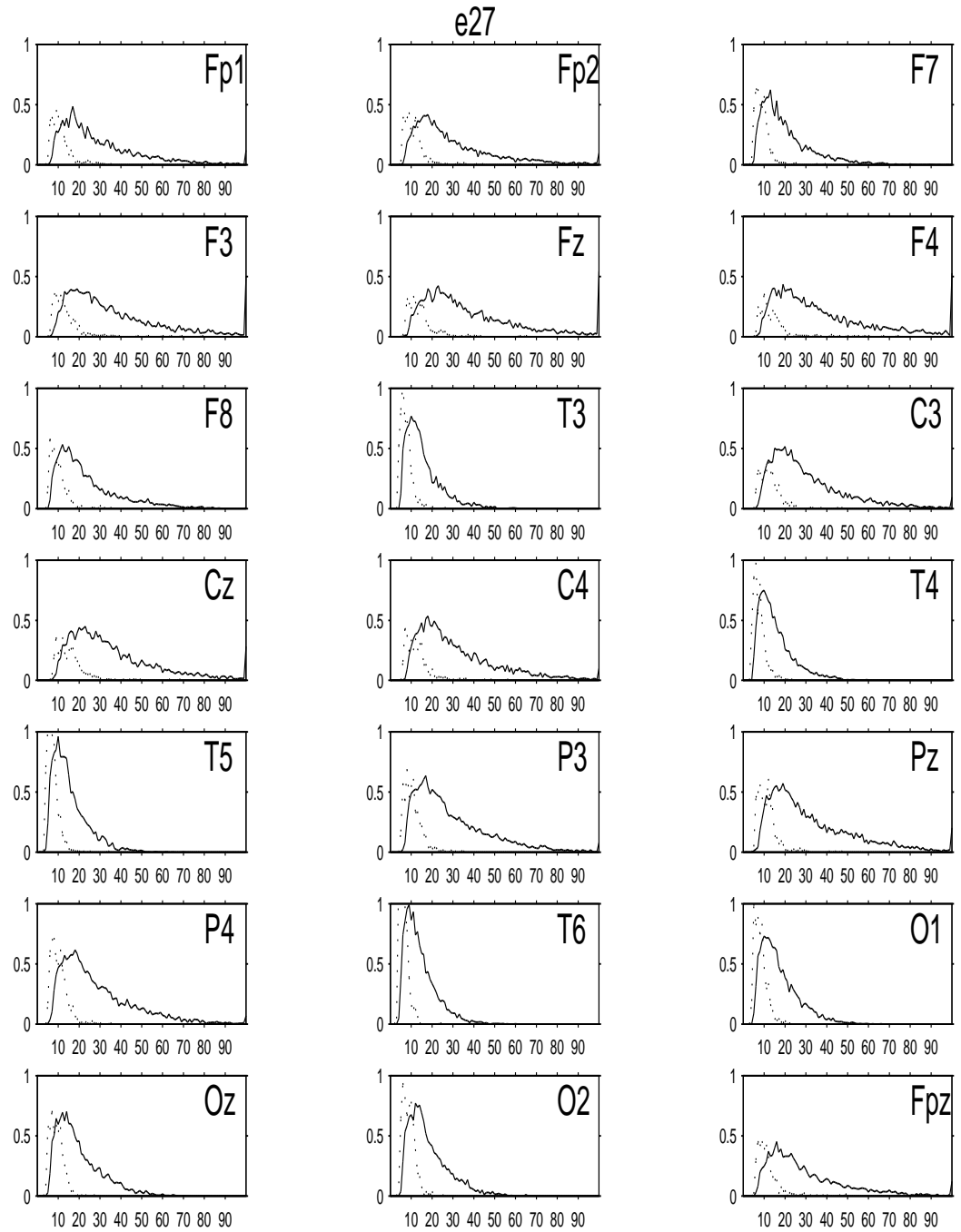


Figure 35 Density [vertical, 1/min] of structures conforming spindle's criteria for frequency and time span plotted versus cutoff amplitude [horizontal, μV]. Solid line - in non-REM stages, dotted line - in REM.

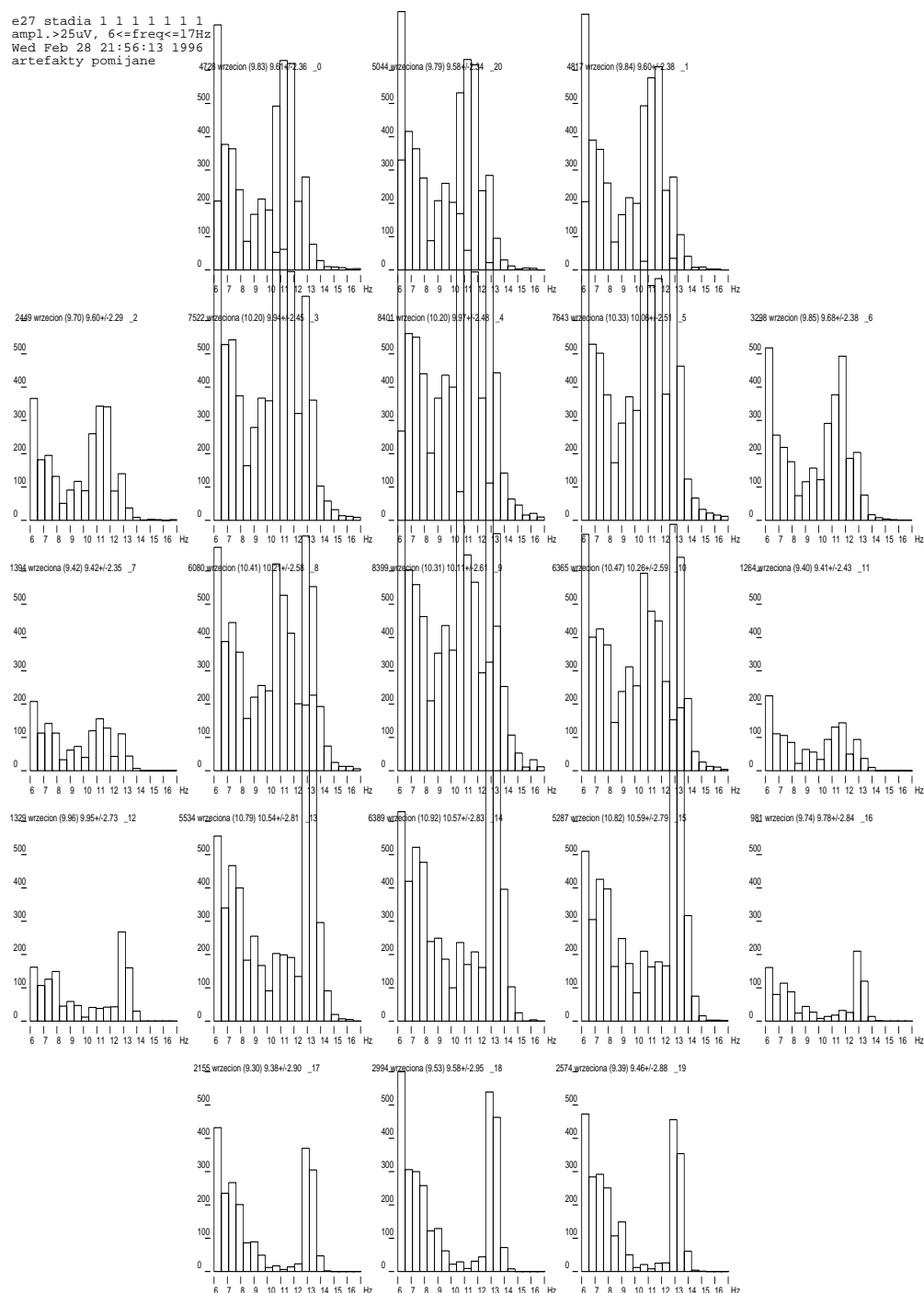


Figure 36 Histograms of frequencies of structures that would be detected as sleep spindles if we extend the frequency window to 6÷17 Hz.

4.3.6. Summary of MP application to spindles detection and analysis

MP with Gabor dictionary is a general method offering the best currently available description of EEG structures, fulfilling also the criterion of predictivity. Presented application to sleep spindles is a proposition of a more accurate description of EEG. Comparison of results of automatic spindle's detection with human judgement showed agreement lower to some of the methods reported in literature. It is result of the fact that, unlike other methods, presented algorithm was not constructed with the aim to repeat human choice, but to detect time-frequency structures within defined range of parameters regardless of the local S/N ratio.

Presented analysis confirmed several of spindle's characteristics reported in literature, assessed by means of other automatic methods or visual analysis. Among them was dominance of low-frequency in frontal and high-frequency spindles in parietal electrodes, related to the hypothesis of two generators of spindles.

Presented parameterization of the SWA (slow wave activity) is an example of straightforward application of the proposed framework to other EEG structures. Time course of spindle and slow wave activity based upon this parameterization confirmed dependencies reported in literature.

Another example of suitability of MP parameterization is the automatic separation of spindles superimposed in time domain. Previous approaches to this problem were based upon complex demodulation applied to visually selected spindles.

Finally, a method of visualization of the spatial distribution of single sleep spindles is presented. Traces of spindles in some electrodes have amplitudes far below the assumed threshold. Owing to its high sensitivity, higher to any previously applied method, presented analysis poses new questions about a phenomenon of the low amplitude spindles.

5. Conclusions

5.1. Brief discussion of time-frequency methods

The orthogonal wavelet parameterization has several advantages: low computational complexity - $O(N)$, stable and fast numerical implementations, providing information on the time-frequency distribution of signal's energy and straightforward interpretation of wavelet coefficients in terms of time-frequency energy content. In fixed orthogonal parameterization wavelet coefficients can be treated as vectors ready for statistical evaluation. Due to these features WT can provide robust and elegant solutions for a large class of problems encountered in biomedical signal analysis.

Limitations of WT are related mainly to the fact that the orthonormal basis is pre-defined. As a result the representation is sensitive to the shift in time of analyzed window, and resolutions are low in frequency domain for high-frequency structures and in time domain for low-frequency structures. Improvement in relative resolution can be brought by the wavelet packets method, in which an orthonormal basis is chosen to minimize the total entropy of the representation. Nevertheless, such choice is driven by transients of highest energy. The neural networks approach offers higher adaptivity of the representation, however due to unsolved problems of initialization and convergence it seems to be in the stage of development premature for general signal processing applications.

Improvement in adaptivity of representation can be achieved by extending the dictionary of functions used for explaining the signal's variance. Redundancy introduced in this way requires a method of choice of a subset of dictionary's waveforms for signal's description. Criterion can be based e.g. on minimalization of representation's error for given number of waveforms. Solution of such a problem is NP-hard and such an optimal expansion is not stable with respect to the number of allowed waveforms. Both these problem are absent in the Matching Pursuit (MP)

method, which offers sub-optimal solution to the problem of signal's expansion over a redundant dictionary. MP is an algorithm that iteratively fits waveforms from a redundant dictionary to local signal structures. Dictionary of Gabor functions offers best time-frequency localization properties. MP with Gabor dictionary describes structures present in signal in terms of their time of occurrence, frequency, time span, amplitude and phase with resolution that can be tuned - up to the theoretical limits. Dictionaries constructed from arbitrary waveforms, not necessarily analytical functions, can be constructed to enhance detectability of structures of particular morphology. However, practical application of MP algorithm, even for dictionaries built from analytical functions, still requires heuristic optimization to speed up the computations. This must be taken into account when comparing results obtained by means of different implementations, even if the same dictionary was used.

Nevertheless, we can say that MP provides the most complete and accurate description of time-frequency structures among currently available methods. This approach offers new possibilities in tracing EEG transients. MP decomposition of time series can also provide a complete parametrization of EEG, enhancing possibilities offered by previously applied methods.

5.2. Summary

Criteria for validation of applicability of signal processing tools to the EEG analysis were formulated. In that context several of the available time-frequency methods of signal analysis: wavelet transform, wavelet packets, wavelet networks and Matching Pursuit were discussed and their performance presented on simulated signals. Two of these methods were chosen for practical application and discussed in detail: wavelet analysis and Matching Pursuit.

Wavelet analysis was applied in two major fields: evoked potential studies and input preprocessing for feedforward neural networks. DOS software package for wavelet decomposition, statistical differentiation of wavelet coefficients and graphical presentation of results was developed. This package is being applied in several neurophysiological research projects other than quoted above.

Presented study of artificial neural networks applied to the detection of EEG artifacts showed significant improvement in performance of the network with wavelet preprocessing of input over network operating on raw signal samples. Suitability of proposed wavelet parameterization includes fast calculation of band-limited products of two signals. The best of studied networks shows performance which can be tuned to produce reliable system for routine applications. Project aimed at construction of clinically applicable neural network for artifact recognition is in progress, based upon presented approach.

Matching Pursuit was introduced to biomedical signal processing in a system of automatic detection and analysis of sleep spindles in overnight EEG recordings. Sleep spindles were described in terms of their amplitude, frequency, time width and position with accuracy higher to any method applied up to now. A Unix-based system for automatic evaluation of MP decomposition of EEG recordings was developed, making possible choice of relevant structures and presentation of results in a way suitable for investigating the physiological issues. Results of automatic detection were compared to electroencephalographers' choice showing good concordance for higher amplitudes and larger amount of structures detected by the algorithm for lower amplitudes. However, some of the methods of automatic sleep spindles detection reported in literature offer higher concordance with expert's choice. This is a natural consequence of the fact that those methods were tailored particularly

for the purpose of achieving maximum agreement with human detection, while proposed approach detects accurately the relevant time-frequency structures regardless of the local S/N ratio.

From the database of detected spindle's parameters reports were drawn in order to present the data in a way suitable for drawing physiological conclusions. Several hypotheses were confirmed:

- lower density and lower amplitudes of spindles in temporal and occipital electrodes,
- presence of two dominant frequencies: lower in frontal and higher in occipital electrodes,
- generally inverse relation of spindle activity to the slow wave activity [SWA] in slow wave sleep epochs,
- presence of superimposed spindles.

A step towards a complete description of sleep EEG in terms of MP parameters was made by presenting various aspects of SWA activity. This approach showed general consistence with results obtained previously by means of spectral analysis and offered a more precise and detailed description.

Example of automatic detection of superimposed spindles and investigation of their spatial relationships was presented. This issue was previously assessed by means of complex demodulation applied to visually scored spindles. Also the spatial relationships were previously investigated visually.

Presented method is by no means limited to sleep spindles and SWA. Accurate and detailed description of other phenomena present in EEG can be achieved by modification of the function of choice of relevant structures. In some cases clustering of atoms describing one structure or extension of the dictionary of waveforms may be necessary.

Proposed frameworks for artifact recognition by artificial neural network with wavelet input preprocessing and MP parameterization and analysis of sleep spindles can be applied to a wide class of problems and tuned for routine clinical applications. Two large projects aimed at routinely applicable automatic detection of EEG artifacts and new and complete description of sleep EEG emerged from the presented research.

List of figures

Figure 1	Symbolic division of time-frequency space for windowed Fourier transform	5
Figure 2	Symbolic division of time-frequency space for multiresolution wavelet decomposition.	8
Figure 3	Top: left - scaling function, right - wavelet. Lower part - scheme of multiresolution decomposition. A - approximated, D - detail signals at each level.	9
Figure 4	Schematic representation of a three-layer ANN	11
Figure 5	Simulated signals (<i>IV</i> and <i>VI</i>) used for presentation of performance of discussed time-frequency methods. <i>I-III</i> and <i>V</i> present structures contributing to signals <i>IV</i> and <i>VI</i>	19
Figure 6	Bottom - signal <i>IV</i> from Figure 5. Top - Fourier estimate of its spectral power density. Middle part - spectrogram, i.e. realization of windowed Fourier Transform.	21
Figure 7	Bottom - noisy signal <i>VI</i> from Figure 5. Top - Fourier estimate of its spectral power density. Middle part - spectrogram, i.e. realization of windowed Fourier transform.	22
Figure 8	Multiresolution decomposition of simulated signals: a) <i>IV</i> , b) <i>VI</i> from Figure 5. Reconstructions from wavelet coefficients at the corresponding octaves [<i>j</i> , marked 1-9 on the right].	24
Figure 9	Multiresolution decomposition of simulated signals: a) <i>IV</i> , b) <i>VI</i> from Figure 5. Height of rectangles at each scale corresponds to the values of discrete wavelet coefficients.	25
Figure 10	Multiresolution decomposition of the simulated signal shifted by 0, 5, 10 and 15 points in time. Representation of discrete wavelet coefficients.	27
Figure 11	Multiresolution decomposition of the simulated signal, shifted by 0, 5, 10 and 15 points in time. Curves marked 1-9 are reconstructions from wavelet coefficients at the corresponding scale 2^j	28
Figure 12	Multiresolution decomposition of an otoacoustic emission; upper part - reconstructed levels, lower part - wavelet coefficients. Border conditions for WT are set as zero outside the measurement window. . .	30

Figure 13	Wavelet packets decomposition of the simulated signals IV [a)] and VI [b)] from Figure 5.	33
Figure 14	Results of approximation [dashed line] of simulated signal IV from Figure 5 without the sine component [solid line] by a wavelet network of 100 wavelons in 50,000 iterations.	34
Figure 15	Wigner plots obtained by means of MP for the simulated signals shown below [compare Figure 5]. Letters mark signal structures and corresponding atoms or groups of atoms.	40
Figure 16	Examples of Gabor functions from a dictionary constructed for 2048-point segment. Amplitude of the window function $[K_{(\gamma,\phi)}, \text{eq. (3.4)}]$ set to 1.	41
Figure 17	Relative difference between the [doubled] amplitude of the window function and the actual peak-to-peak amplitude of discrete Gabor. Right axis - octaves [1-11], left - frequency in general units.	42
Figure 18	Sampling of the frequency [horizontal axis, 0-1024] - octave [vertical axis, 1-10] space in the limited Gabor dictionary discussed in chapter 3.5.	43
Figure 19	λ [eq. (4.15), solid line] and energies: remaining in residuum [dashed] and explained in iteration [dotted line] relative to signal's energy, versus number of iterations; a) EEG b) EMG	44
Figure 20	Wigner plot for the EMG signal, for which the decay of λ was plotted in Figure 19b.	45
Figure 21	Wigner plot for an EEG epoch 20 sec long [below] presented in cases where a) 50, b) 100 and c) 200 atoms (iterations) were taken into account.	46
Figure 22	Reconstructions of single evoked potentials from 5 coefficients differentiating statistically SEP from the on-going EEG. Bottom - raw recording, upper solid - reconstructed EP, dotted - average of the 55 trials.	50
Figure 23	Results of discrimination between SEP and EEG in the space of wavelet coefficients.	51
Figure 24	Number of responses of tested networks to the learning (A1, B1, C1, D1) and testing (A2, B2, C2, D2) sets. Abscissa - the value given by output neuron. Rectangles at 0 and 1 represent expert's decisions.	56

Figure 25	Automatic vs. visual detection of spindles: <i>a</i>) $TP/(TP+FP)$ vs. threshold amplitude, <i>b</i>) within ranges of amplitude, <i>c</i>) and <i>d</i>) - histograms of <i>TP</i> and <i>FP</i> detections vs. amplitude	63
Figure 26	Spindles in Cz: <i>a</i> frequencies, <i>b</i> amplitudes, <i>c</i> hypnogram [court. prof. W.Szelenberger], <i>d</i> occurrences per minute, <i>e</i> amplitudes vs. frequency, <i>f</i> histogram of frequencies.	74
Figure 27	<i>a</i>) hypnogram, <i>b</i>) frequencies <i>c</i>) amplitudes of detected spindles, <i>d</i>) spindles density [1/min.], <i>e</i>) SWA power, <i>f</i>) frequencies <i>g</i>) amplitudes of SWA structures. Time scale conserved.	75
Figure 28	Plots <i>b</i>) [spindle's amplitude vs. time] and <i>c</i>) [hypnogram] from Figure 26 presented for all the 21 EEG channels. Frontal electrodes in the upper part of picture.	76
Figure 29	Spindles <i>E</i> and <i>F</i> from Figure 32 across channels. In each box: frequency [Hz], amplitude [μ V], relative position in time [s], phase. Shades of gray proportional to amplitude. Front of head towards top of page.	77
Figure 30	Histogram of spindle's frequencies [Plot <i>d</i>) from Figure 26] presented for all the 21 EEG channels. Frontal electrodes in the upper part of picture.	78
Figure 31	Plots <i>d</i>) from Figure 26 [detected spindles marked in the frequency-amplitude coordinates] organized as in Figure 28 [bottom - occipital electrodes]	79
Figure 32	Structures <i>A</i> and <i>B</i> are true positive spindles. Superimposed spindles <i>C-D</i> and <i>E-F</i> were classified as one each set. Structure <i>F</i> fallen outside the epoch marked by expert.	80
Figure 33	The same time-frequency energy distribution as in the previous figure in 3 dimensions, rotated (frequency increasing from upper left to lower right) to present clearly spindles in 12-15 Hz range.	81
Figure 34	Spindle's amplitudes vs. time above hypnogram for 21 EEG channels. Frontal electrodes in the upper part of picture. Sleep spindles detected in stages marked as REM.	82
Figure 35	Density [vertical, 1/min] of structures conforming spindle's criteria for frequency and time span plotted versus cutoff amplitude [horizontal, μ V]. Solid line- in non-REM stages, dotted line -in REM. . .	83
Figure 36	Histograms of frequencies of structures that would be detected as sleep spindles if we extend the frequency window to 6÷17 Hz.	84

Bibliography

Wide list of wavelet-related papers available through Internet is located at
<http://www.mathsoft.com/wavelets.html>;

A large bibliography was compiled by Steven Baum:

BIBLIOGRAPHY OF WAVELET AND WAVELET-RELATED DOCUMENTS
 Steven K. Baum
 Dept. of Physical Oceanography
 Texas A&M University
baum@astra.tamu.edu

It is available through WWW or anonymous ftp in many locations, including mentioned above WWW page, as file baum.bib.

The Wavelet Digest: **<http://www.math.sc Carolina.edu/~wavelet>**
contains a current list of available preprints, events etc. References to those and others sources of relevant information can be found in my home page

<http://info.fuw.edu.pl/~durka>

Anonymous ftp sources of the two software packages used in this work are:

The Matching Pursuit Package by Stéphane Mallat and Zhifeng Zhang:

<ftp://cs.nyu.edu/pub/wave/software/mpp.tar.Z>

The Aspirin / Migraines software package by Russel Leighton from Mitre Corporation:

<ftp://pt.cs.cmu.edu/afs/project/connect/code/am6.tar.Z>

Works related to:

- ✓ Aeschbach D., Borbély AA. All-night dynamics of the human sleep EEG. *J Sleep Res* 2:70-81, 1993
- ✓ Aeschbach D., Dijk D-J, Trachsel L., Brunner D.P., Borbély A. Dynamics of Slow-Wave Activity and Spindle frequency Activity in the Human Sleep EEG: Effect of Midazolam and Zopicolone. *Neuropsychopharmacology* 1994, vol 11, No 4.
- ✓ Akay M., Akay Y.M., Cheng P., Szeto H.H. Time frequency analysis of electrocortical activity during maturation using wavelet transform. *Biol.Cybern.* 1994;71:169-176.
- ✓ Andersen P. Rhythmic 10/sec activity in the thalamus. In: Purpura DP, Yahr MD, eds *The thalamus*. New York: Columbia University Press, 1966:143-151
- ✓ Bartnik E.A., Blinowska K.J. Wavelets - a new method of evoked potential analysis. *Med.& Biol.Eng.& Comput.* 1992;30:125-126.
- ✓ Blinowska K.J., Franaszczuk P.J. A model of electrocortical rhythms generation. In: *Dynamics of sensory and cognitive processes in brain*. Ed. E.Basar, Springer Verlag Berlin, Heidelberg, 1989, pp.192-201.

- ✓ Broughton R, Healey T, Maru J, Green D and Pagurek B. A phase locked loop device for automatic detection of sleep spindles and stage 2. *Electroenceph. Clin. Neurophysiol.*, 1976, 40:67-77
- ✓ Calderón A. P. and Zygmund A. Singular integrals and periodic functions. *Studia Math.*, 14, 1954, 249-271
- ✓ Calderón A. P. and Zygmund A. On the existence of certain singular integrals. *Acta Mathematica*, 88, 85-13.
- ✓ Campbell K., Kumar A. and Hofman W. Human and automatic validation of a phase-locked loop spindle detection system, *Electroencephalography Clin. Neurophysiol.*, 1980, 48:602-605
- ✓ Coifman R.R., Meyer Y., Quake S., Wickerhauser M.V. Signal Processing and compression with wavelet packets. In: *Progress in wavelet analysis and applications*. Eds. Y.Mayer, S.Rouges. Edition Frontieres, Gif-sur-Yvette, 1993;77-94.
- ✓ Cybenko G., Approximation by Superpositions of Sigmoidal Functions, *Mathematics of Control, Signals and Systems* 1989, 2:315-341
- ✓ Daubechies I. The wavelet transform, time-frequency localization and signal analysis. *IEEE Trans.Inf.Theor.* 1990;36:961-1005.
- ✓ Davis G., Mallat S. and Avellaneda M., (b) Chaos in Adaptive Approximations, Technical Report, Computer Science, NYU, April 1994
- ✓ Davis G., Mallat S., Zhang Z., (a) Adaptive Time-frequency Approximations with Matching Pursuits <ftp://cs.nyu.edu/pub/tech-reports/tr657.ps.Z>
- ✓ Davis G., Adaptive Nonlinear Approximations - a dissertation (1994):
<ftp://cs.nyu.edu/pub/wave/report/DissertationGDavis.ps.Z>
- ✓ Dijk DJ, Hayes B, Czeisler CA. Dynamics of electroencephalographic sleep spindles and slow wave activity in men: Effect of Sleep deprivation. *Brain Res* 626:190-199, 1993
- ✓ Durka P.J. Parametryczna metoda oceny wpływu leków na EEG, M. Sc. thesis, Institute of Experimental Physics, Warsaw University 1990
- ✓ Dutertre F. Catalog of the main EEG patterns. In: Redmond A, ed "Handbook of electroencephalography and clinical neurophysiology", vol 11A. Amsterdam: Elsevier, 1977:40-79
- ✓ Fish D.R., Allen P.J., Blackie J.D.: A new method for the quantitative analysis of sleep spindles during continuous overnight EEG recordings. *Electroencephalogr Clin Neurophysiol* 70:273-277, 1988
- ✓ Garey M.R., Johnson D.S., *Computers and intractability: A Guide to the Theory of NP-Completeness*, W.H Freeman and Co., New York, 1979.
- ✓ Grossman A, Morlet J. Decomposition of Hardy functions into square integrable wavelets of constant shape. *SIAM J. Math.* 1984;15:723-736.
- ✓ Hao Y.-L., Ueda Y. and Ishii N. Improved procedure of complex demodulation and an application to frequency analysis of sleep spindles in EEG, *Med. & Biol. Eng. & Comput.*, 1992, 30, 406-412
- ✓ Harel D. *ALGORITHMICS The Spirit of Computing*, Addison-Wesley Publishers Limited 1987. Polish edition: *Rzecz o istocie informatyki. Algorytmika*. ISBN 83-204-1525-X. Wydawnictwa Naukowo-Techniczne 1992

- ✓ Hellman M.E., The Mathematics of Public-Key Cryptography, Scientific American, August 1979
- ✓ Hertz J., Krogh A., Palmer R.G. Wstęp do teorii obliczeń neuronowych, Wydawnictwa Naukowo-Techniczne, Warszawa 1993
- ✓ Jankel W.R. and Niedermayer E. "Sleep Spindles", Journal of Clinical Neurophysiology 2(1):1-35, 1985
- ✓ Jobert M., Poiseau E., Jahnig P., Schulz H., Kubicki S.: Pattern Recognition by Matched Filtering: An Analysis of Sleep Spindle and K-Complex Density under the Influence of Lormetazepam and Zopiclone. Neuropsychobiology 26:100-107, 1992
- ✓ Jobert M., Poiseau E., Jahnig P., Schulz H., Kubicki S.: Topographical Analysis of Sleep Spindle Activity. Neuropsychobiology 26:210-217, 1992
- ✓ Kamiński M., Blinowska K.J. A new method of the description of the information flow. Biol. Cybern. 65, 203-210 (1991).
- ✓ Kolmogorov, A.N. On the representation of continuous functions of many variables by superposition. Dekl. Akad. Nauk USSR 1957:114, pp. 953-956.
- ✓ Kumar A. The complex demodulation method for detection of alpha waves and sleep spindles of the human EEG in real-time. Proc Int. Conf. on Adv. Signal Processing Techn., Lausanne, 1975: 355-361
- ✓ Kumar A., Hofman W., Campbell K.: An automatic spindle analysis and detection system based on the evaluation of human ratings of the spindle quality. Waking Sleeping 3:325-333, 1979
- ✓ Kuratowski K. Pół wieku matematyki polskiej, Wiedza Powszechna, Warszawa 1973
- ✓ Lindsay P.H, Norman D.A. HUMAN INFORMATION PROCESSING An Introduction to Psychology, Academic Press Inc, London 1972. *polish edition*: Procesy przetwarzania informacji u człowieka - wprowadzenie do psychologii, PWN Warszawa 1984, ISBN 83-01-04689-9
- ✓ Loomis A.L, Harvey E.N and Hobart G.A. Cerebral states during sleep as studied by human brain potentials. J. Exp. Psychol., 1937, 21:127-144.
- ✓ Loomis A.L, Harvey E.N and Hobart G.A. Potential rhythms of the cerebral cortex during sleep. Science 1935; 81:597-8
- ✓ Mallat S. and Zhong S. Characterization of signals from multiscale edges, IEEE Transactions on Pattern Analysis and Machine Intelligence, vol 14 No 7 July 1992
- ✓ Mallat S.G., Zhang Z. Matching Pursuit with time-frequency dictionaries. IEEE Trans. Sign. Process. 1993;41:3397-3415.
- [also <ftp://cs.nyu.edu/pub/tech-reports/tr0619.ps>]
- ✓ Mallat S.G. A theory of multiresolution signal decomposition: the wavelet representation. IEEE Trans. Pattern Anal. Machine Intell. 1989;11:674-693.
- ✓ Oppenheim A.V., Schafer R.W. Digital signal Processing, Prentice-Hall 1975, ISBN 0-13-214107-8 01
- ✓ Pivik R.T., Bylsma F.W., Nevins R.J.: A new device for automatic sleep spindle analysis: The 'Spindicator'. Electroencephalogr Clin Neurophysiol 54:711-713, 1982

- ✓ Rechtschaffen A., Kales A. eds A manual of standarized terminology, techniques and scoring system for sleep stages in human subjects. Washington: US Government Printing Office, 1968.
- ✓ Schimicek P, Zeitlhofer J, Anderer B and Saletu P. Automatic Sleep-Spindle Detection Procedure: Aspects of Reliability and Validity, Clinical Encephalography 1994 Vol. 25 No. 1 pp. 26-29
- ✓ Tadeusiewicz 1993 Sieci Neuronowe, Akademicka Oficyna Wydawnicza RM Warszawa 1993, ISBN 83-85769-03-X
- ✓ Thakor N.V., Xin-Rong G., Yi-Chun S., Hanley D.F. Multiresolution wavelet analysis of evoked potentials. IEEE Trans on BME 1993;40:1085-1093.
- ✓ Trenker E, Rappelsberger P. Requirements for automatic sleep spindle detection using artificial neural networks. Medical & Biological Engineering and Computing Vol. 34, Supplement 1, Part 2, 1996, pp. 225-226, The 10th Nordic-Baltic Conference on Biomedical Engineering, June 9-13, 1996, Tampere, Finland
- ✓ Zhang Q, Benveniste A, Wavelet Networks, IEEE Trans on Neural Networks, 1992;3:889-898.

Papers I have co-written or written:

- ✓ E.A. Bartnik, K. J. Blinowska, P.J. Durka. Single Evoked Potential Reconstruction by Means of Wavelet Transform, Biological Cybernetics 67, 175-181, 1992
- ✓ K.J. Blinowska, P.J. Durka, A. Kołodziejak, R. Tarnecki. The Influence of Cerebellar Lesions on SEP Studied by Means of Wavelet Transform, Acta Neurobiologiae Experimentalis, vol. 52, Number 3, p.129, 1992
- ✓ K.J. Blinowska, P.J. Durka, A. Kołodziejak, R. Tarnecki. Application of Wavelet Transform to the Single Evoked Potentials Analysis and Reconstruction, Technology and Health Care - Conference Issue, Abstracts of the Second European Conference on Engineering and Medicine, Stuttgart, Germany, April 25-28, 1993 Eds. J.E.W. Benken, U.R. Faust 1:344-345.
- ✓ P.J. Durka. Detection and Analysis of Sleep Spindles by Means of Matching Pursuit, Abstracts of Ist International Congress of the Polish Sleep Research Society, Warszawa, 15-16 April, 1994
- ✓ K.J. Blinowska, P.J. Durka, W. Szelenberger. Time-Frequency Analysis of Nonstationary EEG by Matching Pursuit, World Congress of Medical Physics and Biomedical Engeneering, Rio de Janeiro, August 1994
- ✓ K.J. Blinowska, P.J. Durka. The Application of Wavelet Transform and Matching Pursuit to the Time-Varying EEG signals, In: Intelligent Engineering Systems through Artificial Neural Networks. Vol.4. pp.535-540. Eds.: C.H.Dagli, B.R.Fernandez. ASME Press, New York, 1994. (*invited paper*)
- ✓ P.J. Durka, K.J. Blinowska, A. Skierski, G. Tognola, F. Grandori. Optimal time-frequency representation of OAE. Abstracts of the 3rd European Conference on Engineering and Medicine, Florence, p.78, 1995.

- ✓ P.J. Durka, K.J. Blinowska. Analysis of EEG transients by means of Matching Pursuit. *Annals of Biomedical Engineering* 23:608-611, 1995. (*invited paper*)
- ✓ P.J. Durka, K.J. Blinowska. Modern methods of non-stationary time series analysis - Wavelets and Matching Pursuit. Xth Congress of the Polish Society of Medical Physics, Kraków, Sept.15-18, 1995. (*invited paper*)
- ✓ K.J. Blinowska, P.J. Durka. Introduction to wavelet analysis. Presented at the workshop: Techniques and methods for future EOAE systems, Milano, November 12, 1994. To be published in *British Journal of Audiology*, 1996. (*invited paper*)
- ✓ P.J. Durka, R. Księżyk, K.J. Blinowska. Neural networks and wavelet analysis in EEG artefact recognition. II Konferencja Sieci Neuronowe i Ich Zastosowania, Szczyrk 30 IV - 4 V 1996
- ✓ P.J. Durka, K.J. Blinowska, J. Żygierewicz. Matching Pursuit - a method of evaluation and parametrisation of non-stationary signals and transients. *Medical & Biological Engineering and Computing* Vol. 34, Supplement 1, Part 1, 1996, pp. 429-430, The 10th Nordic-Baltic Conference on Biomedical Engineering, June 9-13, 1996, Tampere, Finland. (*invited paper*)

accepted for publication:

- ✓ P.J. Durka, K.J. Blinowska In pursuit of time-frequency representation of brain signals. In *Time-Frequency and Wavelets in Biomedical Engineering*, IEEE press (*invited paper*)
- ✓ P.J. Durka, E.F. Kelly, K.J. Blinowska Time-frequency analysis of stimulus-driven EEG activity by Matching Pursuit, Abstracts of 18th Annual International Conference of the IEEE EMBS, Amsterdam, 31 Oct-3 Nov 1996
- ✓ P.J. Durka, K.J. Blinowska Matching Pursuit parametrization of sleep spindles, Abstracts of 18th Annual International Conference of the IEEE EMBS, Amsterdam, 31 Oct-3 Nov 1996
- ✓ K.J. Blinowska, P.J. Durka, M. Kamiński, W. Szelenberger. Methods of Topographical Time-Frequency Analysis of EEG in Coarse and Fine Time Scale, Sintra Workshop on Spatiotemporal Models in Biological and Artificial Systems, Sintra, Portugal, 6-8 November 1996
- ✓ W. Szelenberger, P.J. Durka, K.J. Blinowska. Evaluation of Sleep Spindles by Means of Matching Pursuit, X World Congress of Psychiatry, Madrid, August 23-28, 1996

submitted:

- ✓ P.J. Franaszczuk, G.K. Bergey, P.J. Durka Application of time-frequency transform analysis to hippocampal activity in mesial temporal seizures, Abstracts of 1996 American Epilepsy Society Annual Meeting, *to be published in Epilepsy*
- ✓ P.J. Franaszczuk, G.K. Bergey, P.J. Durka Time-frequency analysis of mesial temporal lobe seizures using the Matching Pursuit algorithm. Abstracts of 1996 Annual Meeting of Society for Neuroscience, Washington, D.C. November 16-21, 1996